Summer 7-28-2017

HYPERELASTIC STRUCTURAL FUSES FOR IMPROVED EARTHQUAKE RESILIENCE OF STEEL CONCENTRICALLY-BRACED BUILDINGS

Francys López-Mosquera
University of Nebraska - Lincoln, flopez-mosquera@huskers.unl.edu

HYPERELASTIC STRUCTURAL FUSES FOR IMPROVED EARTHQUAKE RESILIENCE OF STEEL CONCENTRICALLY-BRACED BUILDINGS

by

Francys López-Mosquera

A THESIS

Presented to the Faculty of

The Graduate College at the University of Nebraska

In Partial Fulfillment of Requirements

For the Degree of Master of Science

Major: Civil Engineering

Under the Supervision of Professor Joshua Steelman

Lincoln, Nebraska

August, 2017

HYPERELASTIC STRUCTURAL FUSES FOR IMPROVED EARTHQUAKE RESILIENCE OF STEEL CONCENTRICALLY-BRACED BUILDINGS

Francys López-Mosquera, M.S.

University of Nebraska, 2017

Advisor: Joshua Steelman

Improving structural resilience (i.e., reducing service interruptions and improving rapidity of function restoration) following extreme events is one of the primary contemporary challenges in structural engineering. While massive casualties have successfully been avoided through the adoption of modern building codes, the sole codified performance objective has been limited to the life safety/collapse prevention range of response. Christchurch, NZ, highlighted the insufficiency of this approach, with large sections of the city nonfunctional after a major earthquake, and with subsequent collapses induced by significant aftershocks. Engineering advances to improve building and community resilience are necessary to mitigate hazards from becoming disasters. This study explores the influence and potential benefits of introducing a hyperelastic 3D printed fusing component on global performance outcomes, focusing primarily on direct economic loss estimates. This work identifies potentially beneficial combinations of hyperelastic component phenomenological parameters (i.e., stiffness, ductility, resisting force), presenting the results as a performance comparison between the hyperelastic and conventional hysteretic systems. Current 3D printing technologies allow the easy creation of complex geometries, hence it is expected that 3D printed steel fuses can provide a strategically defined multi-linear hyperelastic constitutive response through geometric configuration and small-scale elastic buckling. The hyperelastic component behavior

permits shared participation of mechanical and inertial effects at the global structure level, while also achieving self-centering after extreme loading has concluded. Additionally, the lack of residual drift combined with the lack of significant structural damage will permit continued occupation with minimal functional disruption.

ACKNOWLEDGEMENTS

Foremost, I want to thank my advisor, Dr. Joshua Steelman, for his commitment, patience and constant support through the learning process of this master thesis. Thank you for the stimulating discussions, and I feel honored to have had the opportunity to work with such a genuine professor.

I would like to thank my fellow graduated students, Pranav Shakya, Ahmed Rageh, Fayaz Sofi, Steven Stauffer, Linh Abdulrahman, and Cesar Gomez, who have contributed to building my body of knowledge through this challenging experience at UNL. I will never forget the sleepless nights working together before deadlines, but overall I will always remember your friendship and advice.

I want to express my gratitude to my committee members Dr. Christine Wittich and Dr. Ronald Faller for sharing their time and expertise in my advisory committee to strengthen this work.

I would like to acknowledge Amber Hadenfeldt for her responsiveness and guidance in editing this thesis. All your suggestions and comments enriched this work tremendously.

I would like to thank Fulbright Colombia and the UNL Civil Engineering department for funding me through this program.

Lastly, and most importantly, I want to thank God and my loved ones for being there for me even when it seemed I was not there for you. Your continuous encouragement kept this boat afloat through the worst storms.

TABLE OF CONTENTS

LIST OF FIGURES

LIST OF TABLES

CHAPTER 1. INTRODUCTION

Indirect economic losses from societal disruptions caused by recent seismic events suggest that traditional (code-based) prescriptive structural engineering outcomes should become less of a final design and more of a preliminary step for structural engineering in the future. Continuous operation and avoiding prolonged disruption times are desirable, next-generation performance objectives for civil structures.

The mismatch between societal expectations and code-based structural engineering outcomes was recently highlighted during the 2010-2011 Christchurch earthquakes in New Zealand, which were some of the most expensive hazards for insurance companies on record (over 16 NZ billion). The main shock hit Christchurch in September 2010, where very few casualties were reported due to the excellent life-safety performance of typical construction. At the same time, considerable structural damage was incurred (some undetectable by non-destructive evaluation). Five months later, in February 2011, an aftershock impacted the Canterbury community, while the region was still under recovery. The aftershock hit structures with reduced stiffness that had already incurred permanent drifts, which caused partial or total collapse of several structures and over 180 casualties. Two-thirds of the casualties occurred after the six-story CTV news office building collapsed, a structure that was marked as safe after the 2010 September quake. The New Zealand authorities, alongside insurance companies, have been working to reconstruct the Christchurch community with the primary goal of minimizing infrastructure disruption and assuring sufficient aftershock resistance (Stevenson et al. 2011). Discussions about these scenarios that address resilience are timely and relevant at an international level.

In the United States, President Barack Obama issued an executive order in February 2016 urging the U.S. Department of Housing and Urban Development (HUD) to adopt resilient construction for all federal buildings, stating that existing construction requirements should be reviewed and revised to meet higher standards that ensure federal buildings will perform with improved earthquake resilience (Exec. Order No. 13717 (2016)).

This executive order also highlighted the prominent role of higher learning centers in addressing this challenge.

> "The Administration is announcing a coalition of 97 colleges, universities, associations, and academic centers around the country that are committing to ensure that the next generation of design professionals are prepared to design and build for extreme weather events and impacts of climate change"

A significant step toward facilitating higher performance standards was taken in 2006, before Christchurch, by the US Federal Emergency Management Agency (FEMA). FEMA published FEMA 445, providing guidance produced through a joint project titled "Next-Generation Performance-Based Seismic Design Guidelines Program Plan for New and Existing Buildings." FEMA 445 highlighted the limitations of current structural design procedures, including the challenges of accurately estimating new performance measures such as repair costs, probability and quantity of casualties, and operational disruption time. These new performance measurements are critical for project investors, insurance companies, and other decision makers. (FEMA 2006)

To achieve higher performance levels, societies cannot rely on traditional design bases and techniques because extrapolating their characteristics will not meet advanced and emerging performance objectives, such as resiliency. Therefore, exploring and developing new or modified structural systems is a prominent requirement for resilient structural engineering.

Currently, there are high-performance systems under evaluation such as rocking, self-centering, energy dissipating fuses, and combinations thereof (Hajjar et al. 2013). In the last decade, structural configurations using Shape Memory Alloy (SMA) metals (DeRosches et al. 2007; Gao et al. 2016; Qiu and Zhu 2017a) and systems incorporating Self Centering Energy-Dissipative (SCED) Braces (Christopoulos et al. 2008; Tremblay et al. 2008; Erochko and Christopoulos 2014) have been rigorously investigated to advance the potential implementation of self-centering in practice. While the present study also focuses on a physical component that provides multi-linear elastic response to the structure, the components under consideration in this study can be distinguished from pre-existing literature because the components do not rely on material nonlinearity but on strategically varying system stiffness through geometric configuration.

This thesis assumes the availability of a 3D printed steel fuse device (see Figure 1), and presents the results of a parametric study conducted to characterize preferential behavior for such a device. The fuse provides the structural system with hyperelasticity, which renders in a multi-linear elastic force-displacement response, so that yielding of the Lateral Force Resisting System (LFRS) and the fuse itself are largely avoided. Additionally, and more importantly, this component would help the structure return to its initial position after the ground shaking has ceased.

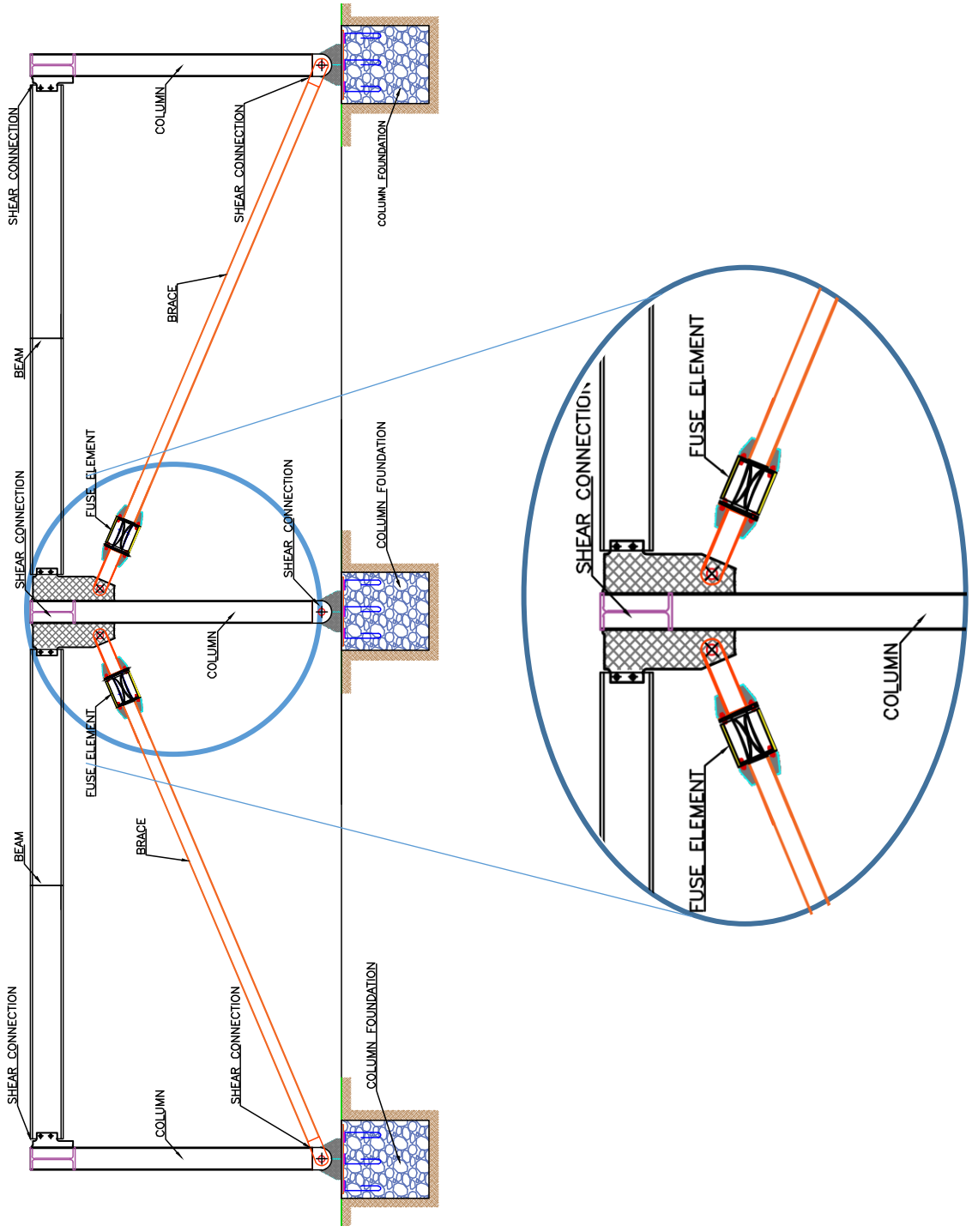

Figure 1. Idealized hyperelastic braced frame

To exhibit such behavior, the proposed hyperelastic fuse is equipped with an elastic-controlled, buckling mechanism as shown in Figure 2 and Figure 3, which consists of a combination of stocky and slender compression elements. During an intense seismic excitation, the slender supports are allowed to buckle elastically once a predefined force level is reached. This buckling creates a reduction of the system stiffness (similar to material yielding), allowing the system to displace with minimal additional induced load. This stage of response continues up to the point where the gap closes, and the stocky supports are also engaged in compression, increasing the system stiffness and induced force demands (tri-linear elastic).

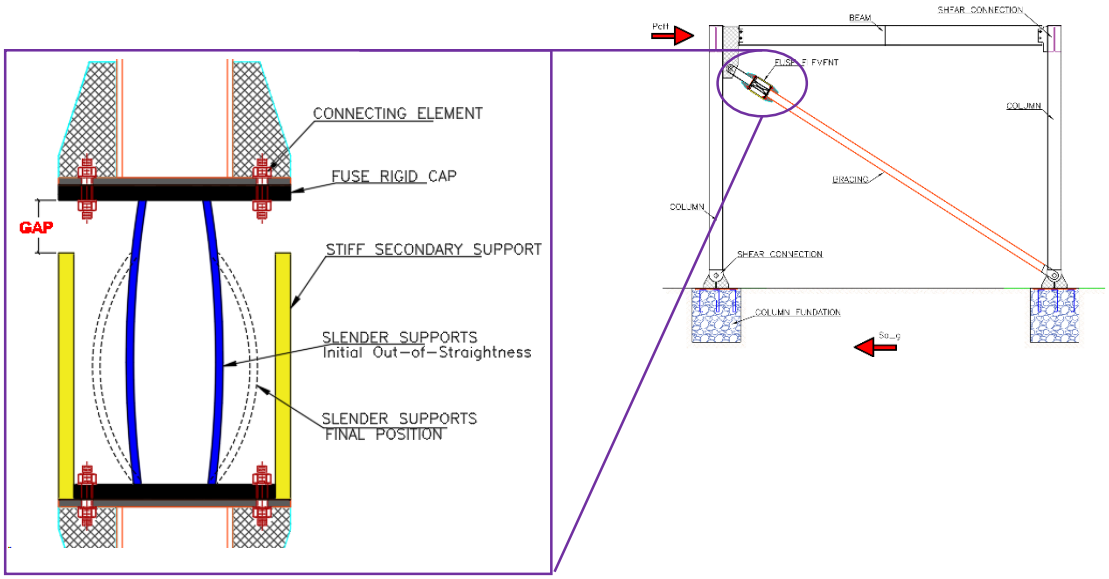

Figure 2. Idealized Hyperelastic Structural Fuse. Right: General Description; left: Sketch of the internal buckling mechanism.

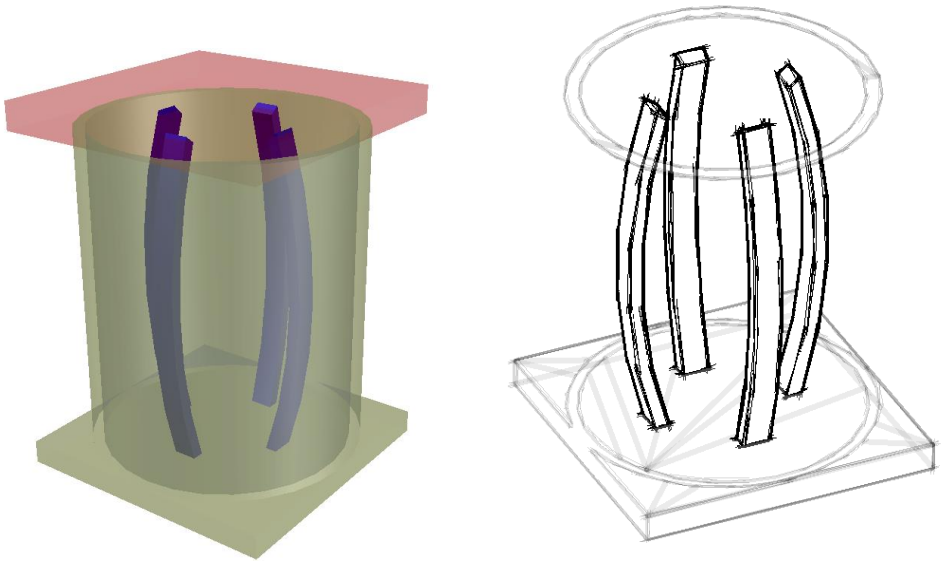

Figure 3. 3D Rendering of Idealized Hyperelastic fuse.

Figure 4 is presented to illustrate the sequence of configuration and corresponding behavioral response stages, where the force-displacement behavior is divided into three loading stages and one unloading phase. The first stage, the line between points 1-2, is when the force in the brace (f) is less than the buckling force of the slender elements (f_e). At this stage, we encounter a typical linear elastic response. The buckling elements are shown with exaggerated out-of-straightness. Printed components are intended to be produced with nearly perfect straightness to minimize buckled strength reduction. Second, the line between 2-3 is when "f" exceeds "f_e"; the slender elements buckle, allowing the structure to displace without a considerable increase in force. Lastly, the third loading stage is reached when the gap has closed, and the stocky elements carry the load again up to a predefined maximum system force (f_{max}).

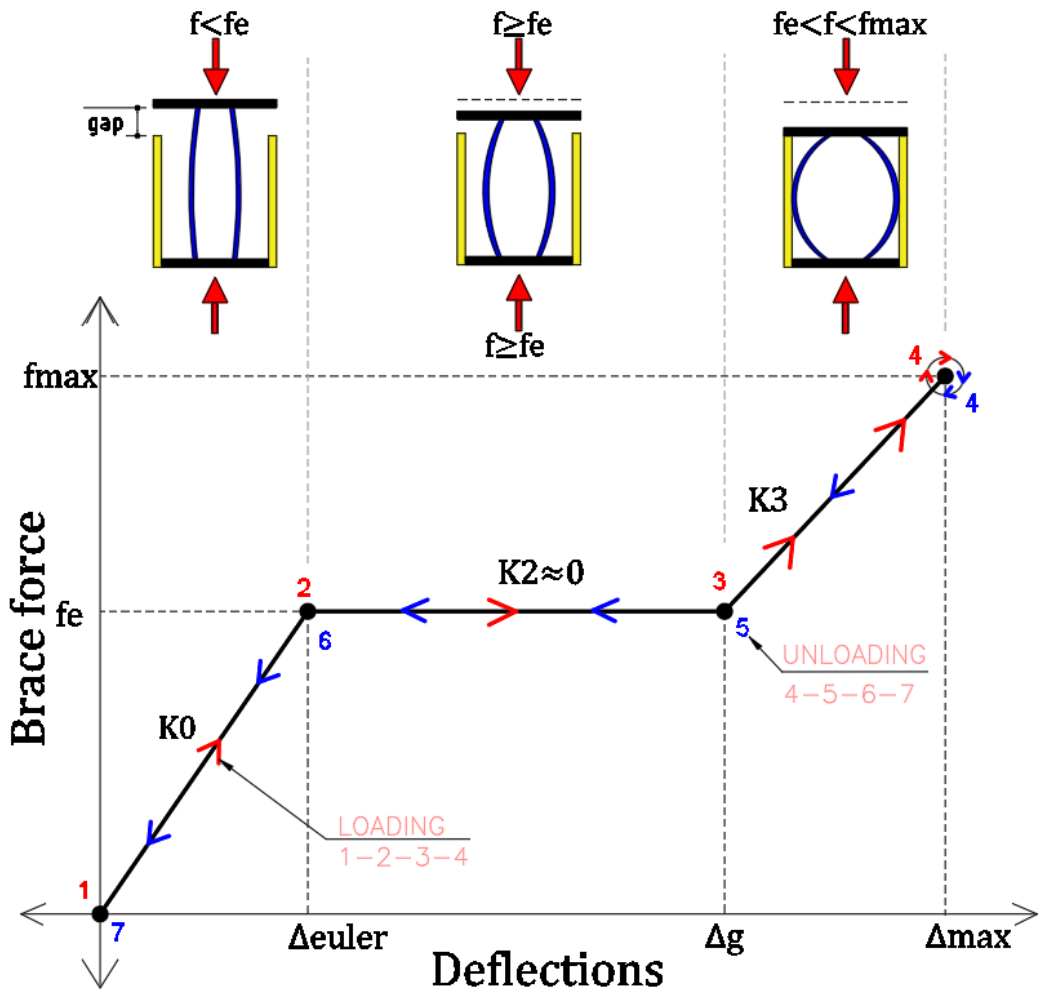

Figure 4. Force-Displacement curve of the Hyperelastic system.

Once the load has been removed, the component response trajectory flows along 4-5-6-7. The slender elements come back to their initial position (elastic buckling), forcing the system to self-center. Furthermore, 3D printed metal fuse fabrication and post-processing is expected to considerably reduce or eliminate the residual stresses exhibited by traditionally fabricated steel shapes. Additionally, a small out of straightness can be introduced to ensure monotonically increasing load-deformation response during buckling.

In conclusion, higher performance systems are needed to attain resilience in steel construction. Numerous authors have studied this problem and have developed an array of potential solutions as a result (refer to Chapter 2. Literature Review). The concepts underlying the proposed device, such as elastic buckling of slender elements, have been studied for decades and thus are well understood. However, the potential application of strategically configured buckling to achieve self-centering has not been sufficiently explored. The hyperelastic 3D printed fuse concept described in this study provides a wide range of possibilities for structural engineers to achieve resilient structural response using geometric nonlinearity and self-centering capabilities.

CHAPTER 2. LITERATURE REVIEW

2.1. Fuses in Braced Frames

Braced frames have been one of the preferred structural systems used to resist lateral load effects in steel building construction. Concentrically-braced frames (CBFs) were favored when metal framing was becoming more commonplace, and lateral resisting systems were primarily focused on resisting wind loads. Seismic demands exposed the potential instability of CBFs under repeated, cyclic, inelastic excursions. Undesirable structural behavior observed under seismic loading included rapid stiffness degradation due to buckling of the compression braces, and damage concentration in certain stories (inability to redistribute seismic forces along the building height) (Christopoulos et al. 2002b; Roeder and Popov 1978).

More recently, Japanese engineers developed Buckling Restrained Braces (BRBs) to avoid global buckling of compression braces between end attachments. BRBs represent a major step forward in achieving full hysteretic behaviors and improved seismic performance (Vargas and Bruneau 2005, AISC 341). Alternatively, eccentrically-braced frames (EBFs), which include a localized fusing region (i.e., the “link” segment), can provide stable hysteretic behavior and excellent energy dissipation. EBF links are intended to bear most of the inelastic deformation induced by seismic (lateral) excitations. EBF shear links studied by Popov in the 1970s and 1980s and knee bracing studied by Aristizábal-Ochoa in 1986 constitute the first fuses widely reported in the literature. Roeder and Popov later referred to these links as ductile fuses. (Malley et al. n.d.; Roeder and Popov 1978; Vargas and Bruneau 2009).

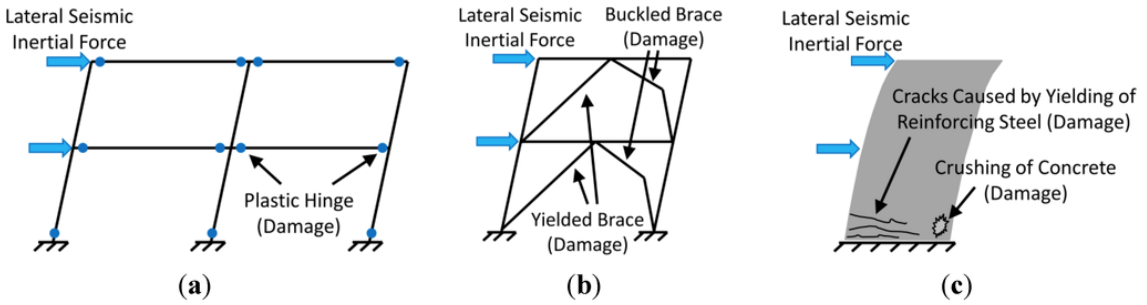

Figure 5. Hysteretic behavior of conventional structural systems: (a) Steel moment resisting frame; (b) Single steel brace; (c) Concrete shear wall. (Nathan Chancellor et al. 2014)

Based on the definition above, the fuse concept has been widely used in the past 30 years of structural engineering, but two aspects are primarily and actively being researched: damaged fuse replacability and self-centering capabilities (Tremblay, 2008). This work aims to contribute advances with respect to self-centering features, which are rarely found in current structural systems, such BRB frames. Despite the fact that these conventional systems have performed successfully at the life-safety/collapse prevention level in the past, they have also exhibited localized damage compromising the global stability of the structure against potential aftershocks, and resulted in economic and social disruption.

Research to create innovative systems with self-centering capabilities in on-going in current literature. For instance, Songye Zhu (2008) and DeRosches (2004, 2016) have studied the use of Shape Memory Alloys (SMAs) to achieve resilient buildings. SMAs are smart nickel/titanium-based metals that have excellent ductility and can recover to an original, undeformed shape after load removal (super-elasticity). However, despite these remarkable features, SMA metals are still expensive to produce and do not exhibit sufficient fatigue resistance (Rahimatpure 2012). Similarly, Christopoulos at al. (2008)

introduced a Self-Centering Energy-Dissipative (SCED) Brace, which incorporates springs within the fuse that force the structure to return to the original position.

Significant steps have been made to enhance replaceability of structural fuses. However, self-centering capabilities have advanced at a slower pace. Within the pool of self-centering systems, few solutions or studies have been found viable, because they either rely on expensive materials (like SMAs) or in rather complex component assemblies (like SCED).

2.2. State of the Art in Resilient Structural Systems

There are many definitions for structural resilience, but the various definitions consistently share two main points in common: robustness and rapid restoration ("rapidity"). The first is related to the capability of the structure to withstand a rare event, and the second is related to how quickly the structure can be operational again (Rodriguez-Nikl 2015). Increasing robustness within a reasonable budget would only reduce the probability of structural collapse while downtime can still be a problem. Today, implementing low-damage technologies is structural engineers' main contribution to mitigating the lack of rapidity. Several studies have been conducted to address these issues.

Hajjar et al. (2013) conducted an extensive literature review consigned in a report called *"A synopsis of sustainable structural systems with rocking, self-centering, and articulated energy dissipating fuses."* This document summarized more than 100 innovative structural systems and their key features, covering a broad range of the

relevant research up to 2011, two years before the document was published (Hajjar et al. 2013).

Relevant research conducted after or not included in the report by Hajjar et al. is presented below:

2.2.1. "Development of a ratcheting, tension-only fuse mechanism for seismic energy dissipation" (2015)

J. Cook, G.W. Rodgers, G.A. MacRae & J.G. Chase

The authors present an innovative tension-only mechanism, which aims to fix the residual compression force problems that current post-tensioned rocking systems face. The device incorporates a linear ratcheting mechanism that guarantees tension-only structural participation of the brace (Figure 6a).

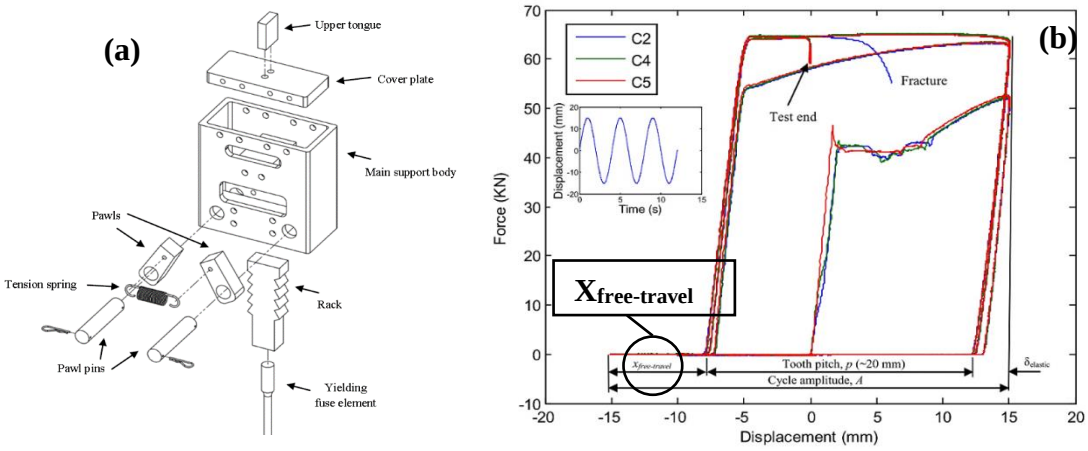

Figure 6. (a) Ratchet mechanism assembly; (b) Force displacement hysteresis (Cook et al. 2015).

To guarantee single direction engagement, a tension spring maintained engagement between the two pawls and the strategically orientated teeth on the sliding rack. Figure 6b illustrates the hysteresis behavior of the tested device, showing that the brace behaves identically to a conventional brace in tension, but when in compression the

device enters a free travel zone, which offsets the zero (0) datum for the next tension incursion. Experimental component validation tests were carried out showing that residual compressive forces were reduced and thus implementing this technology could enhance self-centering capabilities when incorporated into rocking systems. (Cook et al. 2015)

2.2.2. "Optimal Seismic Performance of Friction Energy Dissipating Devices" (2008)

Sanjaya K. Patro and Ravi Sinha.

This system is equipped with a sliding plate, which has slotted holes. Attached to this plate are two clamping plates with pre-stressed connection bolts (see Figure 7, right). The slotted holes allow for displacement, creating a multi-linear elastic force-displacement behavior.

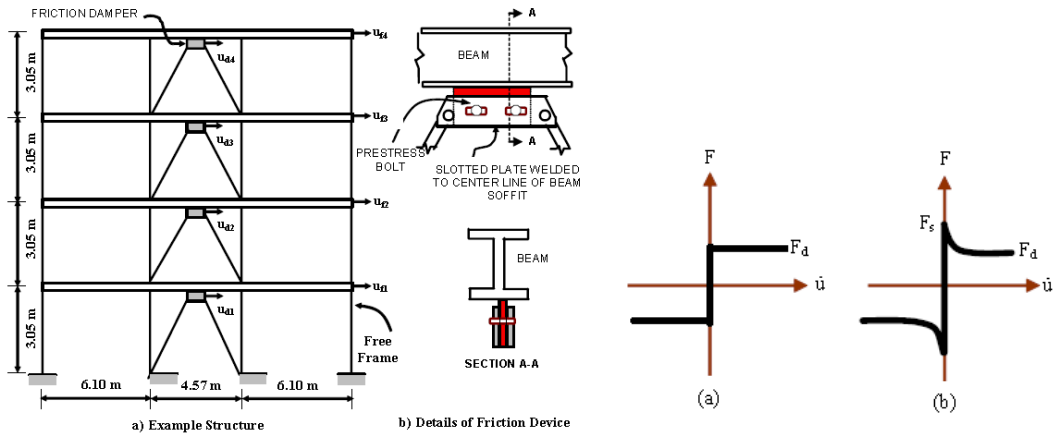

Figure 7. Right: Schematic diagram of four-story building with friction devices (Dimova et al. 1995), left: Dry Friction Models (a) Coulomb Friction Model (b) Realistic Friction Model (Patro and Sinha, 2008).

Patro and Sinha found that using the Coulomb friction model (Figure 7a, left) is not a good approximation of real behavior. The authors found that including stiction and Stribeck effects yielded considerable differences for a realistic dry fiction model. The

study concluded that more realistic models should be used when designing this brace configuration, paying special attention to the pre-stress force applied by the bolts. Bolt prestressing was identified as the most important parameter in this study. (Patro and Sinha 2008)

2.2.3. "Shake table test and numerical study of self-centering steel frame with SMA braces" (2016)

Canxing Qiu, and Songye Zhu.

Qiu and Zhu present a numerical study on the response of Shape Memory Alloy Braced Frames (SMABF), accompanied by experimental validation. The system incorporates an SMA-based damper similar to the one shown in Figure 8. The authors highlighted the good agreement between the analytical models and the test results.

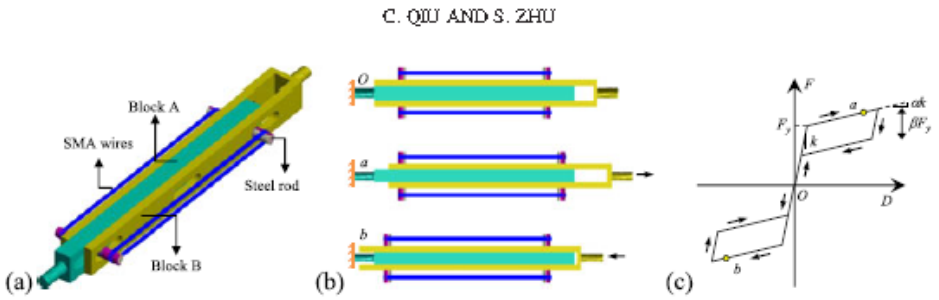

Figure 8. SMA-based damper: (a) configuration of SMA damper; (b) deformation under tension and compression; and (c) idealized flag-shaped hysteresis (Qiu and Zhu 2017b)

The specimens showed strong self-centering capabilities for all earthquake levels. The Lateral Force Resisting System (LFRS) remained elastic, suggesting that economic or social disruption would not be significant for structures implementing this system (Qiu and Zhu 2017b).

2.2.4. "Analytical Response and Design of Buildings with Metallic Structural Fuses. I" (2009)

Ramiro Vargas and Michel Bruneau.

The authors propose a simplified design procedure to assess systems with structural fuses. The proposed procedure assumes that the inelastic deformations will concentrate only on the fuse element, serving as a fast approach to have reasonable estimates without engaging in tedious nonlinear time-history analyses. The procedure states that the structural fuse concept is fully satisfied once specific ductility and period combinations are met (i.e., ductility <1.0 and $T<T_{Limit}$).

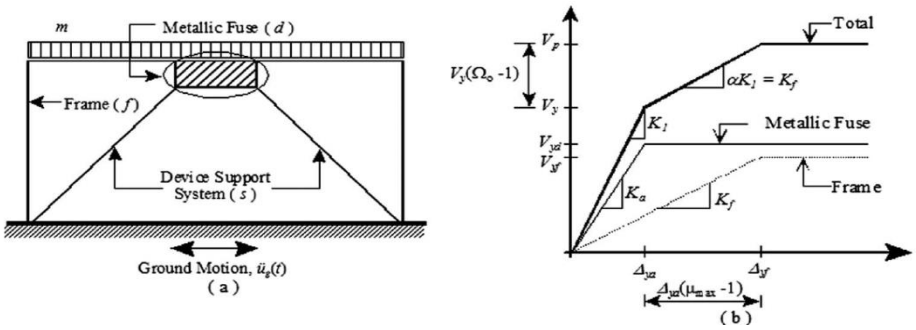

Figure 9. (a) Sample model of an SDOF system with metallic fuses; (b) general pushover curve

SDOF Nonlinear dynamic analyses were conducted using synthetic ground motions to characterize Passive Energy Dissipation (PED) devices. After that, an example showing the proposed design procedure is developed. The authors considered examples for which reference conventional BRBs (taken from SAC joint project) were used as a comparison to metallic fuses (see Figure 9), demonstrating the advantages of implementing such Passive Energy Dissipation Devices (Vargas and Bruneau 2009).

2.2.5. "Seismic Response of Multistory Buildings with Self-Centering Energy Dissipative Steel Braces" (2008)

Robert Tremblay; M. Lacerte; and C. Christopoulos.

The authors presented the results of an analytical study where five steel buildings equipped with different bracing systems were compared. Some of the buildings used self-centering energy dissipative braces (SCED), and the others used buckling restrained braces (BRBs). This comparison aimed to support a hypothesis that smarter structural systems, such as the SCED, are competitive and worth implementation. The force-displacement idealized curves of the systems are shown in Figure 10 (Tremblay et al. 2008).

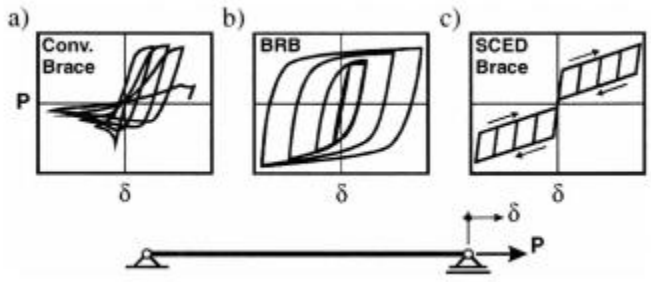

Figure 10. Brace hysteretic response: (a) conventional brace; (b) buckling restrained brace; and (c) SCED brace. (Tremblay et al. 2008)

Detailing for ductility in steel structures usually leads to lower design forces in most seismic codes, because these well-detailed structures are assumed to withstand larger deformations without rupture. However, there are special considerations to account for when dealing with braced steel frames. Attention should be given to damage concentrations at certain story levels and the inability of the system to redistribute loads along the height of the entire structural system (Christopoulos et al. 2002b).

2.2.6. "Self-Centering Energy-Dissipative (SCED) Brace: Overview of Recent Developments and Potential Applications for Tall Buildings" (2014)

J. Erochko and C. Christopoulos

The authors summarize recent advances in self-centering energy dissipative braces, which include the increase of axial and elongation capacity. Such enhancements are under investigation to make the devices more suitable for tall structures. Finally, Erochko and Christopoulos present several configurations where the use of SCED braces could improve the performance of tall buildings (see Figure 11).

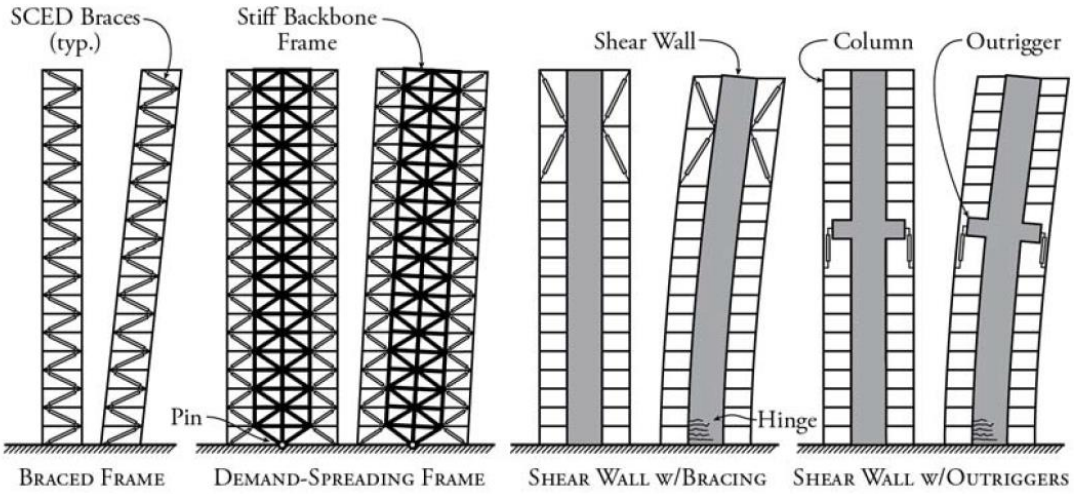

Figure 11. Potential Tall Building Configurations using SCED Braces presented by Erochko and Christopoulos n.d.

2.2.7. "Seismic Assessment of Concentrically-braced Steel Frames with Shape Memory Alloy Braces" (2007)

Jason McCormick, S.; Reginald DesRoches; Davide Fugazza; and Ferdinando Auricchio.

The high self-centering capability of Shape Memory Alloy Braces was exhibited by comparing one three story and one six story conventional steel braced frame with equivalent frames equipped with SMA braces. Maximum interstory drift and residual roof displacement were compared with and without SMA braces. The SMA braces were more effective in the shorter building, and similarly for the first floors of the taller building. For the tall and higher floors, no significant favorable effects were observed (McCormick et al. 2007).

2.2.8. "An innovative seismic bracing system based on a shape memory alloy ring," (2016).

Nan Gao, Jong-Su Jeon, Darel E Hodgson and Reginald DesRoches.

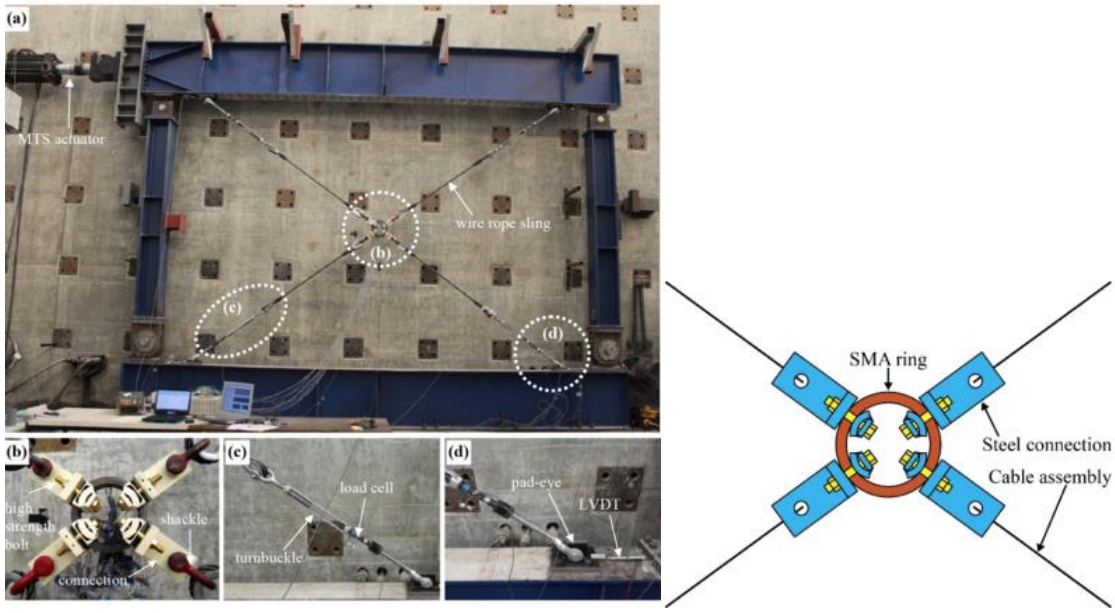

Figure 12. Right: Experimental setup: (a) loading test frame, (b) SMA ring and steel connections, (c) turnbuckle and custom-made load cell, and (d) pad-eye connection and LVDT. Left: a Cross-braced system based on an SMA ring (Gao et al. 2016)

The authors introduced a new bracing system using SMA rings and wires (see Figure 12, right). Analyses were performed using an Abaqus finite element model to simulate the SMA ring behavior. The experimental design used to calibrate the FE model is also shown. The main difference between this study and its predecessors is the adoption of a ring as the key structural component (see Figure 12, left), which Gao et al. argued had a higher capacity (larger sections) and was easier to fabricate than other competing SMA designs. This proposed bracing system showed less self-centering capability compared with previous SMA-based braces, but exhibited larger energy dissipation and lateral stiffness. Gao et al. acknowledged that the system did not perform as expected, and urged that further studies on SMA sensitivity to temperature and loading rate have to be conducted before drawing final conclusions about the capabilities of their bracing system.

2.2.9. "Seismic resistant rocking coupled walls with innovative Resilient Slip Friction (RSF) joints" (2017)

Ashkan Hashemi, Pouyan Zarnani, Reza Masoudnia, Pierre Quenneville.

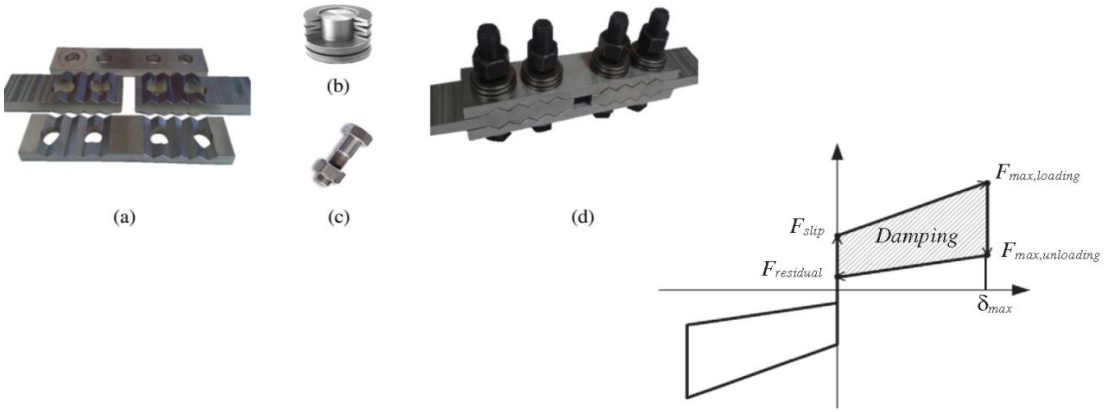

Figure 13. Right: RSF joint: a) Cap plates and slotted center plates b) Belleville springs c) High strength bolts d) Assembly of the joint. Left: Schematic load-deformation loop for the RSF joint.

This study examines the performance of Resilient Slip Friction (RSF) joints when applied to coupling timber walls. The RSF joint, consisting of friction plates with grooves and springs assembled into a compact device (Figure 13), was first introduced by Dr. Zarnani (Provisional patent no.7083, 2015). The device provides the structural system with extra damping and self-centering capabilities. The authors concluded that RDF joints significantly help to dissipate energy through friction. The authors also noted the potential for implementation in steel and reinforced concrete structures (Hashemi et al. 2017).

2.3. Earthquake Loss Assessment

A thorough understanding of strong ground motion effects on societal functionality is a crucially important step toward hazard mitigation. For many years, the structural engineering field was almost exclusively concerned with avoiding casualties during seismic events. As the field became more proficient at this task, efforts have been redirected towards measuring and quantifying socio-economic impacts. One example of primary impacts is the repair cost to return a structure to a safe condition after incurring damage. A secondary effect is the economic impact of business disruption caused by inability to occupy a damaged structure. Would it be economically sound to retrofit particular structures to mitigate potential losses? Would the cost of demolishing and reconstructing the full structure offset any reparability effort? These are questions that joint programs like HAZUS and P-58 developed by FEMA, the NIST Community Resilience Program, and the Resilient Design Institute (RDI), have sought to address for

the last two decades. The following literature highlights the importance of rethinking structural engineering regarding resiliency.

2.3.1. "Lessons from the February 22nd Christchurch Earthquake" (2012)

Helen M. Goldsworthy

This work summarized the main structural flaws observed during the Christchurch earthquake in 2011. There was a direct correlation between the age of the building and the damage incurred. The older the structure, the greater the amount of damage that was observed. This pattern found its explanation in the improved (especially at detailing) new codes that have been implemented (Tremblay et al. 2008). Despite the fact that this work was focused on reinforced concrete structures, it provides valuable insights that can be extrapolated to other kinds of construction, such as soft story failures, damage concentration, and non-structural damage. Goldsworthy concluded by urging the use of displacement-based methods to quantify performance and recommending the adoption of resilient solutions for high importance buildings (Goldsworthy 2012).

2.3.2. "Steel Building Damage from The Christchurch Earthquake Series of 2010 And 2011" (2012)

Charles Clifton, Michel Bruneau, Greg MacRae, Roberto Leon, and Alistair Fussell

Selected steel structures were assessed to quantify damage suffered due to the robust and successive ground motions. Special focus was placed on eccentrically braced frames and moment resisting frames.

The preferred structural material for building construction in Christchurch has historically been reinforced concrete due to easy access to aggregates in the area. Therefore, by 2010 when the first strong earthquake happened, most relevant steel structures had been built recently (Goldsworthy 2012). Overall, these steel structures showed outstanding performance at the life-safety level because they met the most current code standards.

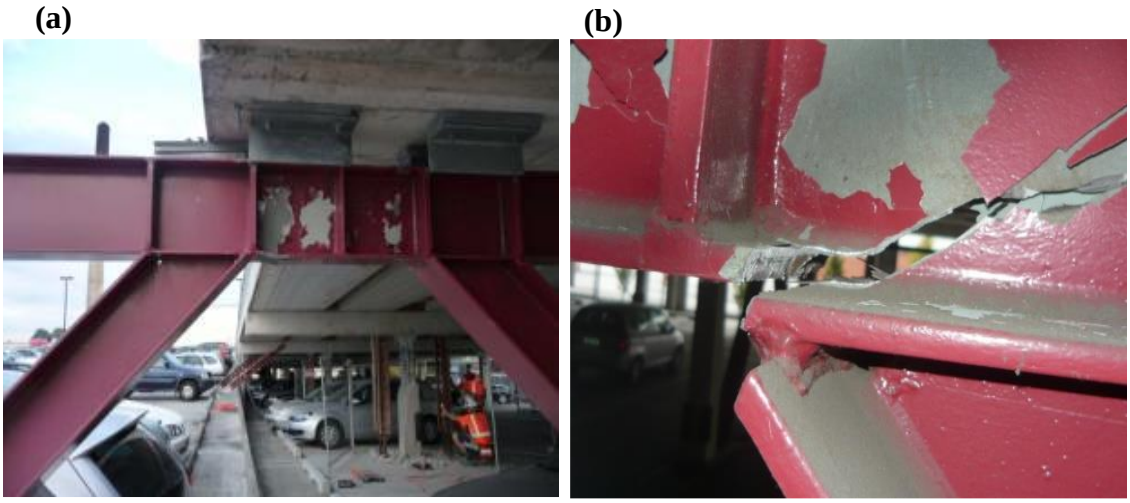

Figure 14. Christchurch parking lot [Photos by M. Bruneau]; (a) inelastic deformations at top level EBF; (b) Fractured link at lower level EBF. (Clifton et al. 2011)

Steel-frame connections generally performed as expected. Eccentrically-braced frames also showed satisfactory response with limited exceptions where link fracture was observed (see Figure 14b). On the other hand, concentrically-braced frames commonly experienced brace fractures (see Figure 15).

The steel structures' overall performance has encouraged Christchurch authorities to implement more steel construction and to increase the research and development of innovative self-centering devices to reduce downtime, building content losses, and non-structural damage.

Figure 15. Low-rise CBF parking garage [Photos by M. Bruneau]. (a) Buckled brace; (b) Fractured non-ductile brace-to-column connection (Clifton et al. 2011).

2.3.3. "Estimation of Seismic Acceleration Demands in Building Components" (2004)

Shahram Taghavi, Eduardo Miranda

Figure 16. Acceleration-sensitive nonstructural components (Taghavi, Shahram; Miranda 2004).

Generally, after a strong ground motion, nonstructural damage represents a significant portion of the total cost of building repair. Thus, Taghavi and Miranda

conducted a parametric study supporting the efficacy of their method to estimate accelerations demands. The study explores sensitivities of the floor peak acceleration demand to parameters like the natural period (Tn), damping (ξ), and stiffness ratio (α). The results suggested that both the Tn and α affect the acceleration demands considerably while reducing stiffness along the height of the building was not influential (Taghavi, Shahram; Miranda 2004).

CHAPTER 3. OBJECTIVES AND SCOPE.

3.1. Objectives

To identify preferable characteristics for a hyperelastic fuse, the following research objectives were selected.

- Identify beneficial combinations of the hyperelastic component parameters (i.e. stiffness, ductility, elastic buckling force), that provide superior or comparable mechanical responses to those of conventional hysteretic systems. Performance was evaluated based on peak mechanical force and displacements.
- Perform earthquake loss assessment estimates to evaluate the competitiveness of hyperelastic systems compared to hysteretic systems available in current practice, such as Buckling Restrained Braces (BRBs). These evaluations were conducted regarding earthquake mainshock repair cost.

3.2. Scope

The extent of this work is limited as follows:

- Buildings with significant irregularities and thus torsional and higher mode effects are not considered. Therefore, simplified SDOF models were reasonably representative for the analyses.
- The prototype buildings used in the study were assumed to be located in high seismicity areas. Specifically, Los Angeles, CA was used as the referenced location in this work.
- Steel-braced, low-rise buildings, with a natural period (Tn) ranging from 0.1 to 0.4 seconds.

- The multi-linear behavior of the hyperelastic system was characterized using three stiffness categories: initial (K_0), buckled (K_2), and arresting (K_3).
- Comparable hyperelastic and hysteretic systems were assumed to have equal initial stiffnesses (K_0).
- It is intended that all lateral loads have to be resisted by the braces exclusively. Hence, all building connections are pinned (i.e. column-foundation, beam-column, brace-column.)
- Second order effects (P-Delta) were not explicitly addressed.

CHAPTER 4. METHODOLOGY

Over 1500 single degree of freedom (SDOF) analyses were carried out using various combinations of constitutive parameters and nonlinear time history methods with a suite of scaled ground motions. The analyses sought to identify beneficial combinations of hyperelastic component parameters. The findings present hyperelastic system performance in context relative to performance available from an alternative hysteretic system. Hyperelastic models were parameterized with respect to a buckling force limit, ductility to an arresting stiffening branch, and the ratio of arresting to initial stiffness. Four low-rise, concentrically-braced, buildings were used as prototypes for the comparisons. These structures were modeled as SDOFs by isolating the first mode response.

Performance is quantified in terms of direct capital-related loss, defined as the repair expenses as a percentage of total building replacement cost (total cost of structure, nonstructural components, and contents). Moreover, sensitivities of loss measures to hyperelastic characteristics were examined with respect to nonlinear dynamic ground motion response using a representative suite of ground motions for Southern California.

4.1. Prototype Buildings

This study was conducting using structural characteristics representative of single- and three-story, concentrically-braced frame (CBF) buildings that might be found in metropolitan Los Angeles or sites with similar seismic demands.

Preliminary design for prototype buildings was performed to satisfy ASCE 7-10 seismic requirements for new commercial office buildings. Ordinary (OCBFs) and

Special (SCBFs) seismic detailing scenarios were selected as baseline hysteretic options to explore design ductility influence on the relative performance of hysteretic and hyperelastic systems. Hence, four prototype buildings were examined as shown in Table 1:

Table 1. Prototype buildings (CASES)

Nº. of Stories	**Seismic Detailing**	
	Ordinary	**Special**
1	CASE C	CASE A
3	CASE D	CASE B

A building plan and elevation were adapted from the 3-story LA building (see Figure 17) reported by the SAC Joint Venture (FEMA 2000). Floor dimensions were 80 x 120 ft (24x36 m) for all buildings. Floor framing spans were 20 ft (6 m) in both directions. The bold lines in Figure 17a represent the braced frame locations (A3-6, E3-6, 1A-D, and 7A-D). Story heights were 13 ft (4 m) for both 1-story and 3-story buildings (see Figure 17b Figure 17c).

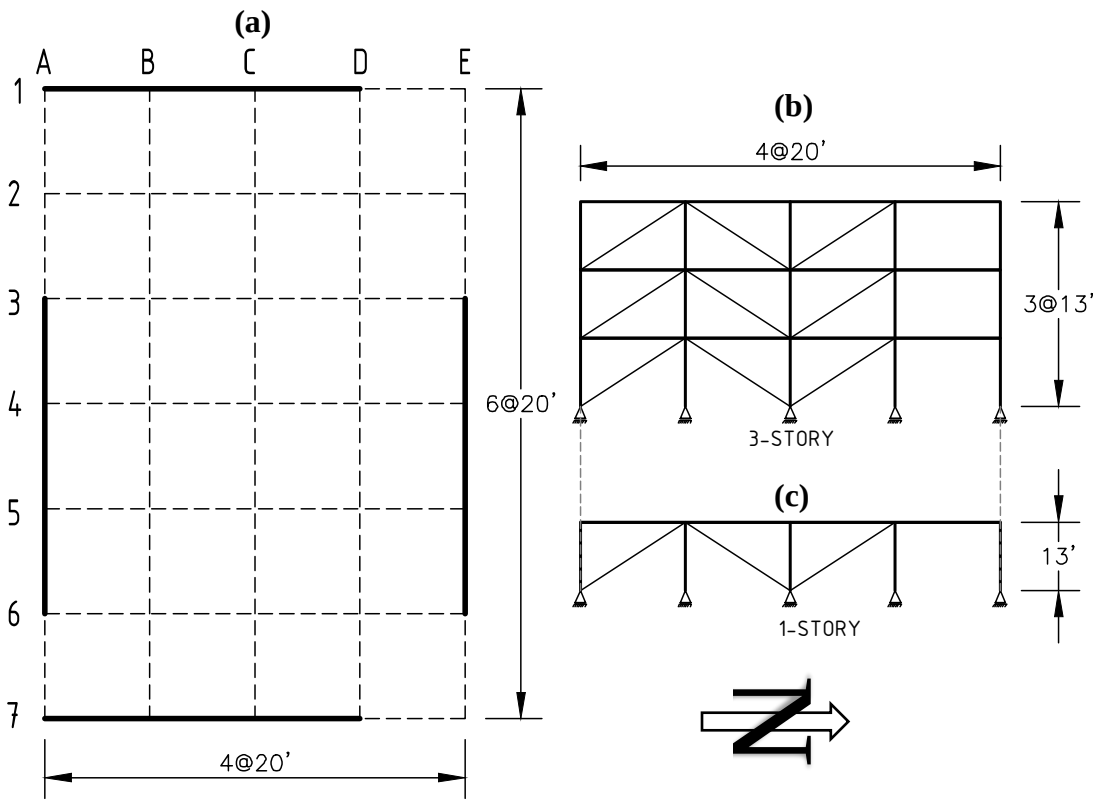

Figure 17. Prototype Buildings. (a) Plan view; (b) 3-Story Elevation view; (c) 1-Story Elevation view

4.2. Design of Prototype Buildings

Preliminary analyses were performed using SAP2000 (see Figure 18), in which all floors were assumed to have a total dead load (self plus superimposed weight) of 100 lb/ft^2 (488 kg/m^2). The study considered a uniform live load of 80 lb/ft^2 (390 kg/m^2). These loads approximately represent the concrete on steel deck flooring (~50 psf), partitions (~25 psf), ceiling (~7psf), supporting steel floor framing (~18psf), office personnel traffic (~50 psf), and furniture of commercial office buildings (~30 psf). All columns and beams were assumed to be W-shapes A992 Grade 50 steel, and all braces were assumed to be HSS with A500 Grade B steel. All load combinations related to the

dead, live, and earthquake load cases were considered for both analysis and design. All elements' boundary conditions were pinned (no moments).

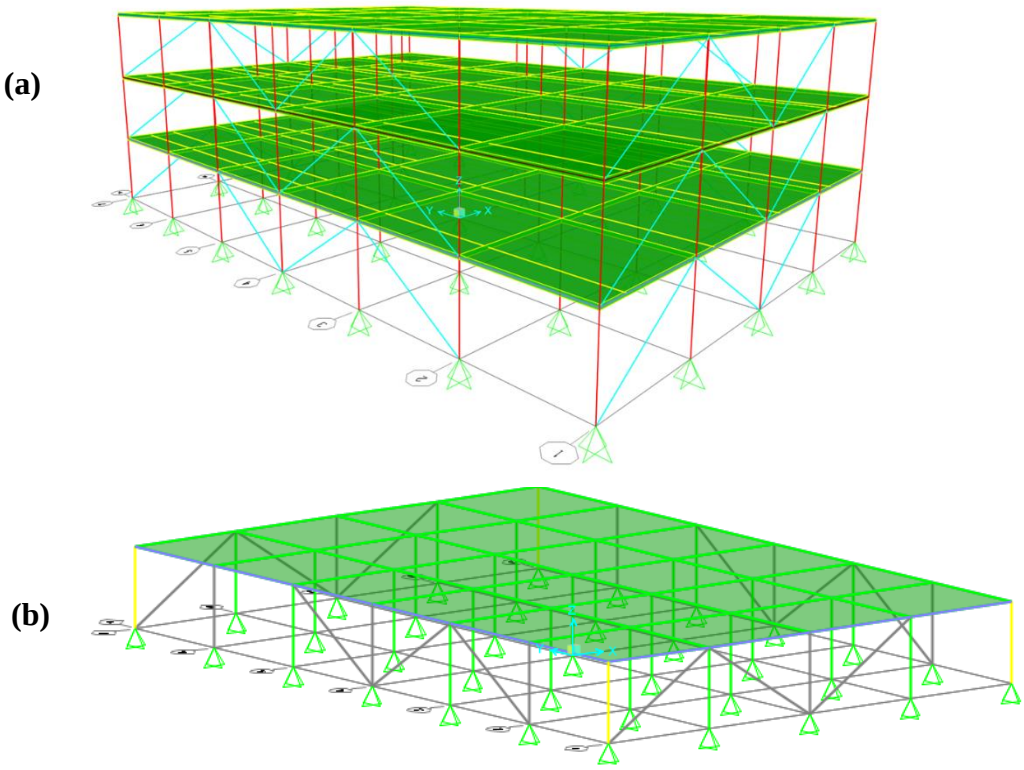

Figure 18. 3D analysis models; SAP2000; (a) 3-Story; (b) 1-Story

4.2.1. Equivalent Lateral Force (ELF)

Figure 17 shows that the lateral force resisting system of the buildings is symmetric and orthogonal, which permits uncoupling the braced frames' contributions to the LFRS. In this context, the buildings' nature (short, symmetric, and orthogonal) validates the applicability of the ELF procedure to design all prototype buildings (ASCE/SEI 2010).

4.2.2. Response Modification Coefficient R.

The CBFs under consideration are either Ordinary or Special with respect to seismic detailing. Therefore, the two base response modifications factors (R) used were 3.25 and 6, respectively, as shown in Table 2.

Table 2. Design Coefficients and Factors for Seismic Force-Resisting Systems of the ASCE/SEI 2010.

Table 12.2-1 Design Coefficients and Factors for Seismic Force-Resisting Systems

Seismic Force-Resisting System	ASCE 7 Section Where Detailing Requirements Are Specified	Response Modification Coefficient, R[a]	Overstrength Factor, Ω_0[g]	Deflection Amplification Factor, C_d[b]	Structural System Limitations Including Structural Height, h_n (ft) Limits[c] Seismic Design Category				
					B	C	D[d]	E[d]	F[e]
B. BUILDING FRAME SYSTEMS									
1. Steel eccentrically braced frames	14.1	8	2	4	NL	NL	160	160	100
2. Steel special concentrically braced frames	14.1	6	2	5	NL	NL	160	160	100
3. Steel ordinary concentrically braced frames	14.1	3¼	2	3¼	NL	NL	35[i]	35[i]	NP[i]

4.2.2.1. Design Category, Spectral Accelerations (S_{DS} and S_{D1})

Based on the site conditions assumed (Site Class D, Los Angeles) and the risk category of typical commercial office buildings (II), the USGS U.S. Seismic Design Maps provided a design spectral acceleration in the short period range (S_{DS}) of 1.36 g and design spectral acceleration at 1 second (S_{D1}) of 0.717 g. Accordingly, the prototype buildings fall in the most severe design category, D, in accordance with Table 11.6-1 and 11.6-2 (ASCE/SEI 2010; USGS 2015).

4.2.2.2. Approximate Period

In order to compute the seismic load distribution by the ELF method, approximate periods had to first be calculated. Approximate periods were calculated using ASCE equation (12.8-7)

$$T_a = C_t * h_n^x,$$

where, according to Table 3, $C_t = 0.02$; $x = 0.75$; *and* $h_n =$ *building height* $[ft]$. For instance, for the 3-story building $T_{a2} = 0.02 * 39^{0.75} = 0.312\ sec$; while for the 1-Story building $T_{a1} = 0.137$ sec.

Table 3. ASCE 7-10 Parameters to compute Approximate Period.

Table 12.8-2 Values of Approximate Period Parameters C_t and x

Structure Type	C_t	x
Moment-resisting frame systems in which the frames resist 100% of the required seismic force and are not enclosed or adjoined by components that are more rigid and will prevent the frames from deflecting where subjected to seismic forces:		
Steel moment-resisting frames	0.028 (0.0724)[a]	0.8
Concrete moment-resisting frames	0.016 (0.0466)[a]	0.9
Steel eccentrically braced frames in accordance with Table 12.2-1 lines B1 or D1	0.03 (0.0731)[a]	0.75
Steel buckling-restrained braced frames	0.03 (0.0731)[a]	0.75
All other structural systems	0.02 (0.0488)[a]	0.75

[a]Metric equivalents are shown in parentheses.

4.2.2.3. Vertical Distribution of Lateral Loads

Preliminary design base shear (V) was computed as follows. First, base shear coefficients (C_s) were determined for each prototype structure:

$$C_S = \frac{S_{DS} * I_e}{R} \leq \frac{S_{D1} * I_e}{R * T} \quad for\ T \leq T_L$$

Where:

$$SD1 = 0.717\ g$$

$$SDS = 1.360\ g$$

$$TL = 8\ seconds$$

For the 3-story building ($T_n \approx 0.312$ sec) with high ductility (R = 6):

$$C_S = \frac{1.36 * 1}{6} \leq \frac{0.717 * 1}{6 * 0.312}$$

$$C_S = 0.22667 \leq 0.3829$$

$$\boldsymbol{C_S = 0.22667}$$

Check if $C_S > 0.044 * SD_S * I_e \geq 0.01$

$$C_S > 0.044 * 1.360 * 1 \geq 0.01$$

$$C_S > 0.05984 \geq 0.01$$

Because $S_{D1} = 0.717 \geq 0.6\ g$, it is required to check that $C_S \geq \frac{0.5 * S_1 * I_e}{R}$

$$C_S \geq \frac{0.5 * 0.717 * 1}{6}$$

$$C_S \geq 0.0598$$

Then the $\boldsymbol{C_S}$ for the 3-story building with special seismic design (R=6) equals:

$$\boldsymbol{C_S = 0.2267}$$

Performing a similar analysis for the other three prototype building confirmed that all cases were governed by the acceleration-controlled region of the elastic design spectrum. The design $\boldsymbol{C_S}$ values were as shown in Table 4:

Table 4. Seismic Response Coefficients (Cs) for all Prototype Buildings

3-story SCBF (R = 6)	**One story – SCBF (R = 6)**	**Three story – OCBF (R = 3.25)**	**One story – OCBF (R = 3.25)**
0.2267	0.2267	0.4185	0.4185

After inputting these C_s values into the corresponding SAP 2000 models, the base shears were computed and subsequently distributed through the structures' height as equivalent lateral forces. The general equation for seismic base shear is found from the product of the seismic response coefficient (Cs) and the seismic weight (W, i.e., the assumed dead load of each structure):

$$V = C_S * W,$$

While the vertical distribution of lateral forces computed by the program used the following equations:

$$F_i = C_{vi} * V,$$

where:

$$C_{vi} = \frac{W_i * h_i^k}{\sum_{j=1}^{N} W_j * h_j^k}$$

$$k = 1 \; for \; T \leq 0.5s;$$

$$k = 2 \; for \; T => 2.5s;$$

$$k = linear \; interpolation \; between \; 1 \; and \; 2 \; for \; T = 0.5 - 2.0s$$

Furthermore, after designing the buildings using SAP2000 (beam, columns, and braces) to satisfy the AISC requirements and obtaining the final natural periods, they were checked to be less than $T_{SAP2000} \leq C_u * Ta$.

$$T_{SAP2000} \leq C_u * Ta = 1.4 * 0.312 = 0.44 \; sec$$

Where; $C_u = 1.4$ from *Table 5*.

$$T_{SAP2000} = 0.4 \leq 0.44 \; sec \; \textbf{\textit{OK!}}$$

.

Table 5. ASCE 7-10 Upper Limit on Calculated Period (from Table 12.8-1).

Design Spectral Response Acceleration Parameter at 1 s, S_{D1}	Coefficient C_u
≥ 0.4	1.4
0.3	1.4
0.2	1.5
0.15	1.6
≤ 0.1	1.7

The final calculated periods are listed in Table 6.

Table 6. Natural Periods of Prototype Buildings

Parameters under Evaluation	**Period Tn [s]**			
	3-story SCBF (R = 6)	**1 story – SCBF (R = 6)**	**3 stories – OCBF (R = 3.25)**	**1 story – OCBF (R = 3.25)**
$C_u * Ta$	0.44	0.20	0.44	0.19
X direction	0.40	0.21	0.32	0.18
Y direction	0.40	0.20	0.29	0.17
Tn SDOF	**0.40**	**0.20**	**0.31**	**0.17**

4.3. Prototype Buildings Simplification to Single Degree of Freedom (SDOF) Systems

Once all columns, beams, and braces were proportioned to meet preliminary strength design requirements, the 3-story buildings were converted into equivalent SDOF systems by using the modal participation factor to isolate the first mode response. The analysis of MDOF systems (3-story cases) based on a single mode is valid because more than 90% of the seismic mass participated effectively in the first mode. Additionally, the symmetry of the buildings suppresses torsional effects. The equivalent SDOF systems consist of an effective modal mass (M_{sdof}), and effective modal height (h_{sdof}) (damping:

5% of the critical). This simplification is illustrated in Figure 19, an illustration from the book “Dynamics of Structures” by Anil K. Chopra, 2012.

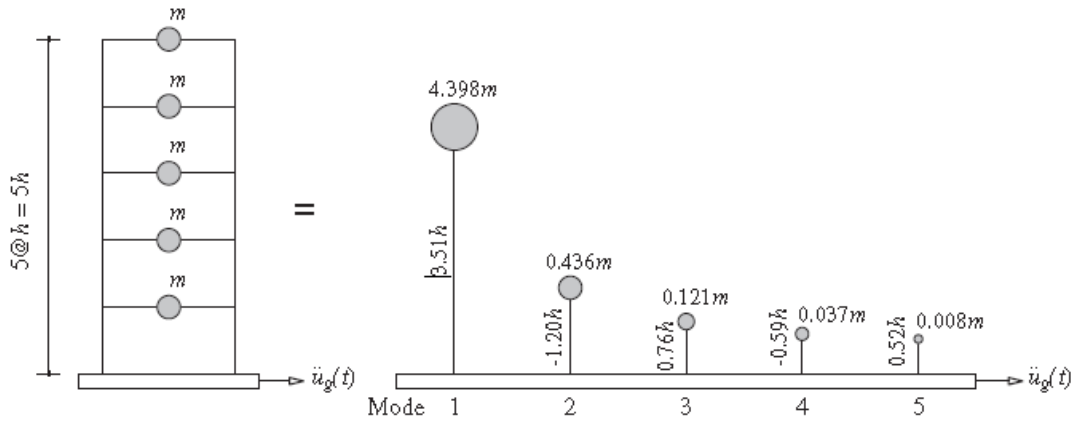

Figure 19. Chopra illustration for effective modal masses and heights (Chopra 2012).

The floor seismic mass of the buildings (labeled ‘m’ in Figure 19) was computed by factoring the floor area times the distributed dead load, $m = A_{floor} * DL$. With the stiffness and mass matrices assembled, natural frequencies and mode shapes were computed through the eigenvalue formulation. After that, modal participation factors and SDOFs masses ($\mathbf{m_{SDOF}}$) were calculated. Representative modal stiffnesses were calculated using natural periods and modal masses from SAP2000.

A summary of the SDOF characteristics systems considered in this study is presented below (Table 7).

Table 7. Summary table equivalent SDOF systems

Calculated Parameters	Equations	3-story- High Ductility (R = 6)	1 story – High Ductility (R = 6)	3 stories – Low Ductility (R = 3.25)	1 story – Low Ductility (R = 3.25)
m_{SDOF} [kg]	$\Gamma_1 * \sum_j m_j \Phi_{1j}$	891781	297260	891781	297260
ω_{n_SDOF}	Eigen Value	15.7	31.4	20.2	36.9
T_{n_SDOF} [sec]	$\frac{2\pi}{\omega_n}$	0.4	0.2	0.31	0.17
K_{0_SDOF} [N/m]	$\omega_n{}^2 * m_{SDOF}$	220038142	293383860.4	366348623.6	406067627
ξ [% of C_R]	$\frac{C}{2 * m_{SDOF} * \omega_n}$	5	5	5	5

4.4. Ground Motions

A suite of 16 records was selected to match some of those considered in the "*Seismic response of self-centring hysteretic SDOF systems"* conducted by professors Chirstopolous et al. in 2001. The ground motions were scaled to a target 5% damped elastic design spectrum for soil type D conditions in Los Angeles area. These historically strong ground motions were used to evaluate the seismic performance of all prototype buildings. The scaled suite is intended to represent earthquakes with a probability of exceedance of 10% in a 50-year hazard level, approximated as 2/3 of the MCE (maximum considered earthquake), consistent with ASCE 7-10. (FEMA 2000; Tremblay et al. 2008).

The motions were obtained from the NGA-West2 on-line Ground-Motion Database created by experts at the Pacific Earthquake Engineering Research Center (PEER) (Ancheta et al. 2013). Table 8 and Table 9 present the main characteristics of the ground motions used in this study.

Table 8. Ground Motions (Metadata)

#	Matlab ID	Magnitude	Spectral Ordinate	time step (sec)	Mechanism
1	CENTROH1	6.54	H1	0.005	strike slip
2	CENTROH2	6.54	H2	0.005	strike slip
3	PLASTERH1	6.54	H1	0.01	strike slip
4	PLASTERH2	6.54	H2	0.01	strike slip
5	BRAH1	6.54	H1	0.01	strike slip
6	BRAH2	6.54	H2	0.01	strike slip
7	mulholH1	6.69	H1	0.01	Reverse
8	mulholH2	6.69	H2	0.01	Reverse
9	glandaleH1	6.69	H1	0.01	Reverse
10	glandaleH2	6.69	H2	0.01	Reverse
11	CanogaH1	6.69	H1	0.01	Reverse
12	CanogaH2	6.69	H2	0.01	Reverse
13	CapitolaH1	6.93	H1	0.005	Reverse Oblique
14	CapitolaH2	6.93	H2	0.005	Reverse Oblique
15	fortunaH1	7.01	H1	0.02	Reverse
16	fortunaH2	7.01	H2	0.02	Reverse

Ground motions were scaled by minimizing Sum of Squared Errors (SSE) between the target design spectrum of each motion and the 5% damped elastic response spectrum at 0.1, 0.25, 0.5, 1, and 2 seconds periods. The sum of the square error is represented by SSE_t in the equation below, while S_{motion} and S_{target} correspond to the scaled spectral acceleration and design spectral accelerations at a particular period, T_n, respectively.

$$SSE_t = \sum_{Tn=0.1,0.2,0.5,1,2} (S_{motion} - S_{target})^2$$

Figure 20 shows the sum of squared errors for each ground motion record plotted versus scaling factor. From this figure, scaling factors can be identified by selecting the value corresponding to the lowest error for each motion. For instance, for the BRAH1 motion, a scaling factor of 4 would render the minimum dispersion in accelerations between the target and response spectra at the periods noted above.

Scaling factors are reported in the last column of Table 9 for each ground motion. Additionally, the response spectrums of the scaled motions are plotted against the target design spectrum for visual comparison in Figure 21.

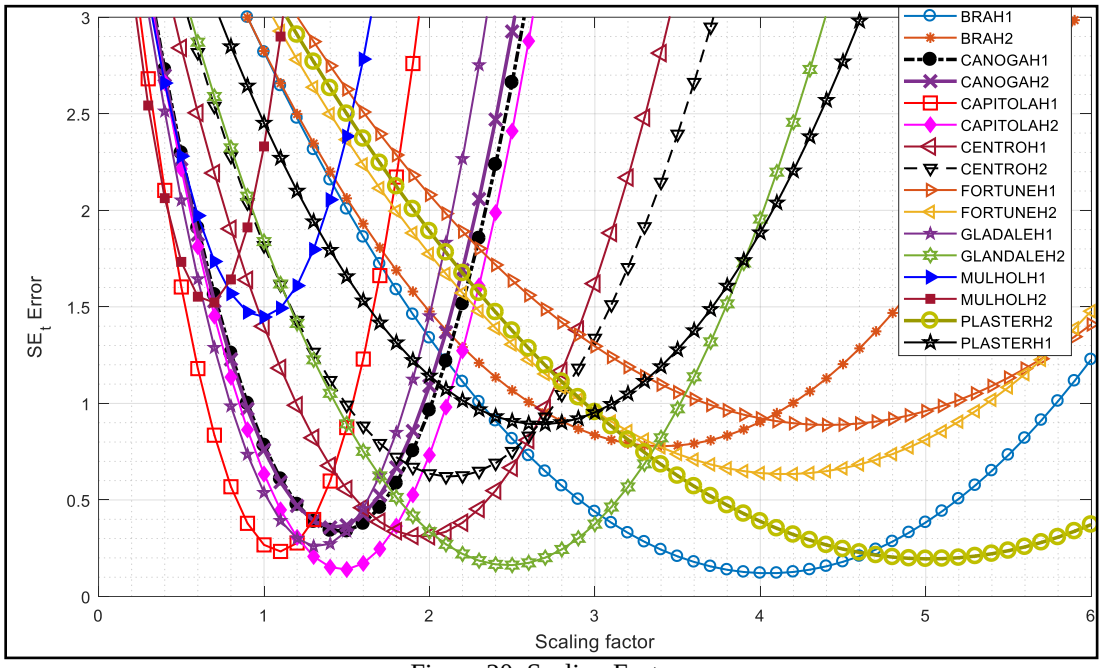

Figure 20. Scaling Factors

Each recorded direction was considered separately in analyses (as obtained from the PEER strong motion database). Moreover, the end of all of the records was filled with 20 zeros to measure residual displacements accurately; this created a free vibration phase until the damping abates inertial effects.

Table 9. Ground Motions' Scaling Factors

#	Matlab ID	Record	Earthquake Name	Year	Station Name	Vs30 (m/sec)	Scale Factor
1	CENTROH1	RSN721-ICC000	Superstition Hills-02	1987	El Centro Imp. Co. Cent	192.05	2
2	CENTROH2	RSN721-ICC090	Superstition Hills-02	1987	El Centro Imp. Co. Cent	192.05	2.1
3	PLASTERH1	RSN724-PLS045	Superstition Hills-02	1987	Plaster City	316.64	5
4	PLASTERH2	RSN724-PLS135	"Superstition Hills-02"	1987	Plaster City	316.64	2.7
5	BRAH1	RSN719 - BRA225	Superstition Hills-02	1987	Brawley Airport	208.71	4
6	BRAH2	RSN719-BRA315	Superstition Hills-02	1987	Brawley Airport	208.71	3.4
7	mulholH1	RSN953-MUL009	Northridge-01	1994	Beverly Hills - 14145 Mulhol	355.81	1
8	mulholH2	RSN953-MUL279	Northridge-01	1994	Beverly Hills - 14145 Mulhol	355.81	0.7
9	glandaleH1	RSN974-GLP177	Northridge-01	1994	Glendale - Las Palmas	371.07	1.3
10	glandaleH2	RSN974-GLP267	Northridge-01	1994	Glendale - Las Palmas	371.07	2.5
11	CanogaH1	RSN959-CNP106	Northridge-01	1994	Canoga Park - Topanga Can	267.49	1.5
12	CanogaH2	RSN959-CNP196	Northridge-01	1994	Canoga Park - Topanga Can	267.49	1.4
13	CapitolaH1	RSN752-CAP000	Loma Prieta	1989	Capitola	288.62	1.1
14	CapitolaH2	RSN752-CAP090	Loma Prieta	1989	Capitola	288.62	1.5
15	fortunaH1	RSN827-FOR000	Cape Mendocino	1992	Fortuna - Fortuna Blvd	457.06	4.4
16	fortunaH2	RSN827-FOR090	Cape Mendocino	1992	Fortuna - Fortuna Blvd	457.06	4.2

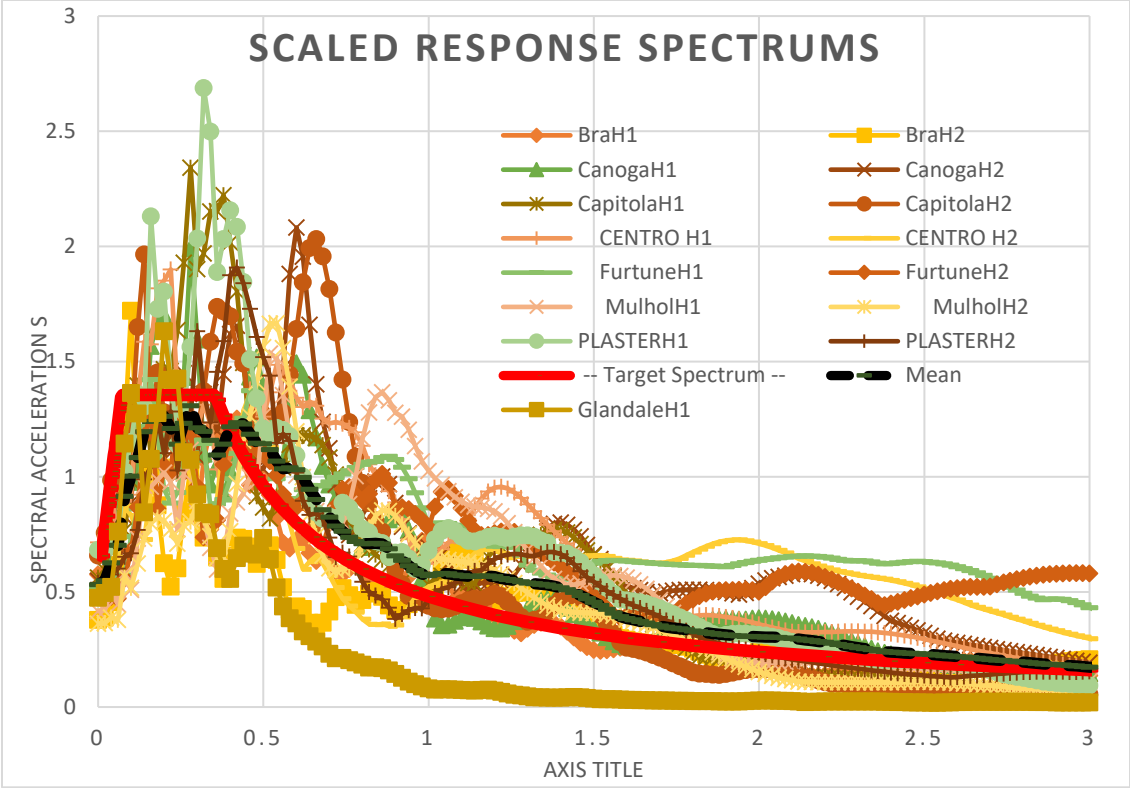

Figure 21. Elastic Spectrums of Scaled Ground Motions

4.5. Earthquake Estimates of Direct Physical Building Damage

This section is based on the Hazus® –MH 2.1 Technical Manual for multi-hazard loss estimation methodology, especially chapter 5 (“Direct Physical Damage”). Here, building damage caused by a strong ground motion is measured as the cumulative probability of being in or exceeding a damaged state (slight, moderate, extensive, or complete). This procedure is supported on the same principles as performance-based engineering described extensively in the FEMA 273 and the ATC-40 (FEMA 2015).

4.5.1. Fragility Curves

Fragility curves represent the cumulative distribution function (CDF) of the logarithm of an engineering demand parameter, such as spectral displacement (S_d) or

spectral acceleration (S_a). In other words, these curves (see Figure 22) represent the vulnerability in terms of probability of a building being in or exceeding a particular damage state. For instance, in Figure 22, a building with 5 inches of peak displacement would have approximately 100%, 50%, 5%, and 0% probabilities of exceeding the slight, moderate, extensive, or complete damage stages, respectively.

Regarding the engineering demand parameters, the direct economic loss module of HAZUS-MH uses displacement to assess damage to structural and drift-sensitive nonstructural components. Whereas, acceleration is used to calculate acceleration-sensitive nonstructural damage and contents losses.

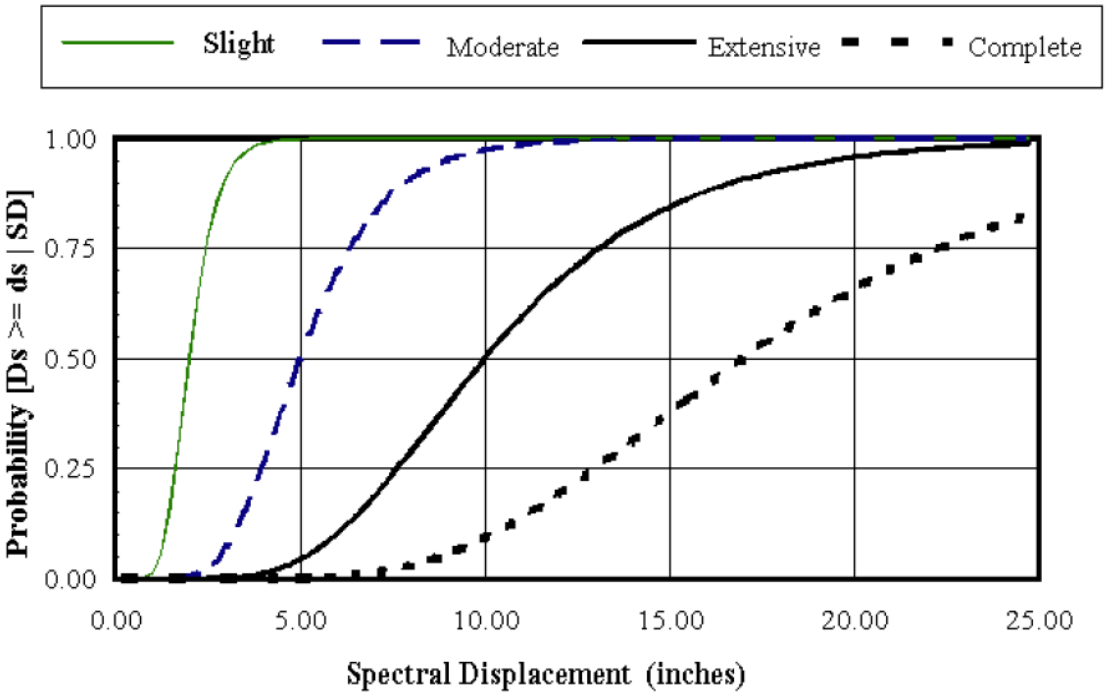

Figure 22 HAZUS-MH Example of Fragility Curves for Slight, Moderate, Extensive and Complete Damage

The probability of being in or exceeding a damage state is given by the equation below, which was taken from HAZUS-MH technical manual, page 1-40.

$$P[ds|S_d] = \Phi\left[\frac{1}{\beta_{ds}}\ln\left(\frac{S_d}{S_{d,ds}}\right)\right]$$

where:

$\boldsymbol{S_{d,ds}}$**:** the median value of spectral displacement at which the building reaches the threshold of the damage state, ds.

$\boldsymbol{\beta_{ds}}$**:** the standard deviation of the natural logarithm of spectral displacement of damage state, ds.

$\boldsymbol{\Phi}$**:** the standard normal cumulative distribution function.

All prototype building structures were labeled as S2L, which stands for the low-rise steel-braced frame (see Table 10). Moreover, because buildings were assumed to be commercial, the corresponding occupancy classification was COM4, which stands for offices offering technical or professional services. Structure classifications determine damage state thresholds, and occupancy classifications determine relative proportions of building value associated with structural and nonstructural components and contents.

Table 10. Building Model Classification (from Table 3.1 HAZUS-MH).

No.	Label	Description	Height			
			Range		Typical	
			Name	Stories	Stories	Feet
6	S2L	**Steel Braced Frame**	Low-Rise	1 - 3	2	24
7	S2M		Mid-Rise	4 - 7	5	60
8	S2H		High-Rise	8+	13	156

Table 11. Building occupancy classification (from Table 3.2 HAZUS-MH)

Label	Occupancy Class	Example Descriptions
	Commercial	
COM1	Retail Trade	Store
COM2	Wholesale Trade	Warehouse
COM3	Personal and Repair Services	Service Station/Shop
COM4	Professional/Technical Services	Offices
COM5	Banks	
COM6	Hospital	
COM7	Medical Office/Clinic	
COM8	Entertainment & Recreation	Restaurants/Bars
COM9	Theaters	Theaters
COM10	Parking	Garages

Fragility curve parameters ($S_{d,ds}$, β_{ds}) were selected to corresponded to high-code seismic design and construction, which is appropriate for modern construction in a high seismic region such as Los Angeles. Fragility parameters were used as appropriate per the HAZUS loss estimation methodology to assess structural versus nonstructural component damage. Excerpts from the HAZUS-MH Technical Manual are provided in Table 12, Table 13, and Table 14 highlighting the lognormal damage state parameters for structural, drift-sensitive nonstructural, and acceleration-sensitive nonstructural components, respectively.

Table 12. Structural Fragility Curve Parameters for High-Code seismic design level (from Table 5.9a HAZUS-MH)

Building Properties			Spectral Displacement (inches)							
Type	Height (inches)		Slight		Moderate		Extensive		Complete	
	Roof	Modal	Median	Beta	Median	Beta	Median	Beta	Median	Beta
W1	168	126	0.50	0.80	1.51	0.81	5.04	0.85	12.60	0.97
W2	288	216	0.86	0.81	2.59	0.88	8.64	0.90	21.60	0.83
S1L	288	216	1.30	0.80	2.59	0.76	6.48	0.69	17.28	0.72
S1M	720	540	2.16	0.65	4.32	0.66	10.80	0.67	28.80	0.74
S1H	1872	1123	3.37	0.64	6.74	0.64	16.85	0.65	44.93	0.67
S2L	288	216	1.08	0.81	2.16	0.89	6.48	0.94	17.28	0.83
S2M	720	540	1.80	0.67	3.60	0.67	10.80	0.68	28.80	0.79
S2H	1872	1123	2.81	0.63	5.62	0.63	16.85	0.64	44.93	0.71

Table 13. Nonstructural Drift-Sensitive Fragility Curve Parameters for High-Code Seismic Design Level (from Table 5.11 HAZUS-MH)

Building Type	Median Spectral Displacement (inches) and Logstandard Deviation (Beta)							
	Slight		Moderate		Extensive		Complete	
	Median	Beta	Median	Beta	Median	Beta	Median	Beta
S2L	0.86	0.84	1.73	0.90	5.40	0.97	10.80	0.92
S2M	2.16	0.71	4.32	0.74	13.50	0.74	27.00	0.84
S2H	4.49	0.71	8.99	0.71	28.08	0.72	56.16	0.78

Table 14 Nonstructural Acceleration-Sensitive Fragility Curve Parameters -High-Code Seismic Design Level (from Table 5.13a HAZUS-MH)

Building Type	Median Spectral Acceleration (g) and Logstandard Deviation (Beta)							
	Slight		Moderate		Extensive		Complete	
	Median	Beta	Median	Beta	Median	Beta	Median	Beta
S2L	0.30	0.67	0.60	0.67	1.20	0.67	2.40	0.67
S2M	0.30	0.69	0.60	0.66	1.20	0.66	2.40	0.66
S2H	0.30	0.68	0.60	0.66	1.20	0.65	2.40	0.65

Once the probabilities of reaching each particular limit state have been computed, they are converted into Percentage of Total Building Replacement Cost (% TBRC). The factors used for this conversion were derived from statistical data associated with building occupancy. The repair cost conversion factors are shown in Table 15, Table 16, and Table 17 for structural, nonstructural acceleration-sensitive, and nonstructural drift-sensitive components, respectively.

Table 15. Drift-sensitive Non-structural Repair Costs [% TBRC] (from HAZUS-MH table 15.2).

No.	Label	Occupancy Class	Structural Damage State			
			Slight	Moderate	Extensive	Complete
15	COM4	Professional/Technical/ Business Services	0.4	1.9	9.6	19.2

Table 16. Acceleration-sensitive Non-structural Repair Cost Ratios [% TBRC] (from HAZUS-MH table 15.3).

No.	Label	Occupancy Class	Acceleration Sensitive Non-structural Damage State			
			Slight	Moderate	Extensive	Complete
15	COM4	Professional/Technical/ Business Services	0.9	4.8	14.4	47.9

Table 17. Structural Repair Cost Ratios [% TBRC] (from HAZUS-MH table 15.4).

No.	Label	Occupancy Class	Drift Sensitive Non-structural Damage State			
			Slight	Moderate	Extensive	Complete
15	COM4	Professional/Technical/ Business Services	0.7	3.3	16.4	32.9

On the other hand, strong ground motions can also induce damage to building contents. Therefore, contents losses were taken into account for all analyses. Contents include any equipment or furniture that is not integrally attached to the structure, such as computers, screens, and projectors. Contents damage is usually associated with building accelerations. Therefore, quantifying contents damage can be related to the nonstructural acceleration-sensitive estimations. For this task, FEMA developed Table 18 to estimate contents losses based on the state of nonstructural acceleration-sensitive damage.

Table 18. Contents Damage Ratios (in % of contents replacement cost) (from Table 5.15 HAZUS-MH)

No.	Label	Occupancy Class	Acceleration Sensitive Non-structural Damage State			
			Slight	Moderate	Extensive	Complete*
		Commercial				
12	COM1	Retail Trade	1	5	25	50
13	COM2	Wholesale Trade	1	5	25	50
14	COM3	Personal and Repair Services	1	5	25	50
15	COM4	Professional/Technical/ Business Services	1	5	25	50

An example to clarify this process is presented in Table 19. Here, loss estimates for structural (STR), nonstructural drift-sensitive (NS_{DS}), nonstructural acceleration-sensitive (NS_{AS}), and contents of an example structure are calculated using the HAZUS-MH methodology. For this task, $P[ds|S_d]$ equation (page 42) was applied three times. The inputs were the spectral (peak) displacement (S_d) for STR and NS_{DS} loss projections, and the spectral (peak) acceleration (Sa) for NS_{AS} loss assessments. For all cases the values of $\boldsymbol{S_{d,ds}}$ (S_{d_bar}) and $\boldsymbol{\beta_{ds}}$(beta) are found in Table 12, Table 13, and Table 14. Once the probability of being in or exceeding a limit state is determined (P_E), the probability of not reaching such a state of damage (P_{DS}) can be directly computed. For instance, in Table 19 it was shown that the P_E for at least slight structural damage was 33% and therefore the P_{DS} for "no damage" would equal 66% (66% chance of having zero structural damage in the structure). Similarly, the P_E for moderate structural damage was 23.5%, which rendered a 10% P_{DS} for the slight structural damage state, 10% chance of having slight structural damage (33% at least Slight (including Moderate and greater) - 23.5% at least Moderate = 10% probability of Slight damage).

An identical process was followed for all STR, NS_{DS}, and NS_{AS} damage states [None, Slight (S), Moderate (M), and Complete (C)]. Then all P_{DS} values were multiplied by the appropriate repair cost ratios (from Table 15, Table 16, and Table 17) to obtain building repair costs as a percentage of the total building replacement cost. For the contents damage assessment, the process is slightly shorter because the previously calculated P_{DS} values for of the nonstructural acceleration-sensitive components (NS_{AS}) are multiplied by the content damage ratios (Table 18) to produce the content repair costs.

Once all the repair costs have been estimated for individual components and damage states, the costs are summed to produce a total estimated repair cost (loss). For this particular example (Table 19), the HAZUS methodology indicated that repair costs for a commercial office building, which sustained a 0.49 in (12.5 mm) peak displacement and 0.4185 g (4.1 m/s^2) peak acceleration, would cost, on average, approximately 24.9% of the total building replacement cost. Here, it can also be seen that most of the damage came from nonstructural acceleration-sensitive and building contents losses.

Analogous direct economic capital-related loss estimates were conducted for hundreds of structural hyperelastic structural configurations as well as their hysteretic counterparts. The structural damage was considered negligible for all hyperelastic models because of the intended lack of inelastic deformations in the lateral load resisting system.

Table 19. Example of Direct Physical Building Damage Computation using HAZUS-MH, inputs' units Sd=[in] and Sa=[g]

		Sd bar	beta	*Sd / Sd bar*	log (*)	log (*) / beta	PE	P DS	COM4	Loss	Sum Loss
STR	Sd 0.49							None 0.66	0	0.00	
	Slight 0.49	1.08	0.81	0.454	-0.343	-0.424	0.336	S 0.10	0.4	0.04	1.68
	Moderate 0.49	2.16	0.89	0.227	-0.644	-0.724	0.235	M 0.12	1.9	0.22	
	Extensive 0.49	6.48	0.94	0.076	-1.121	-1.193	0.116	E 0.09	9.6	0.82	
	Complete 0.49	17.28	0.83	0.028	-1.547	-1.864	0.031	C 0.03	19.2	0.60	
NS DS	Sd 0.49							None 0.61	0	0.00	
	Slight 0.49	0.86	0.84	0.570	-0.244	-0.291	0.386	S 0.11	0.7	0.08	4.02
	Moderate 0.49	1.73	0.9	0.283	-0.548	-0.609	0.271	M 0.13	3.3	0.43	
	Extensive 0.49	5.4	0.97	0.091	-1.042	-1.074	0.141	E 0.07	16.4	1.13	
	Complete 0.49	10.8	0.92	0.045	-1.343	-1.460	0.072	C 0.07	32.9	2.37	
NS AS	Sa 0.4185							None 0.41	0	0.00	
	Slight 0.4185	0.3	0.67	1.395	0.145	0.216	0.585	S 0.18	0.9	0.16	8.81
	Moderate 0.4185	0.6	0.67	0.698	-0.156	-0.234	0.408	M 0.16	4.8	0.77	
	Extensive 0.4185	1.2	0.67	0.349	-0.457	-0.683	0.247	E 0.12	14.4	1.71	
	Complete 0.4185	2.4	0.67	0.174	-0.759	-1.132	0.129	C 0.13	47.9	6.17	
									$\Sigma_{STR+NS-DS+NS-AS}$		14.5

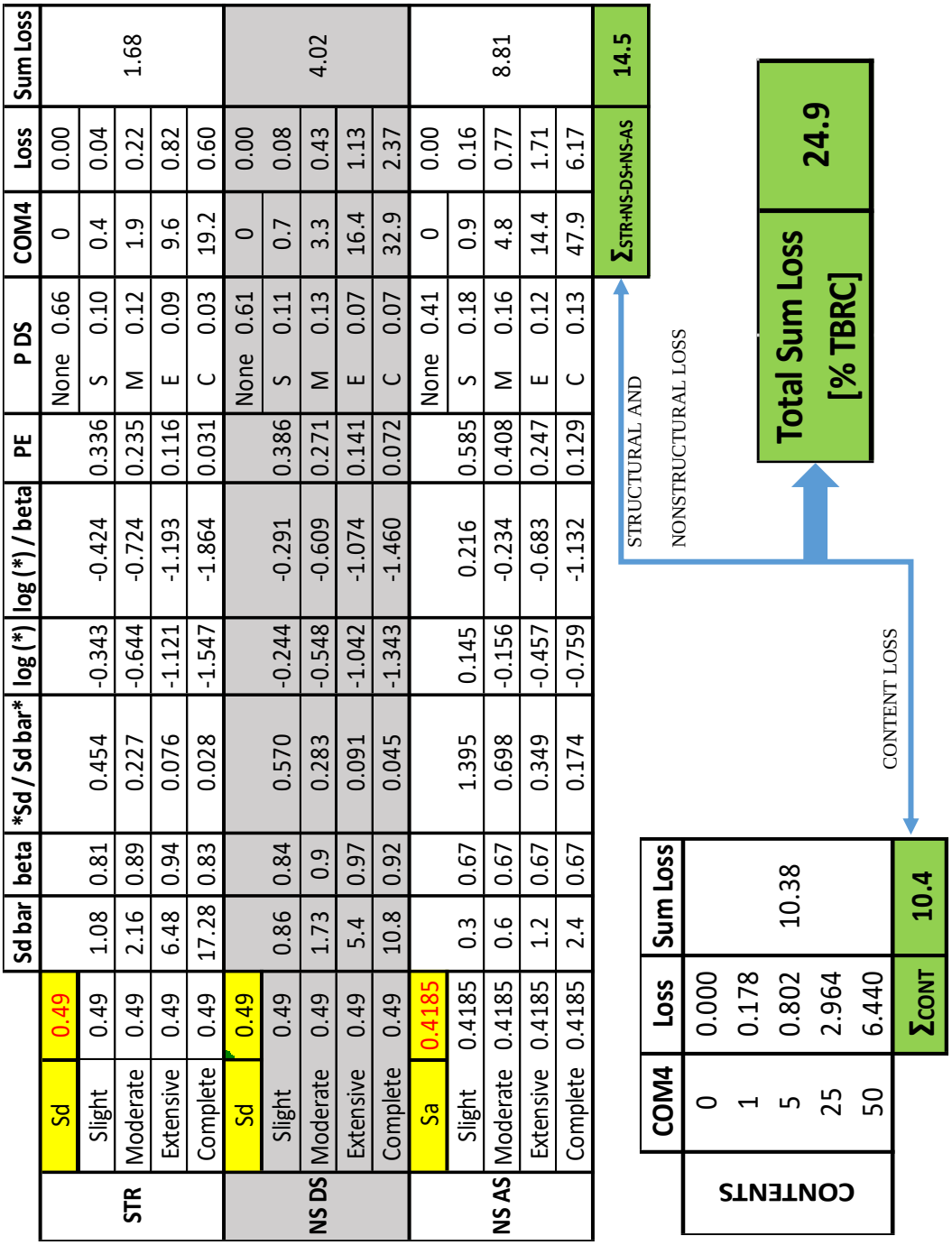

4.6. Parametrization

The performance of two structural models is evaluated in this work: a bilinear elastoplastic (fully hysteretic without degradation) and a trilinear hyperelastic model. The hyperelastic model represents a concentrically-braced frame equipped with innovative hyperelastic fuses. The idealized force-displacement relationships of both systems are shown in Figure 23. The main parameters describing the systems are:

Hysteretic

- **f_y:** Yielding force
- **k_{h0}:** Elastic stiffness and a
- **k_{h2}:** Plastic stiffness.
- **Δ_y:** Yielding displacement

Hyperelastic

- **f_e:** Buckling force
- **k_0:** Initial stiffness
- **k_2:** Buckling stiffness
- **k_3:** Arresting stiffness
- **Δ_g:** Gap closure displacement
- **Δ_e:** Buckling displacement

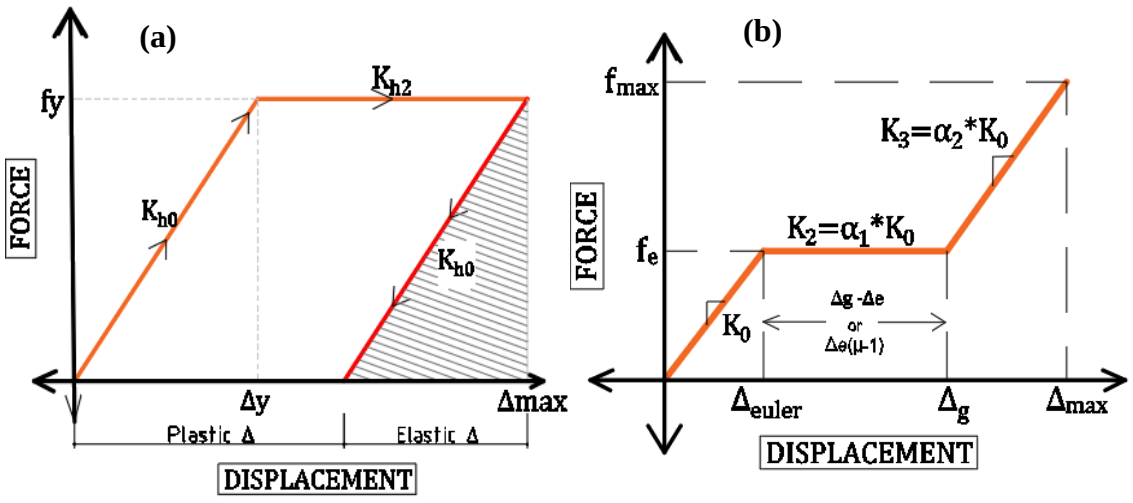

Figure 23. (a) hysteretic system behavior; (b) hyperelastic system.

The initial stiffness was assumed equal (k_{h0}=K_0) for both systems, hyperelastic and hysteretic, through the entire study, and the yielding (k_{h2}) and first post-buckling (K_2) stiffness were assumed zero for simplicity, disregarding potential strain hardening in the hysteretic system or post-buckling strength in the hyperelastic system. Three independent response parameters were selected for parameterization in the hyperelastic model: the ratio of initial to buckling stiffness (α_1), the ratio of initial stiffness to arresting stiffness (α_2), and ductility to the arresting stiffness (μ). Additionally, the hyperelastic buckling force was taken as a fraction of the hysteretic yielding force (f_y), then the force ratio (f_y/f_e) became the fourth parameter evaluated.

$$\mu = \frac{\Delta_g}{\Delta_y};\ \alpha_1 = \frac{k_2}{k_0} = 0;\ \alpha_2 = \frac{k_3}{k_0}$$

4.6.1. Sensitivity Analysis.

In this part of the study, the primary goal was to identify how induvial hyperelastic parameters affect the structural response (peak displacements and mechanical force). First, using a single ground motion response, peak response trends were identified. These trends were confirmed by running all ground motions. If such a trend was valid for more than nine of the sixteen motions, this trend was studied in more detail.

An example of this procedure is presented in Figure 24, where the influence of the arresting stiffness ($k3 = \alpha_2 * k0$) in the final response was investigated. For this purpose, the arresting stiffness ratio (α_2) was varied from 0 (flat) up to 0.25 (K_3 equals 25% of the initial stiffness), while the ductility equals 1.5 and a buckling force is equivalent to half

the yielding force (f_y/f_e=2) of the reference hysteretic model (see Figure 24a). The response pattern here suggested that increasing the arresting stiffness yields a linear decrease in displacement and a linear increase in maximum force. In order to see if this trend remained while changing the ductility, maximum response trend lines (MRTLs) were created. One of these lines is shown in Figure 24b. This line was created by joining the maximum displacement and force (Δ_{max}, f_{max}) of every hyperelastic system in Figure 24a (steps 1 and 2). Once the line was generated, the MRTL was mirrored to the opposite region (step 3) to compare maximum displacements against the hysteretic system at both zones (blue lines in Figure 24c). Finally, Figure 24c shows several MRTLs plotted for ductilities varying from 1.5 to 10 in 0.5 increments. Base on this figure, it was demonstrated that the linear trend remained independent of the ductility used. Similar sensitivity analyses were conducted for all three parameters evaluated (α_2, μ, f_y/f_e ratio). Once a trend was identified, the validity of the trend was verified. A trend was considered valid if it was observed with at least nine of the sixteen considered ground motion records.

In summary, this study identified the parameters governing the seismic behavior of concentrically-braced frames equipped with hyperelastic structural fuses. Additionally, it was analytically verified that it is possible to calibrate hyperelastic fuses to achieve better or comparable performances (regarding peak mechanical force and displacements) to that of comparable hysteretic systems.

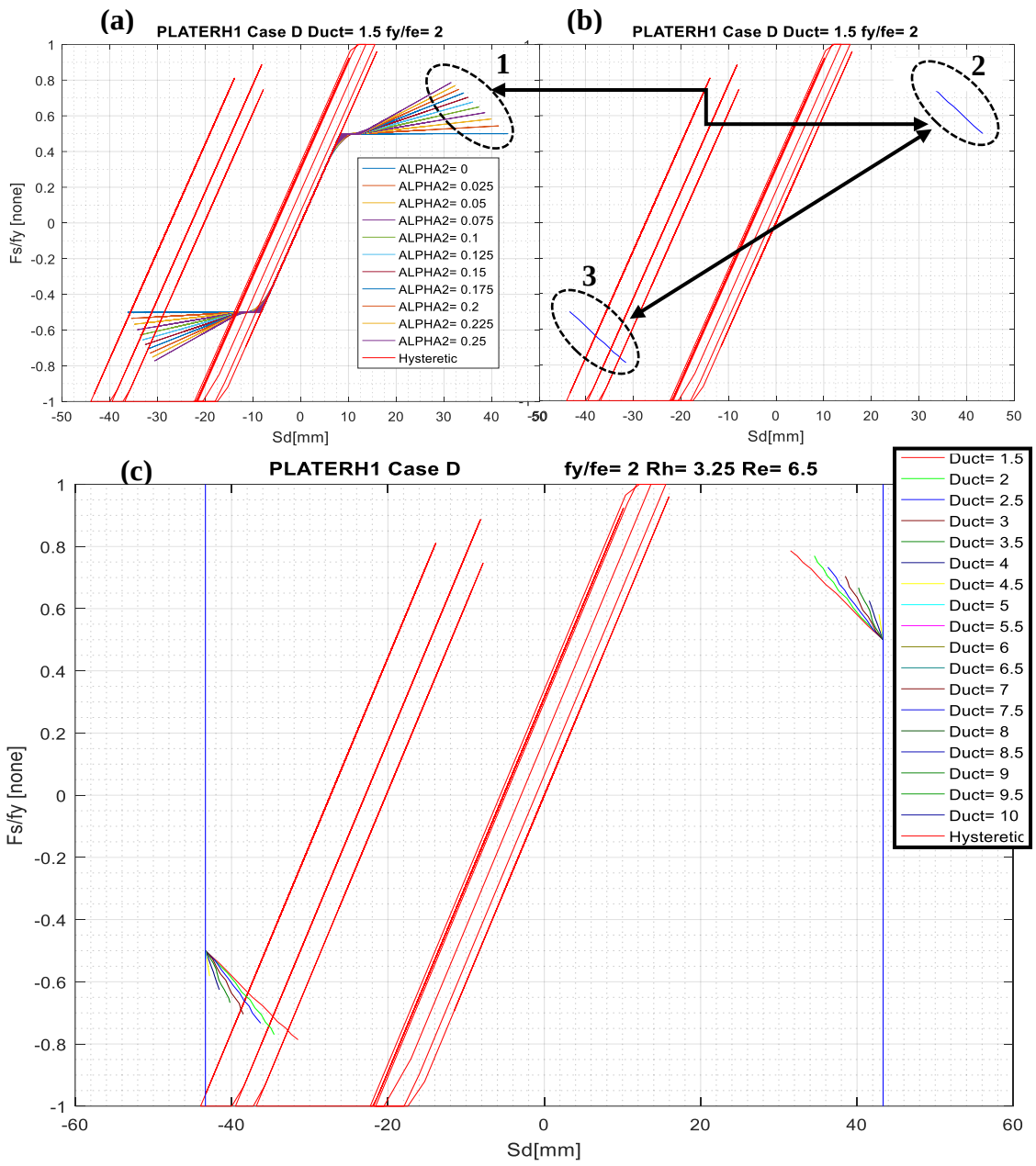

Figure 24. Trend identification example by using maximum response trend lines (MRTLs)

CHAPTER 5. RESULTS

5.1. Overview

The body of this chapter is divided between bilinear and trilinear hyperelastic system evaluations. Within these two sections, the results for each prototype building are discussed one by one (case D through case A). Comparative results for bilinear hyperelastic systems are shown starting on page 55, and the trilinear system results are discussed starting on page 63. Comprehensive summaries of observations are shown for the main findings of the bilinear system evaluations as a whole and individually for each trilinear system.

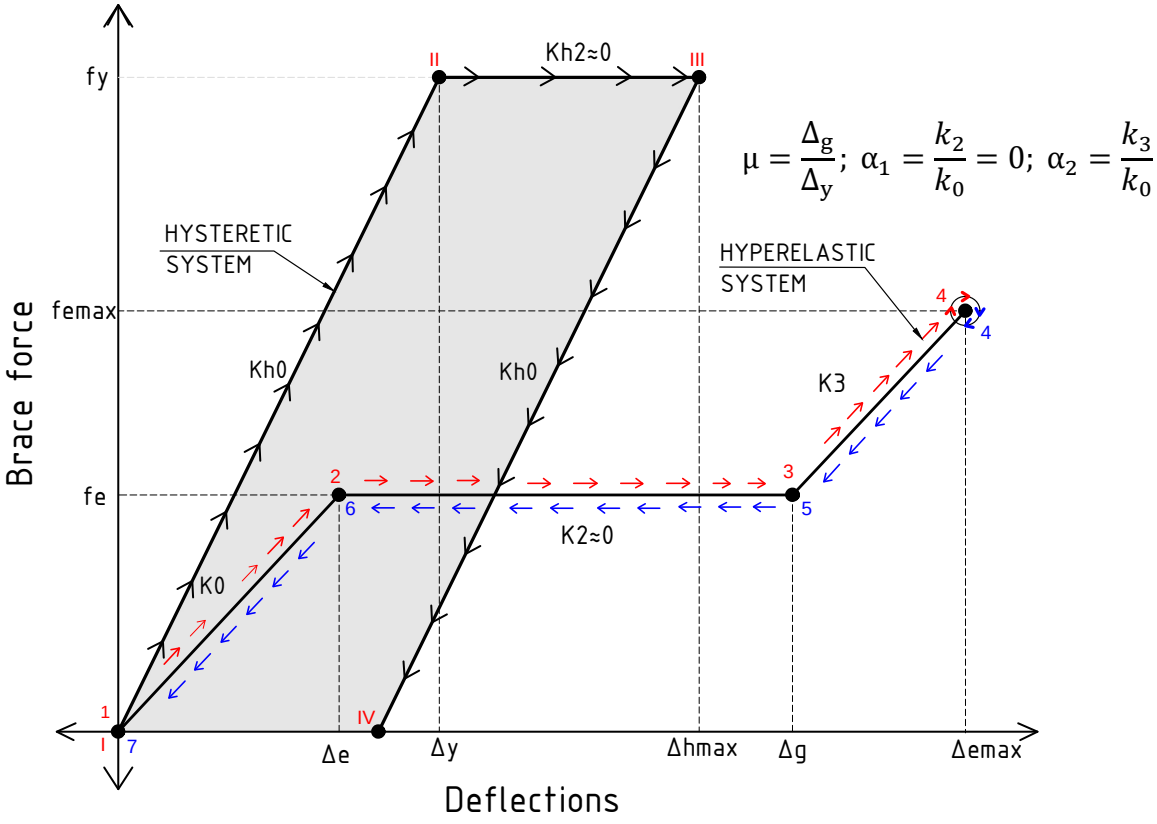

Figure 25. Idealized Force- Displacement curve. Hysteretic and Hyperelastic

5.2. Evaluation of Bilinear Hyperelastic Models

This section explores the possibility of obtaining competitive self-centering features from bilinear hyperelastic systems by trading off reductions in brace force and, ideally, acceleration demands, in exchange for higher average peak displacements. Such bilinear behavior is achieved by using a fuse with enough gap space so that the arresting stiffness (K_3) is never reached.

The main question to address is how much additional displacement will occur for a bilinear hyperelastic system relative to a full hysteretic system? Figure 26 illustrates this comparison, where a hysteretic reference system is plotted against possible bilinear hyperelastic models. Although the hyperelastic (K_0) and hysteretic (K_{h0}) initial stiffnesses are portrayed as having different values (different elastic stiffness slopes), the numerical values were equivalent ($K_{h0} = K_0$) for each of the four considered Cases (A through D).

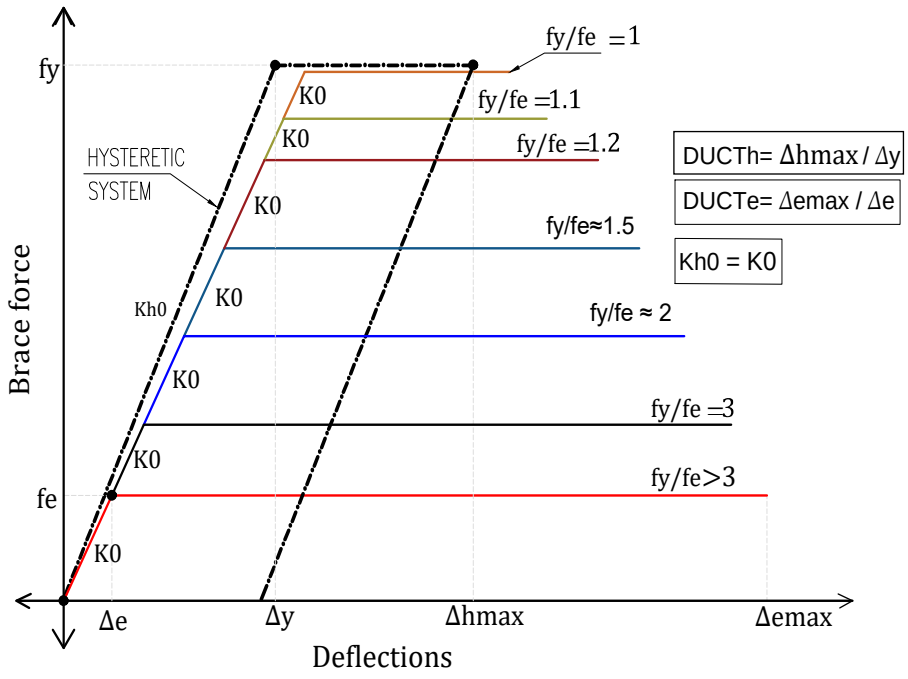

Figure 26. Force-Displacement curve for bilinear hyperelastic systems.

5.2.1. Bilinear, 3-Story Building, Low-Ductility (CASE D)

As described in the Methodology chapter, case D refers to a building with a natural period (Tn) of 0.31s. This period approximates a three story concentrically-braced frame (CBF) building, such as the structure shown in figure 2. According to ASCE/SEI 2010, a response modification factor (R) of 3.25 can be used for seismic design when the frame is proportioned and detailed in accordance with Ordinary CBF requirements.

Analysis results are presented in Table 20 and Figure 27, showing that the peak displacement increased from 44% when fy/fe=1 to 1039% when the buckling force level of the hyperelastic system was reduced to a third of the corresponding hysterestic system yield strength, fy/fe=3. The viability of increasing the fy/fe ratio was explored further while computing loss assessment estimates, results of which are presented in Figure 31.

Table 20. CASE D. Peak Ductility comparisons between Hysteretic and Bilinear Hyperelastic systems (different f_y/f_e ratios.)

CASE D- Ductility							
3-Story, Ordinary Seismic Design							
3 Stories			R=3.25			Tn=0.31	
Ground Motions	**Duct_Hysteretic**	**Duct_Hyperelastic -- (f_y/f_e)**					
	0	**1**	**1.1**	**1.2**	**1.5**	**2**	**3**
CENTRO H1	4	7.43	9	10	22	44	51
CENTRO H2	4.16	5	8	8	13	23	78
PLASTERH1	6.8	9	9	13	16	28	33
PLASTERH2	5.4	5.7	8	8	8	18	39
BraH1	3.6	3.15	4	5	11	18	28
BraH2	2.3	1.55	3	3	6	7	13
MulholH1	2.93	2.67	7	9	59	85	127
MulholH2	2	5.5	8	9	11	16	47
GlandaleH2	1.4	1.79	2	3	3	7	8
GlandaleH1	1.45	2.5	3	4	5	6	8
CanogaH2	5.6	11.24	14	15	19	31	45
CanogaH1	5.3	6.64	8	8	15	26	41
CapitolaH2	6.8	9.1	14	15	17	18	28
CapitolaH1	4.6	4.8	5	5	17	23	42
FurtuneH2	4	8.64	9	13	20	26	69
FurtuneH1	6.8	12	8	15	18	23	108
Average	**4.2**	**6.0**	**7.4**	**8.9**	**16.3**	**24.9**	**47.8**
Max	**6.8**	**12**	**14**	**15**	**59**	**85**	**127**

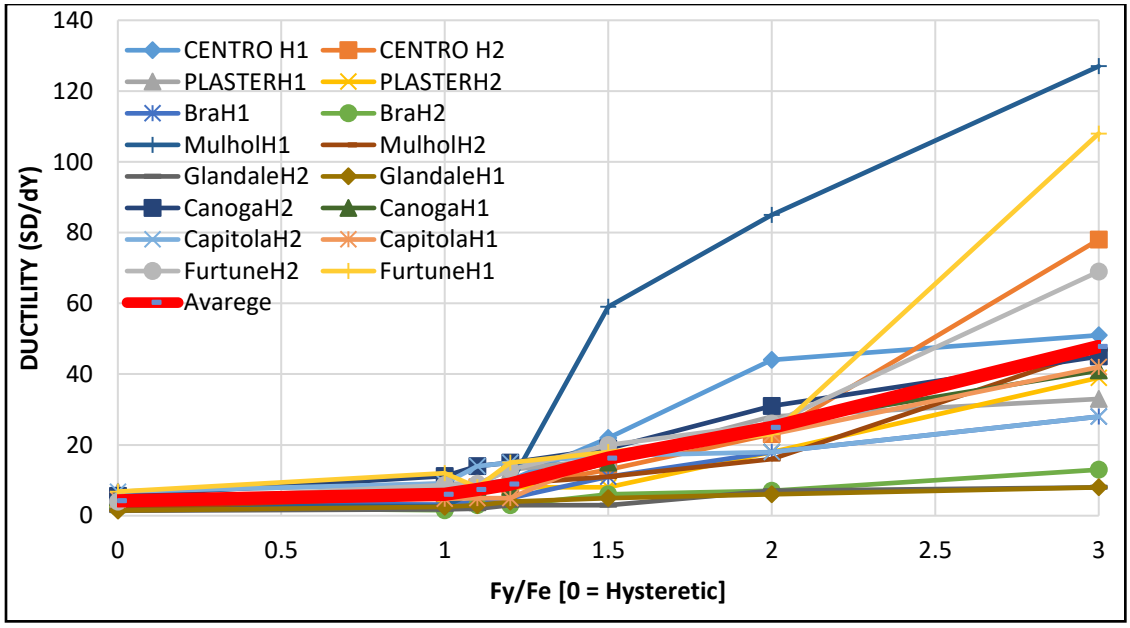

Figure 27. CASE D. Ductility required for a Bilinear Hysteretic system, different fy/fe ratios.

5.2.2. Bilinear, 1-story Building, Low-Ductility (CASE C)

As described in the methods chapter, case C refers to a building with a natural period of 0.17 seconds. As with case D discussed previously, the R factor equals 3.25.

Table 21 and Figure 28 show the results for this particular building. Here, the increase in displacement demands was more pronounced with a shorter period (higher elastic stiffness). When f_y equals f_e, the average ductility for the hyperelastic system was 12 (116% increase over the hysteretic) while for $f_e=f_y/3$ the average ductility reached 94 (1593% increase over the hysteretic). Hence, the viability of increasing f_y/f_e was further explored through HAZUS-MH. Those results are presented in Figure 31.

Table 21. CASE C. Peak Ductility comparisons between Hysteretic and Bilinear Hyperelastic systems (different f_y/f_e ratios.)

CASE C- Ductility							
1-Story, Ordinary Seismic Design							
1 Stories			R=3.25			Tn=0.17	
Ground Motions	**Duct_Hysteretic**	**Duct_Hyperelastic -- (f_y/f_e)**					
	0	**1**	**1.1**	**1.2**	**1.5**	**2**	**3**
CENTRO H1	7.13	22.2	25	31	45	87	164
CENTRO H2	9.56	10.33	14	17	21	46	126
PLASTERH1	8.12	22.4	21	26	35	46	93
PLASTERH2	9.5	22.95	25	28	26	36	66
BraH1	4	6.76	7	8	19	26	71
BraH2	3.6	2.4	2	3	3	20	30
MulholH1	3.58	4.3	7	9	59	85	127
MulholH2	2.13	5.74	7	21	27	42	81
GlandaleH2	3	7.4	7	9	10	18	26
GlandaleH1	2.65	7.6	8	8	10	15	20
CanogaH2	6.5	26	28	32	51	65	96
CanogaH1	7.1	11.68	13	13	25	46	109
CapitolaH2	9.8	15.77	10	42	42	48	72
CapitolaH1	5.79	13.6	14	14	17	46	73
FurtuneH2	2.72	6.2	13	8	32	57	163
FurtuneH1	3.67	7	35	34	55	56	187
Average	**5.6**	**12.0**	**14.8**	**18.9**	**29.8**	**46.2**	**94.0**
Max	**9.8**	**26**	**35**	**42**	**59**	**87**	**187**

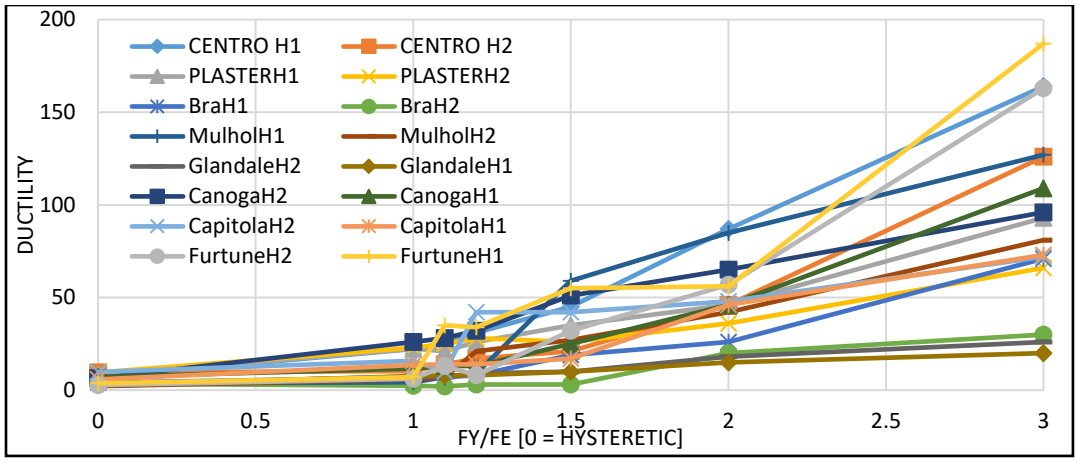

Figure 28. CASE C. Ductility required for a Bilinear Hysteretic system, different f_y/f_e ratios.

5.2.3. Bilinear, 3-story Building, High Ductility (CASE B)

As described in the methods chapter, case B refers to a 3-story building with a natural period of 0.4 seconds. Case B represents a building designed for high seismic demands. Therefore, the response modification factor (R) equals 6, corresponding to a structure meeting requirements for Special CBFs (ASCE/SEI 2010). Table 22 and Figure 29 show the results for this particular building. When the same force capacity is used for hyperelastic and hysteretic systems (f_y/f_e=1), the average peak ductility required increases 60%, a ductility of 8.5 in the hysteretic versus a 13.6 of the hyperelastic. If the buckling force in the hyperelastic (f_e) is set to one-third of the hysteretic system yield strength (f_y/f_e =3), the average ductility demand is 671% greater than that of the hysteretic system. The economic viability of increasing the f_y/f_e was further explored through HAZUS-MH. The results are presented in Figure 31.

Table 22. CASE B. Peak Ductility comparisons between Hysteretic and Bilinear Hyperelastic systems (different f_y/f_e ratios.)

CASE B - Ductilities							
3-Story, design for seismic							
	3 Stories		R=6			Tn=0.4	
Ground Motions	Duct_Hysteretic	Duct_Hyperelastic -- (f_y/f_e)					
	0	1	1.1	1.2	1.5	2	3
CENTRO H1	15	20.2	28	31	40	43	92
CENTRO H2	9.2	13	19	20	52	89	118
PLASTERH1	6.5	18	18	19	24	47	59
PLASTERH2	9.7	8.5	17	19	25	39	70
BraH1	8.6	10	11	13	16	22	32
BraH2	5.12	4.8	4	4	20	34	43
MulholH1	9.24	23	25	27	36	41	57
MulholH2	5.58	15.6	19	20	29	37	47
GlandaleH2	4	4	4	5	5	7	9
GlandaleH1	2.65	3.37	4	4	5	6	7
CanogaH2	10.35	20.3	20	25	34	55	93
CanogaH1	6.18	16.7	19	20	22	34	54
CapitolaH2	11.43	12.2	13	14	16	26	43
CapitolaH1	9.22	10	18	22	27	35	42
FurtuneH2	7.17	20.5	29	32	36	96	149
FurtuneH1	16.7	18	29	44	66	84	138
Average	**8.5**	**13.6**	**17.3**	**19.9**	**28.3**	**43.4**	**65.8**
Max	**16.7**	**23**	**29**	**44**	**66**	**96**	**149**

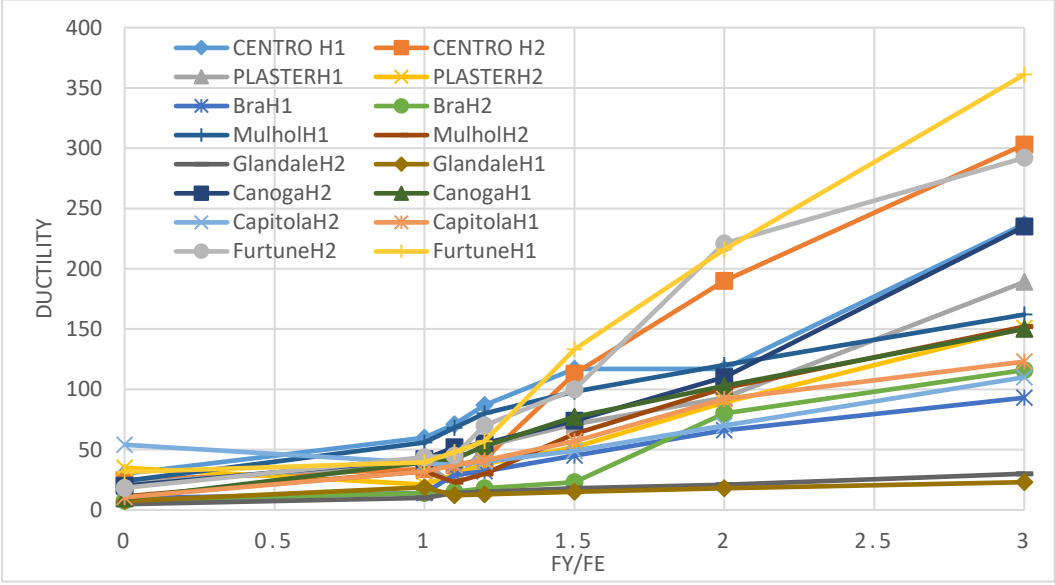

Figure 29. CASE B. Ductility required for a Bilinear Hysteretic system, different f_y/f_e ratios.

5.2.4. Bilinear, 1-Story Building, High Ductility (Case A).

Case A refers to a low-rise steel concentrically-braced frame designed with high seismic standards. ASCE 7-10 assigns a response modification factor of 6 to buildings designed and detailed with Special CBFs.

Table 23 and Figure 30 show the results for this building. When f_y equals f_e, peak ductility demands increase by 67% relative to the baseline hysteretic case. When f_y/f_e=3, a 752% increase in peak displacement demand (relative to the hysteretic) is observed for the selected ground motions. The viability of this system is further explored by using HAZUS-MH. Results are presented in Figure 31.

Table 23. CASE A. Peak Ductility comparisons between Hysteretic and Bilinear Hyperelastic systems (different f_y/f_e ratios.)

CASE A - Ductilities							
low-rise, Design for seismic							
1 Stories			**R=6**			**Tn=0.2**	
Ground Motions	**Duct_Hysteretic**	**Duct_Hyperelastic -- (f_y/f_e)**					
	0	**1**	**1.1**	**1.2**	**1.5**	**2**	**3**
CENTRO H1	30	60	71	87	117	117	237
CENTRO H2	24.9	34	37	42	113	190	303
PLASTERH1	22	39	21	53	71	93	189
PLASTERH2	35	21	29	38	52	89	151
BraH1	9.7	14	29	32	45	66	93
BraH2	7.48	14	15	18	23	80	116
MulholH1	24	56	68	80	98	120	162
MulholH2	11.2	32	23	30	63	101	152
GlandaleH2	4.74	10	14	15	18	21	30
GlandaleH1	7.3	18.85	12	13	15	18	23
CanogaH2	20	42	52	55	74	110	235
CanogaH1	9.42	39.33	42	53	77	103	150
CapitolaH2	54	39	37	40	49	70	110
CapitolaH1	10.4	32	37	41	57	92	123
FurtuneH2	18.3	43.6	45	70	100	221	292
FurtuneH1	31.5	39.5	48	57	133	216	361
Average	**20.0**	**33.4**	**36.3**	**45.3**	**69.1**	**106.7**	**170.4**
Max	**54**	**60**	**71**	**87**	**133**	**221**	**361**

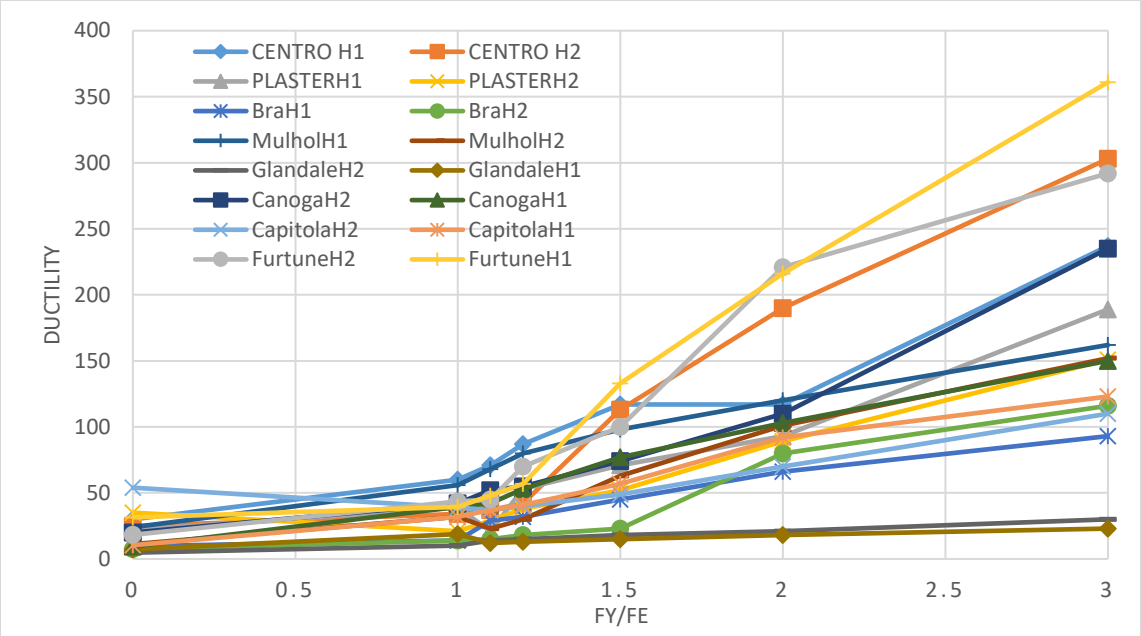

Figure 30. CASE A. Ductility required for a Bilinear Hysteretic system, different f_y/f_e ratios.

5.2.5. Summary and Loss Assessment Estimates for Bilinear Hyperelastic Models.

Figure 31 shows the direct economic loss estimates for bilinear hyperelastic systems at each prototype building discussed above (cases A, B, C, and D). In Figure 31, the normalized cost of hyperelastic system loss to hysteretic system loss ($Cost_{\_Hyper}/Cost_{\_Hysteretic}$) is plotted versus several f_y/f_e and different ductility levels. A value of 1 in the vertical axes means same repair cost for both systems while higher values than one mean that the hyperelastic repair cost exceeded that of the hysteretic.

These results show that none bilinear hyperelastic systems are expected to increase the direct economic impact of an earthquake. Accelerations only correlate directly to forces for linear systems, so the considered scenarios with reduced system forces did not produce proportionately reduced accelerations.

Favorable relative repair costs will depend on whether or not the nonstructural damage due to additional displacements offset the savings of preventing structural damage and reduced accelerations. The buildings with a higher period (case B and D) showed direct repair costs closer to the hysteretic, suggesting that for more flexible structures with reduced elastic stiffness, a bilinear hyperelastic system could yield better performance.

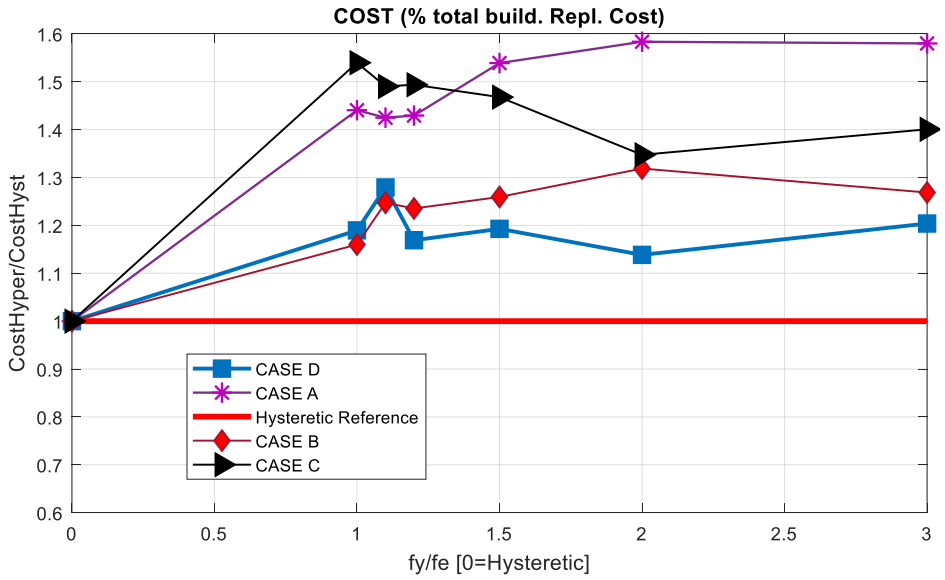

Figure 31. Loss assessment estimate for Bilinear Hyperelastic models.

5.3. Trilinear Hyperelastic Evaluations

Figure 32 shows different hyperelastic configurations contrasted against a conventional hysteretic model. An infinite array of hyperelastic system permutations could be considered. However, during the analysis, the pool of systems was significantly reduced by considering only parametric combinations that result in equal or reduced force compared to the hysteretic system ($f_{e,\,max}<f_y$). This requirement limited the valid range of arresting stiffness (K_3) considerably. As had been implemented for the bilinear

hyperelastic study, the same initial stiffness was used for both reference hysteretic and hyperelastic systems.

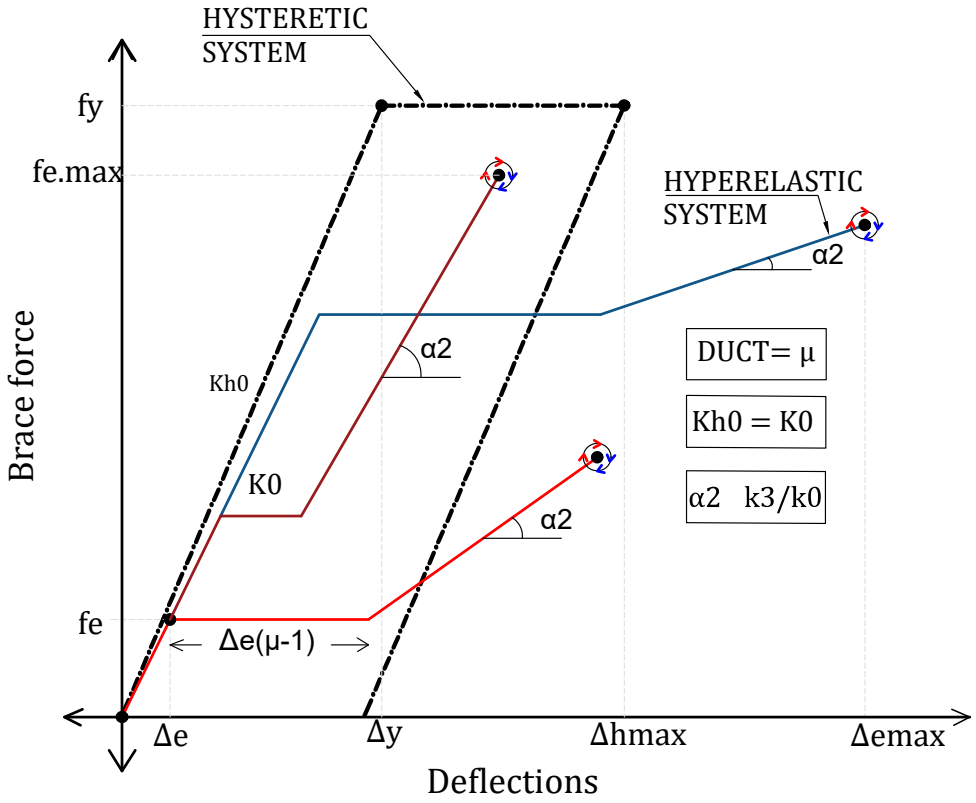

Figure 32. Different Hyperelastic configurations (Force-Displacement)

During the analysis, it was noticed that the hyperelastic peak brace forces were highly influenced by variations in frequency content of each motion, especially low-frequency content. For instance, when motions that exhibit higher acceleration demands (compared to those of the target spectrum) in the long period range were used, the hyperelastic system required stricter parameter combinations to meet the mechanical force level (i.e. FortuneH1, FortuneH2). On the other hand, when motions with lower acceleration demands in the long period range (Tn>0.7s) were used, the hyperelastic system met the hysteretic force level within a wider pool of parameters.

Trends were identified from an extensive parametric study, with main findings presented below in a case by case format.

5.3.1. Trilinear, 3-Story Building, Low-Ductility (CASE D)

The analyses revealed that the arresting stiffness (K_3) must be kept less than $0.1K_0$ to ensure that the hyperelastic maximum brace force will be equal to or less than the complementary hysteretic brace. An example is shown in Figure 33a, where the buckling force in the hyperelastic system is three times less than the yielding force in the hysteretic system ($f_y/f_e = 3$), and the ductility from buckling to the arresting stiffness is 2.5. In this figure, the blue lines demarcate the maximum displacement and force in the reference hysteretic system. When α_2 is set higher than 0.1, all hyperelastic maximum forces surpass the brace force of the reference hysteretic system. This happens to be true for the majority of f_y/f_e ratios, but the lowest peak displacements were obtained with f_y/f_e ratios close to 1.0. Similarly, it was found that ductility (Figure 33b) did not have considerable influence in the force demand when lower f_y/f_e values were used (1 to 2).

Three values of α_2 (0.1, 0.05, and 0.025) were evaluated for ductility values of 7 to 15 and fy/fe ratios from 1 to 6. the optimal combinations of K_3 (α_2) and ductility with respect to peak force and displacement demands were:

- $\alpha_2 = 0.1$, $\mu=9$ to have $f_{e,\,max} < f_y$ for most f_y/f_e
- $\alpha_2 = 0.05$, $\mu>6$ to have $f_{e,\,max} < f_y$ for all f_y/f_e
- $\alpha_2 = 0.025$, any ductility allows that $f_{e,\,max} < f_y$ for all f_y/f_e (but when f_y/f_e equals 1, μ >7 is required)

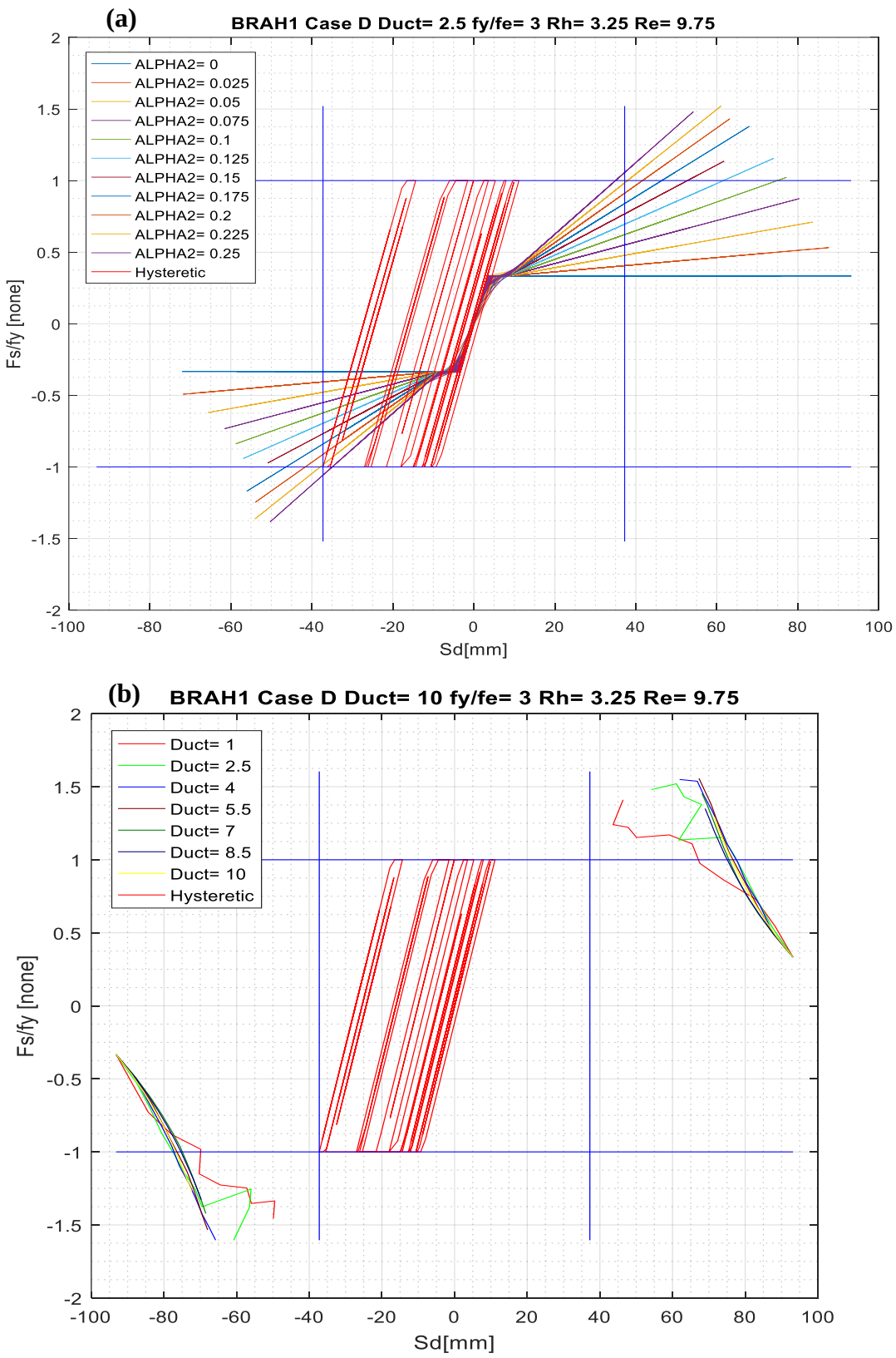

Figure 33. CASE D- f_y/f_e equals 3. (a) Right: α_2= [0 to 0.25] for μ=2.5; (b) Left: μ = [1 to 10] for α_2 [0-0.25].

In summary, for all combinations of μ and the f_y/f_e ratio, the arresting stiffness (K_3) has to be less than 10% of the initial stiffness (K_0). This range of stiffness was used to meet the force limit in the brace. The best displacement responses were found when f_y/f_e was closer to 1.0 (similar force level on both systems), and the highest K_3 considered was used (α_2 close to 0.1).

5.3.1.1. Case D. Loss Assessment Estimates

The structural responses of hyperelastic systems with peak forces not exceeding the comparable hysteretic system force were used to assess seismic consequences with respect to direct building repair costs. Building accelerations and peak displacements were mapped to direct economic loss by using the HAZUS-MH loss assessment methodology.

Three loss estimates are presented, which provide meaningful insights about the advantages of using either system.

- Previously, it was noted that the max brace force developed in hyperelastic systems with α_2= 0.1 and μ=9 generally did not exceed the yielding force of the reference hysteretic system ($f_{e,max}<f_y$ for most f_y/f_e considered). However, when the induced peak accelerations and displacements were mapped to direct economic losses, only the f_y/f_e ratios greater than three (3) yielded considerable savings in final repair costs (20% less than the hysteretic). This reduction is illustrated in Figure 34, where the normalized repair cost (hyperelastic repair cost normalized by corresponding hysteretic repair cost) is plotted against the f_y/f_e ratio for several ductilities. This repair cost was compute based on the average

hyperelastic response obtained after running all ground motions (9 out of 16 was the minimum number of motions needed to add a point in Figure 34).

In this figure, it is also shown that hyperelastic systems with f_y/f_e ratio lower than two (2) exceeded the unity threshold, which means that such configurations would be expected to require higher repair costs than a comparable conventional hysteretic system.

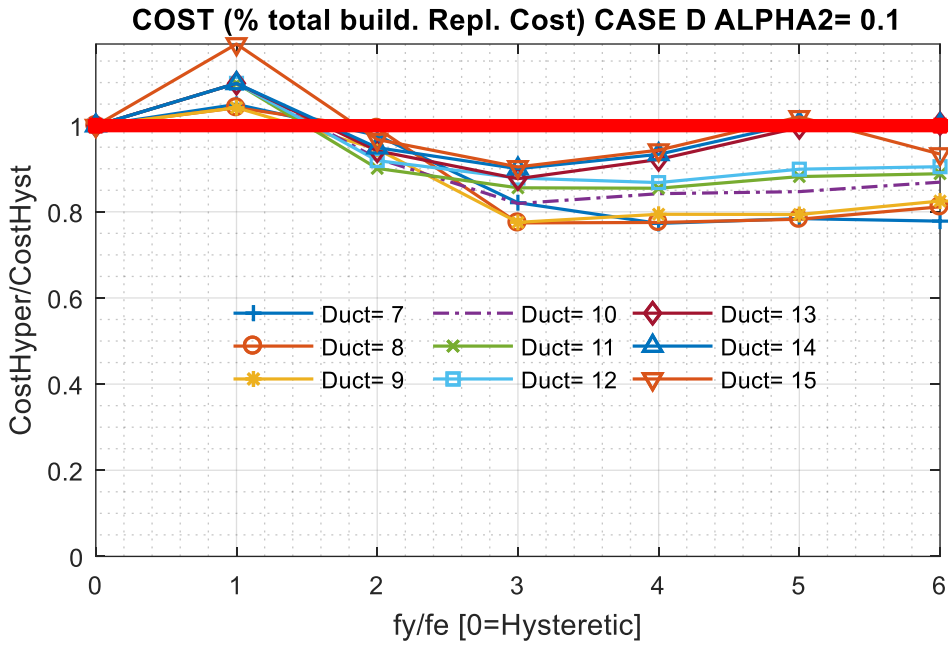

Figure 34. CASE D- α_2=0.1; Normalized repair cost, ductility, and f_y/f_e ratio.

- Similarly, some hyperelastic systems were modeled with an $\alpha_2 = 0.05$ and $\mu>6$. Figure 35 shows that even though such systems met the force level ($f_{e,\,max}<f_y$), the direct economic impact is not likely to be an improvement over hysteretic systems.

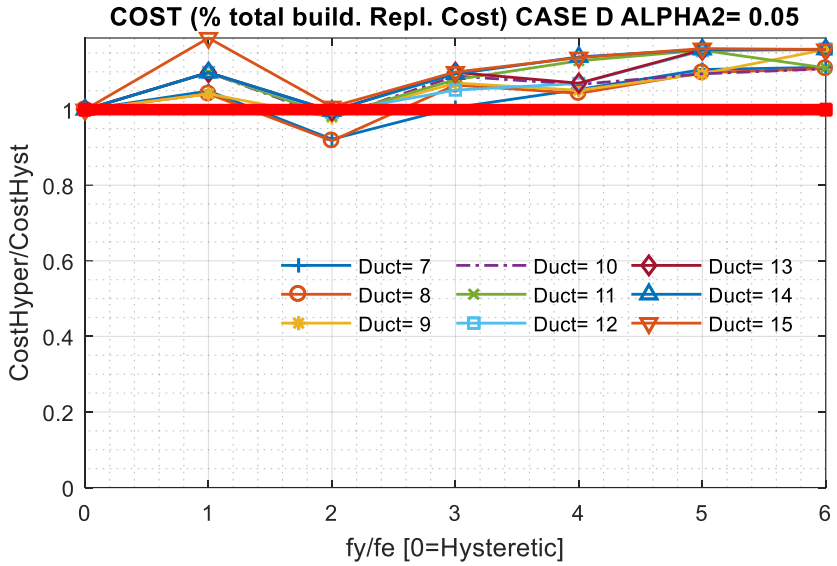

Figure 35. CASE D- α_2=0.05; Normalized repair cost, ductility, and f_y/f_e ratio.

- Third, the loss assessment in Figure 36, showed that no hyperelastic trilinear systems with α_2= 0.025 were competitive with hysteretic systems based solely on direct economic loss estimation.

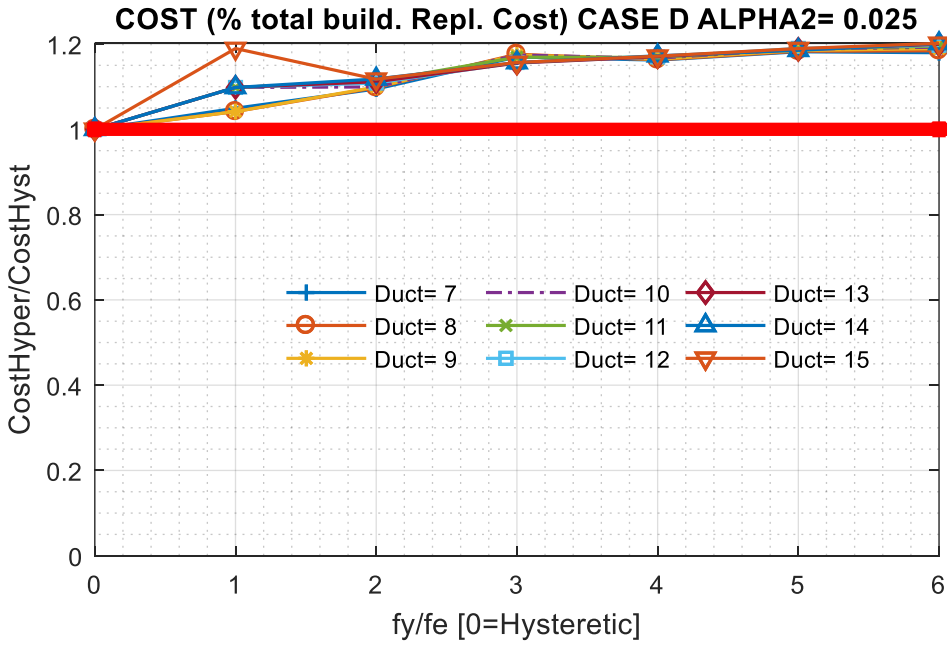

Figure 36. CASE D- α_2=0.025; Normalized repair cost, ductility, and f_y/f_e ratio.

5.3.1.2. Case D. Summary

The best hyperelastic performance was observed when the highest arresting (K_3) stiffness was used (10% of K_0) because this minimized displacement demands while brace forces were maintained similar or lower than the reference hysteretic system. This configuration yielded a repair cost reduction of 20% over a comparable conventional hysteretic system.

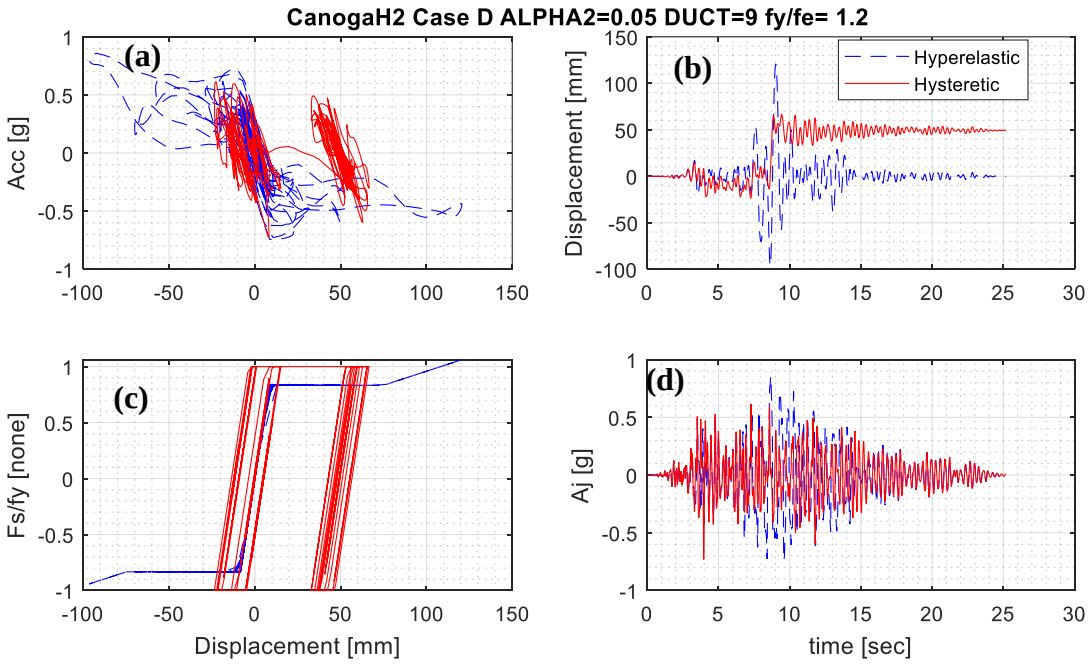

Figure 37. CASE D. (a) Acc. Vs Disp.; (b) Disp. vs. time; (c) normalized brace force vs. Displ.; (d) Acc. vs. time.

To understand the unfavorable performance outcomes when a lower K_3 was used, the data was further examined and confirmed that the additional displacement demands caused by the softened stiffness were not compensated by a significant reduction in

acceleration demands. Having similar damage coming from acceleration-sensitive elements (Figure 37a, Figure 37d) and larger peak displacements (Figure 37b, Figure 37c) resulted in higher repair cost estimates for these hyperelastic systems.

Direct economic losses attributed to displacements (drift-sensitive nonstructural) and accelerations (acceleration-sensitive nonstructural and contents) were aggregated separately for each combination of ductility and fusing force ratio (f_y/f_e). The aggregated displacement- and acceleration-based losses were then normalized by their sum for each combination, providing a relative measure of displacement vs. acceleration demand parameter significance. Figure 38 presents the results of these calculations for Case D at each of α_2 equal to 0.1, 0.05, and 0.025. A f_y/f_e ratio equal to zero (0) corresponds to the reference hysteretic system loss distribution. Filled markers correspond to displacement-induced damage (associated with S_d in HAZUS), and unfilled markers correspond to acceleration-induced damage (associated with S_a in HAZUS). Structural damage was assumed negligible for all hyperelastic models, but was included in the displacement-based damage for the hysteretic system losses.

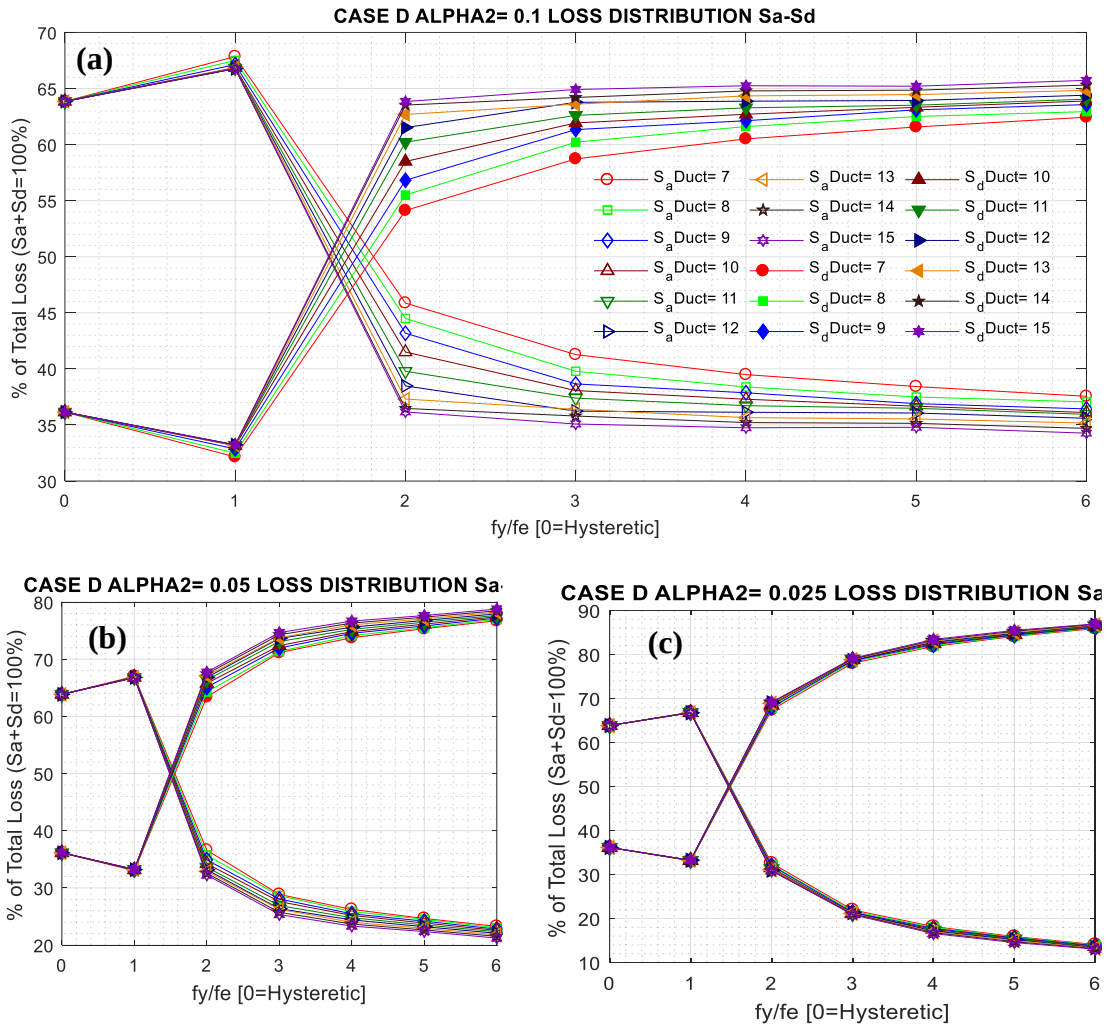

Figure 38. CASE D. (a) loss distribution for α_2=0.1; (b) loss distribution for α_2=0.05; (c) loss distribution for α_2=0.025.

For hyperelastic systems with low f_y/f_e ratios (f_y/f_e approaching 1, when the hyperelastic buckling force approaches the hysteretic yielding force), the damage in the hyperelastic structure was mainly attributable to acceleration-sensitive components (e.g., damaged suspended ceilings and/or mechanical, electrical, or plumbing components in ceiling spaces, or falling shelves and damage to building contents). As the f_y/f_e ratio increased, peak displacements rise correspondingly and become the primary source of damage in the building (at drift-sensitive nonstructural elements such as partitions or curtain walls). The damage distribution for each of the examined K_3 options is shown in

Figure 38a, Figure 38b, and Figure 38c. These figures also show that the role of ductility diminished when systems were modeled with low α_2.

5.3.2. Trilinear, 1-Story Building, Low-Ductility (CASE C)

Similarly, to the Case D building, the same initial stiffness was used for both hysteretic and hyperelastic systems. The Case C building differs from Case D with a shorter natural period (0.17 sec for Case C versus 0.31 sec for Case D). This building presented a greater challenge to find hyperelastic systems that develop less or equal brace force and comparable displacements to those of the comparable hysteretic system. These complications were due to the excellent responses exhibited by the hysteretic model. Testing hundreds of different hyperelastic configurations revealed that:

- Systems with α_2= 0.1 did not meet the force limit $f_{e,\,max}<f_y$ until high ductilities were used ($\mu>45$). However, when the f_y/f_e ratio was kept below three (f_y/f_e <3), ductility values as low as thirty ($\mu>30$) could satisf$_y$ the peak force limit.
- Hyperelastic systems with α_2= 0.05 required ductilities larger than twenty ($\mu>20$) to have $f_{e,\,max}<f_y$ for all f_y/f_e ratios less than three (3); the rest of the f_y/f_e combinations would require $\mu>35$ to satisf$_y$ the peak force limit.
- When α_2= 0.025 or lower, ductilities higher than five ($\mu>5$) are enough to guarantee that the $f_{e,\,max}$ is less than f_y. This applies to all f_y/f_e ratios.

5.3.2.1. Case C. Loss Assessment Estimates

HAZUS-MH estimates provided meaningful insights about the magnitudes of direct economic loss when using hysteretic versus hyperelastic systems.

- The analysis of hyperelastic systems with α_2= 0.1, see Figure 39, shows that the vast majority of hyperelastic models rendered higher repair costs than the traditional hysteretic.

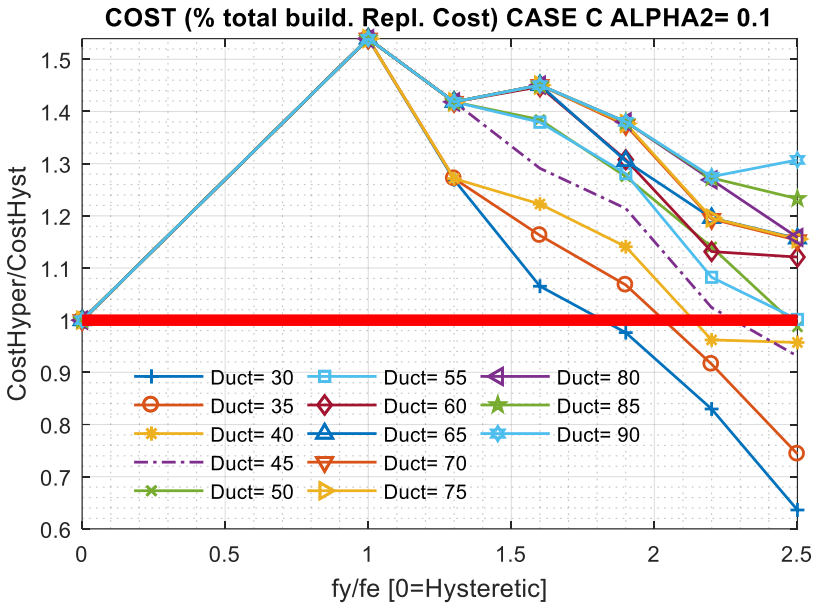

Figure 39. CASE C- α_2=0.1; Normalized repair cost, ductility, and f_y/f_e ratio.

- Hyperelastic systems with a α_2 = 0.05 and μ>20 were evaluated. Figure 40 shows that systems with a f_y/f_e ratio higher than 3 produce an estimated 10% direct repair saving over the hysteretic model.

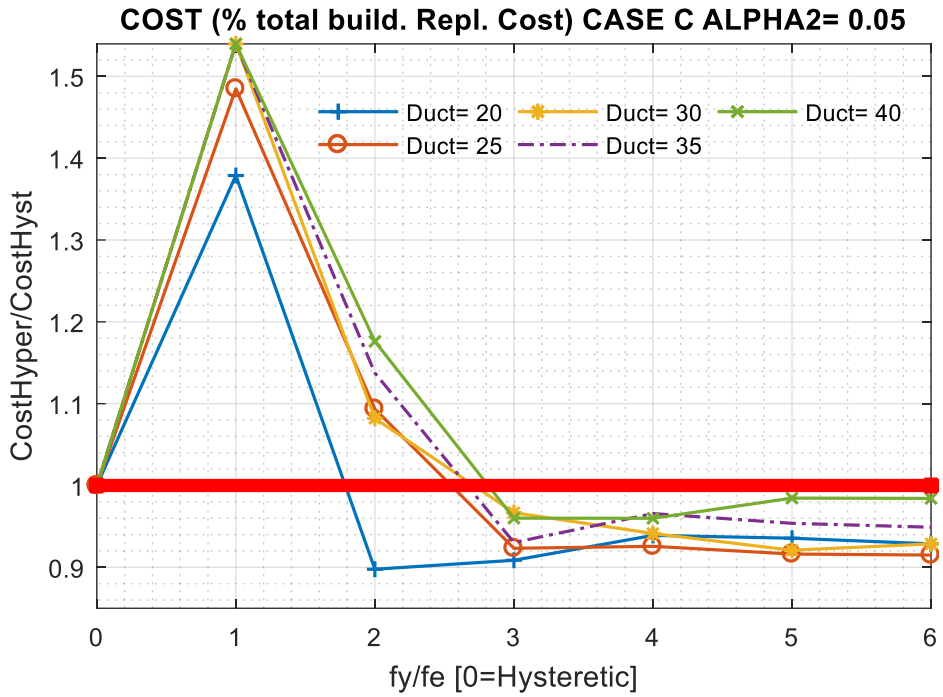

Figure 40. CASE C- α_2=0.05; Normalized repair cost, ductility, and f_y/f_e ratio.

- The loss assessment results presented in Figure 41, using α_2= 0.025, showed that increasing the flexibility generated higher total losses, while the f_y/f_e ratio did not display substantial influence in either reducing or increasing direct economic loss outcomes. In general, none of the hyperelastic systems considered were competitive (regarding direct economic damage only) with traditional hysteretic systems.

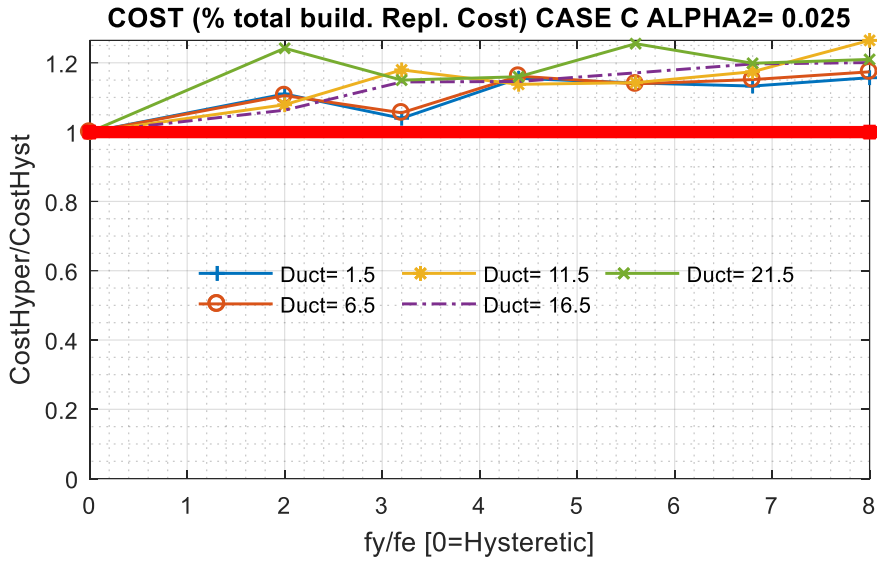

Figure 41. CASE C- α_2=0.025; Normalized repair cost, ductility, and f_y/f_e ratio.

5.3.2.2. Case C. Summary

The most favorable hyperelastic performance relative to hysteretic performance was observed when the arresting stiffness was set to 0.05 (5% of K_0), providing a reduction in direct economic loss of 10% over the conventional hysteretic. The rest of the arresting stiffness, ductility and fy/fe variations considered did not result in expected direct economic loss savings.

These adverse outcomes were further examined to find the cause of the overruns. Figure 42 shows a representative comparison of hysteretic and hyperelastic system responses for Case C, for one ground motion. The hyperelastic system behaved correctly, but the reason why it was not competitive (regarding direct economic repair cost) was due to the excellent hysteretic response that eclipsed it. The residual displacements incurred by the hysteretic system and avoided in the hyperelastic system (structural damage savings) were not significant enough to offset the damage caused by large

relative displacements (damage to nonstructural drift-sensitive elements) that result in higher earthquake direct capital-related costs.

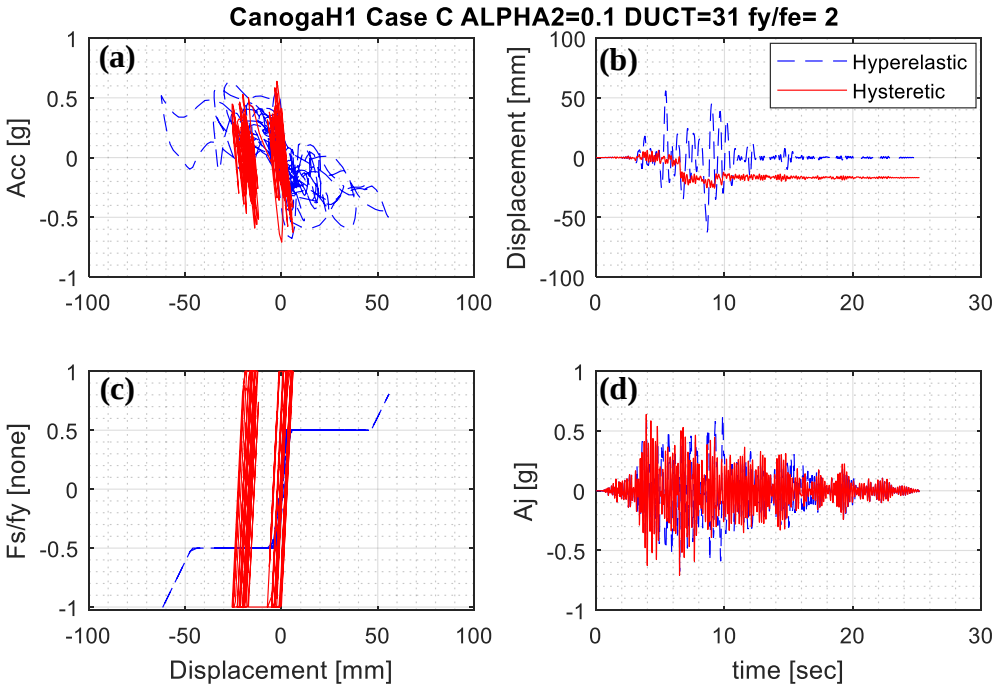

Figure 42. CASE C. (a) Acc. Vs Disp.; (b) Disp. vs. time; (c) normalized brace force vs. Displ.; (d) Acc. vs. time.

Furthermore, the loss assessment distribution illustrated below (see Figure 43a) showed that when K_3 equals 10% of K_0, displacement-induced and acceleration-induced losses are approximately evenly distributed for most of the evaluated hyperelastic models (those meeting the hysteretic mechanical force threshold). A similar loss distribution was observed in hyperelastic systems when K_3 was 5% of K_0 (see Figure 43b), but a wider pool of systems passed the force limit. Optimal combinations of fusing force ratio and ductility produced hyperelastic systems expected to incur approximately 5% to 10% less direct economic loss than a comparable hysteretic system.

Systems with a shallower arresting stiffness (K_3 less than 2.5% of K_0) did not provide economic savings in terms of mainshock direct economic effects. The loss distribution (see Figure 43c) showed that most of the building damage was due to large displacements causing the loss of nonstructural drift-sensitive elements.

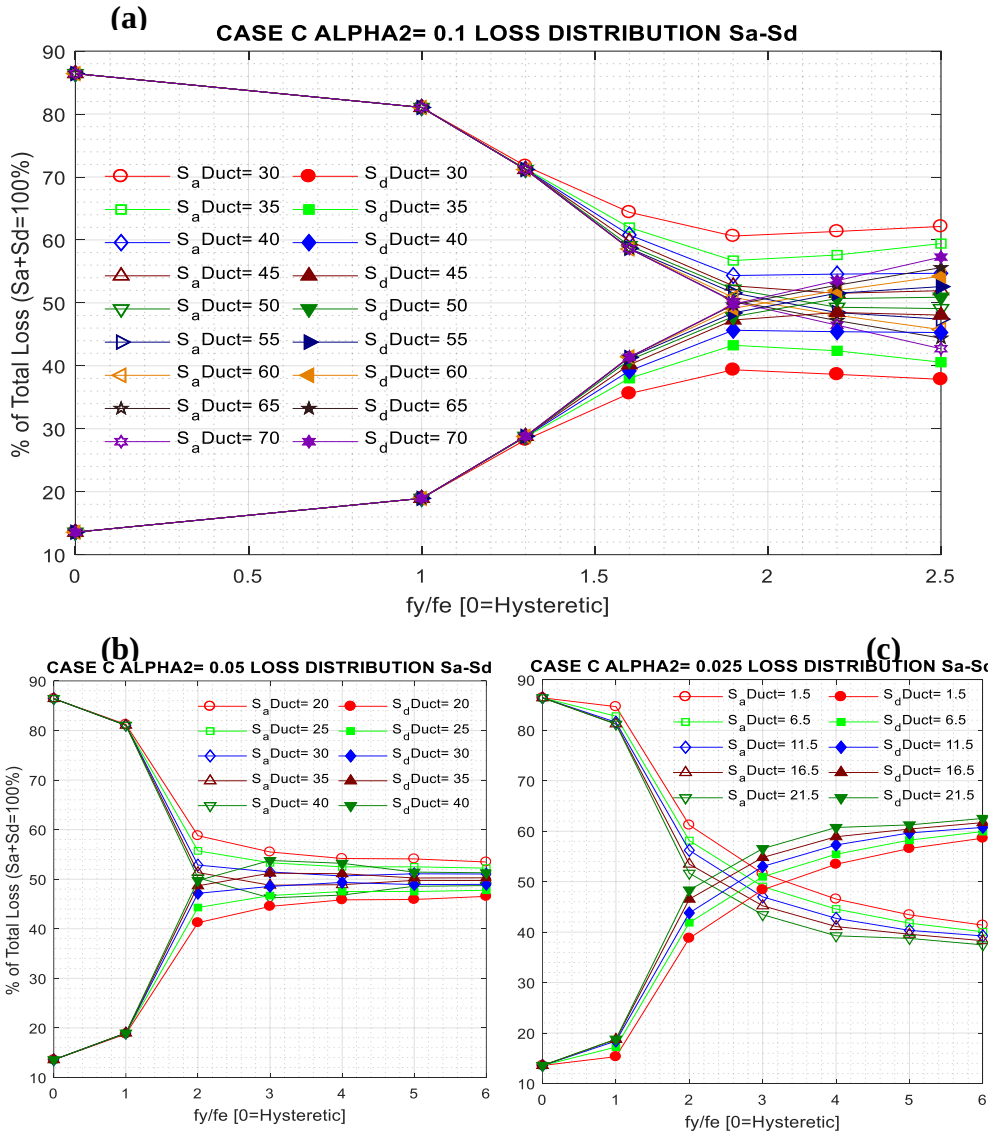

Figure 43. CASE C. (a) Loss distribution for α_2=0.1; (b) loss distribution for α_2=0.05; (c) loss distribution for α_2=0.025.

In summary, lowering the arresting stiffness (α_2) diminishes the influence of ductility in the response. The transition to re-stiffening would not generate significant response

variations because of the smooth change in the system stiffness (the trilinear system approaches a bilinear response, similar to those previously analyzed in section 5.2.2). Regarding the f_y/f_e ratio, when low ratios were used (f_y/f_e=1), the damage in the hyperelastic structure was mainly because of acceleration-sensitive component failures. Increasing the ratio reversed the loss distribution proportions.

5.3.3. Trilinear, 3-Story Building, High Ductility (CASE B)

As mentioned in the scope of this work, the same initial stiffness (K_0=K_{h0}) was used for both hysteretic and hyperelastic systems. The Case B prototype building was similar to Case D, but designed to withstand high seismic demands with greater ductility. The code provides a response modification factor, R, of 6 for structures with SCBFs. As discussed in the Methodology chapter, the natural period associated with this Case was estimated to be 0.4 sec.

As observed for Case D and C structures, hyperelastic Case B parameter evaluations with arresting stiffness ratio, K_3, greater than 10% of K_0 did not meet the force limit (equal or less elastic force than the corresponding hysteretic system). Accordingly, the SDOF analyses conducted were limited to K_3 equal 10%, 5%, and 2.5%. The main findings for each modeled K_3 value are summarized as follow:

- When K_3 equals 10% of the initial stuffiness (α_2 = 0.1), a ductility greater than 35 (μ>35) was required to meet the force limit (f_y>$f_{e,max}$) for all f_y/f_e ratios that complied (one to four). However, low f_y/f_e ratios (1 to 1.5) complied with the force limit while rendering lower ductility demands (μ>25). This means that for a system with a response modification factor, R, of 6, the hyperelastic buckling force should preferably be selected

close to the corresponding yield force of the hysteretic system to minimize uneconomically large structural peak displacements.

- When K_3 was set equal to 5% of K_0 ($\alpha_2 = 0.05$), parameter permutations that included ductilities higher than 15 ($\mu>15$) and f_y/f_e ratios between one and five met the force limit.

- For the shallowest arresting stiffness analyzed, K_3 equals 2.5% of K_0 ($\alpha_2= 0.025$), ductilities higher than 16 ($\mu>16$) were required when f_y/f_e equaled one ($f_y=f_e$) to ensure that the hyperelastic brace force will be equal to or less than the complementary hysteretic brace. However, for higher f_y/f_e (2 to 5) ratios ductilities as low as five ($\mu>5$) secured peak mechanical forces below the threshold ($f_{e,max}<f_y$).

5.3.3.1. Case B. Loss Assessment Estimates

Loss assessments using the HAZUS-MH methodology were conducted for each arresting stiffnesses noted previously (10%, 5%, and 2.5% of K_0) and the results are summarized in Figure 44, Figure 45, and Figure 46, respectively.

The analyses indicated that none of the hyperelastic systems discussed above would reduce the cost of replacing nonstructural and contents elements. Despite the savings from structural system protection, the repair cost would rise to around 20% over the traditional hysteretic.

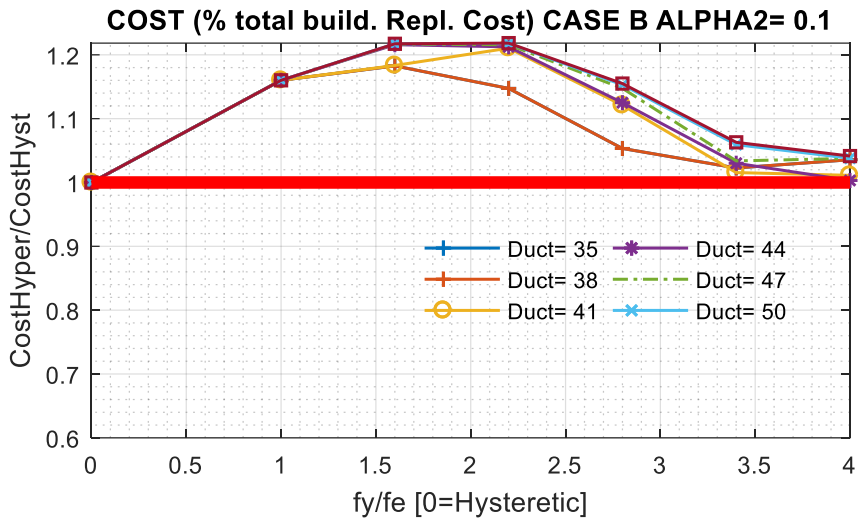

Figure 44. CASE B- α_2=0.1; Normalized repair cost, ductility, and fy/fe ratio.

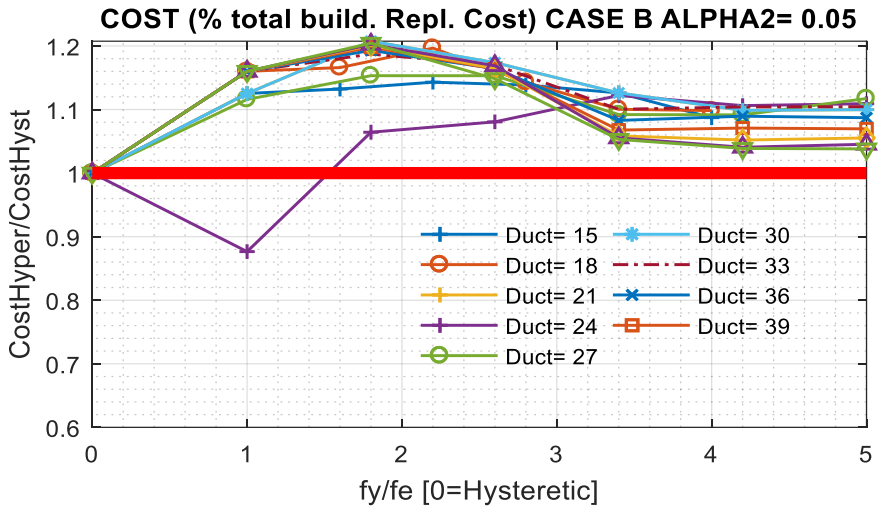

Figure 45. CASE B- α_2=0.05; Normalized repair cost, ductility, and f_y/f_e ratio.

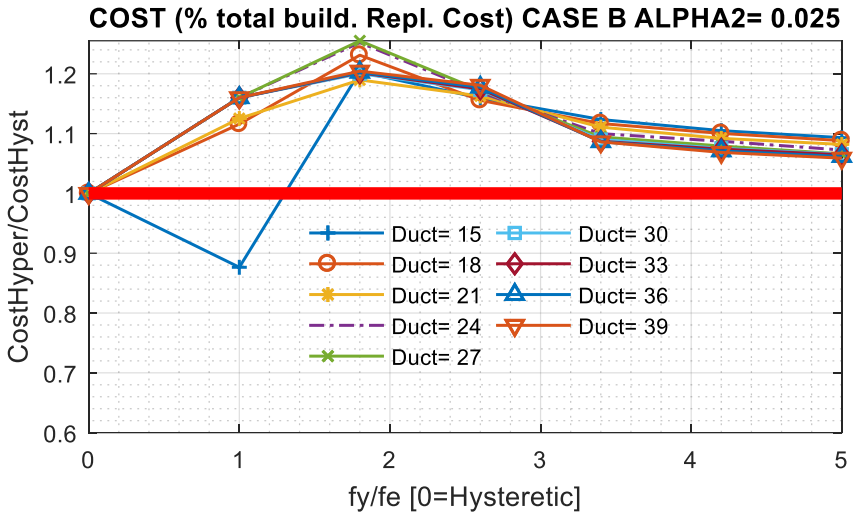

Figure 46. CASE B- α_2=0.025; Normalized repair cost, ductility, and f_y/f_e ratio.

5.3.3.2. Case B. Summary

Most of the hyperelastic systems that rendered less or equal peak force demand than the hysteretic system ($f_{e,max}<f_y$) did not produce direct economic loss reductions. However, in Figure 45, there was a single hyperelastic system that produced a lower repair cost than that of the hysteretic system. This system has a ductility of 24 and a f_y/f_e ratio of 1 ($f_y=f_e$). Analyzing the only beneficial response may help to understand why the rest that were examined failed. Figure 48 presents response plots for a single ground motion. In Figure 47b, the hysteretic system experienced a large permanent displacement (Δ_{hmax}>100 mm, 3.93 in), while there were not significant differences regarding peak accelerations (Figure 48a). Furthermore, the loss distribution plot (see Figure 49b) showed that when f_e is set to equal f_y, the vast majority of damage comes from acceleration-sensitive elements. Based on this scenario, this particular hyperelastic system saves 10% in repair costs over the hysteretic, because the structural damage was avoided while damage to acceleration-sensitive elements was comparable.

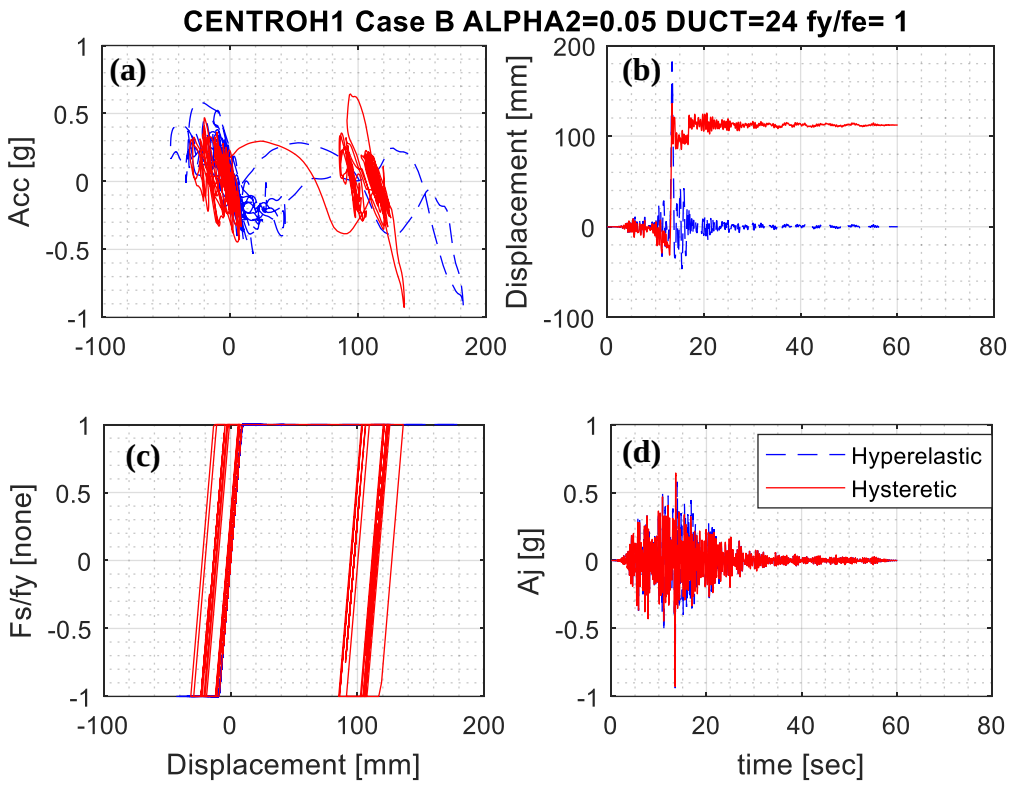

Figure 47. CASE B. (a) Acc. Vs Disp.; (b) Disp. vs. time; (c) normalized brace force vs. Displ.; (d) Acc. vs. time.

The loss distribution analysis illustrated by Figure 48 shows that for all systems, the loss of drift-sensitive elements accounted for most of the damage for all systems evaluated (independently of the K_3, f_y/f_e ratio, and ductility).

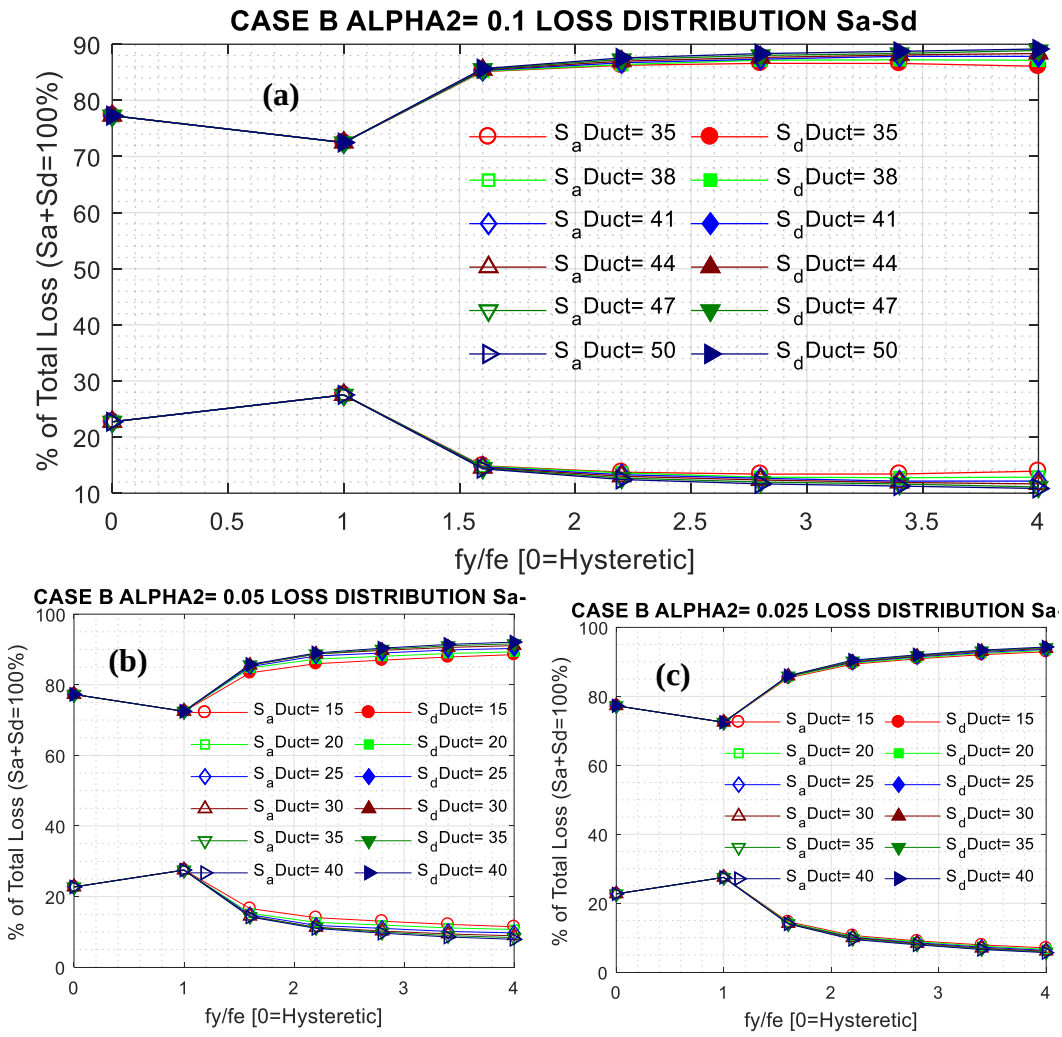

Figure 48. CASE B. **(a)** Loss distribution for α_2=0.1; **(b)** loss distribution for α_2=0.05; **(c)** loss distribution for α_2=0.025.

5.3.4. Trilinear, 1-Story Building, High Ductility (Case A).

Similar to previous cases, three values of α_2 were evaluated (0.1,0.05, and 0.025) for all ductility and f_y/f_e variations that rendered superior or competitive peak responses to that of the reference hysteretic. After extensive parameter changes, the optimal combinations of K_3 (α_2), ductility, and hyperelastic peak force ($f_{e,\,max}$) are:

- For α_2= 0.1, a ductility higher than sixty (μ>60) is required to meet the force limit, only f_y/f_e ratios between 1 to 1.5 passed the force limit criterion. Furthermore, systems equipped with lower f_y/f_e ratios met the hysteretic force threshold with lower ductility demands (μ>45). Regarding peak displacements, the closer f_e was to f_y, the better.
- For systems with α_2= 0.05, ductilities higher than forty-five were needed (μ>45) to ensure that $f_{e,\,max}<f_y$. This was true for f_y/f_e ratios between 1 and 1.3. For f_y/f_e ratios between 1.3 and 1.5, a ductility higher than sixty (μ>60) was needed to ensure that $f_{e,\,max}$ remained below f_y. Higher f_y/f_e ratios than 1.5 did not meet the force limit criterion.
- For hyperelastic configurations with α_2= 0.025, μ>45 allowed that $f_{e,\,max}<f_y$ for all f_y/f_e ratios between 1 to 1.5. Higher f_y/f_e ratios did not meet the force cap.

5.3.4.1. Case A. Loss Assessment Estimates

For this building (case A, R = 6, Tn = 0.2 sec), the loss assessment estimates conducted using HAZUS-MH are shown in Figure 49, Figure 50, and Figure 51, where α_2 equals 0.1, 0.05, and 0.025%, respectively. These analyses indicated that implementing none of the above hyperelastic systems would produce reductions in repair costs. Conversely, they would increase direct economic loss up to 40%.

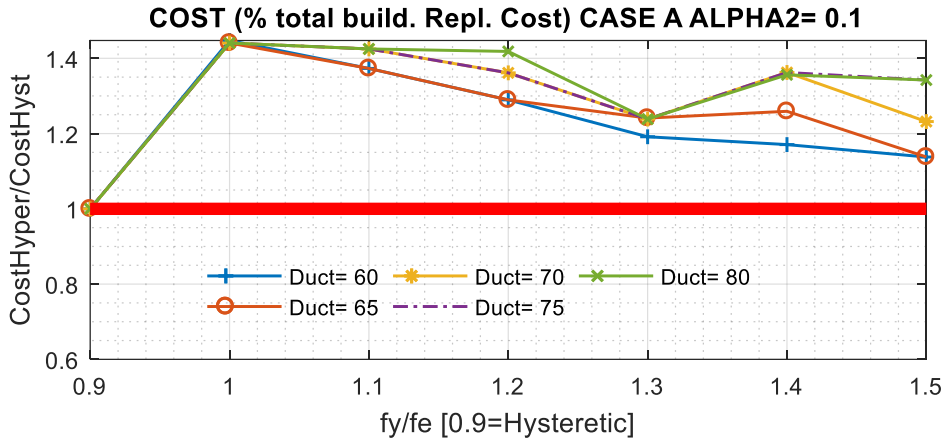

Figure 49. CASE A- α_2=0.1; Normalized repair cost, ductility, and f_y/f_e ratio.

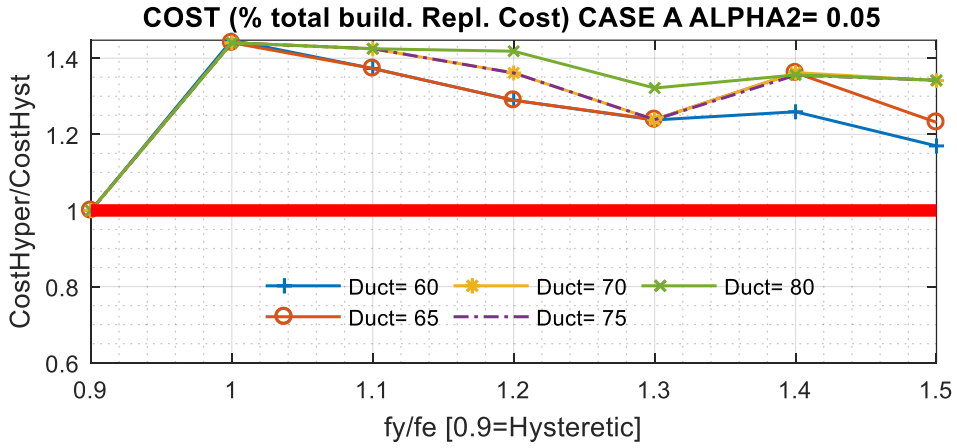

Figure 50. CASE A- α_2=0.5; Normalized repair cost, ductility, and f_y/f_e ratio.

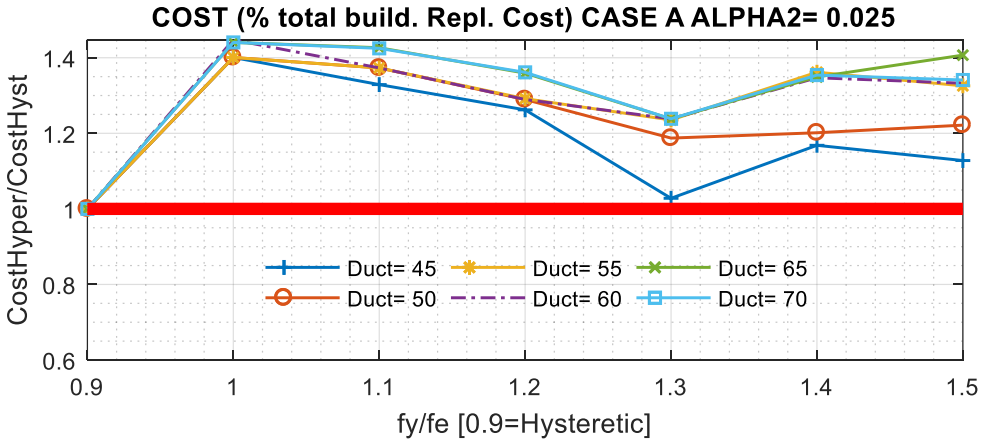

Figure 51. CASE A- α_2=0.025; Normalized repair cost, ductility, and f_y/f_e ratio.

5.3.4.2. Case A. Summary

None of the examined hyperelastic systems produced direct economic loss savings. Even though hyperelastic systems had a lower peak force than that of the hysteretic reference model ($f_{e,max}<f_y$), the accelerations reached by the hyperelastic system were equal or even higher to those in the hysteretic (see Figure 52a). Furthermore, the loss distribution shown in Figure 53 proves that displacement-induced damage constituted most of the total building loss. Therefore, avoiding structural damage by incorporating the hyperelastic fuse was not enough to render repair cost savings.

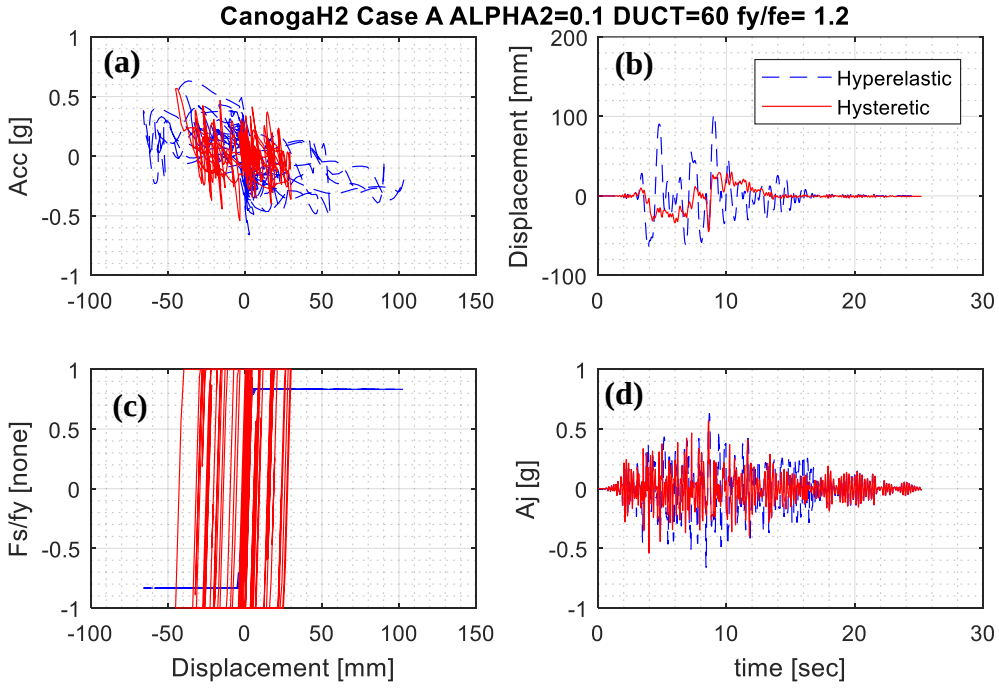

Figure 52. CASE A. (a) Acc. Vs Disp.; (b) Disp. vs. time; (c) normalized brace force vs. Displ.; (d) Acc. vs. time.

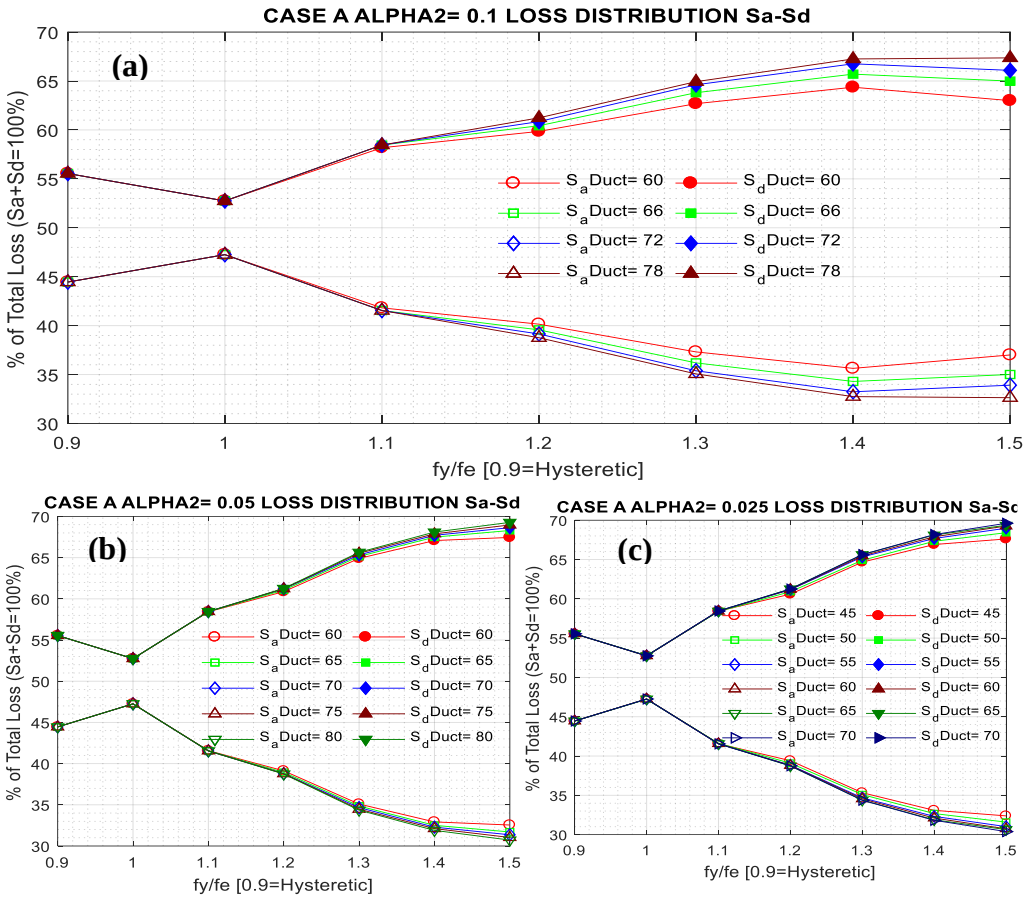

Figure 53. CASE A. (a) Loss distribution for α_2=0.1; (b) loss distribution for α_2=0.05; (c) loss distribution for α_2=0.025.

CHAPTER 6. CONCLUSIONS

Findings related to economic loss were drawn solely based on HAZUS direct economic loss assessments. HAZUS guidelines and procedures were developed by a team of earthquake loss experts, including earth scientists, engineers, architects, economists, emergency planners, social scientists, and software developers. (Schneider and Schauer 2006)

6.1. Case Specific

6.1.1. CASE D. (3 stories, R=3.1/4)

- In comparison with its hysteretic equivalent, the best trilinear hyperelastic performance rendered an average 20% total loss reduction to mitigate earthquake mainshock's effects.
- The buckling force of the slender elements must be three to six times less than the comparable hysteretic yielding force, while the gap of the fuse should remain within six to nine times the displacement corresponding to slender fusing element elastic buckling.
- Displacements were the primary source of damage for the hyperelastic models. Conversely, accelerations accounted for most of the direct economic loss in the reference hysteretic system.

6.1.2. CASE C (1 story, R=3.1/4)

- The trilinear hyperelastic alternative rendered an average 10% reduction of the direct repair cost (response to mainshock only).

- The buckling force of the slender elements must be three to six times lesser than the comparable hysteretic yielding force, while the gap of the fuse should remain within 19 to 39 times the buckling displacement of the slender elements.
- Displacements and accelerations contributed evenly to the final loss estimates for the hyperelastic system. On the other hand, the hysteretic direct loss was 85% due to acceleration-induced damage.

6.1.3. CASE B (3 stories, R=6)

- None of the hyperelastic parametric combinations having equal or reduced force compared to the hysteretic system produce reductions in mainshock direct economic loss. Alternative, multi-linear, hyperelastic combinations may reduce accelerations demands and thus reduce hyperelastic repair cost.
- Displacements are the primary source of damage for all hyperelastic systems as well as for the reference hysteretic.

6.1.4. CASE A (1-Story Building, High Ductility)

- None of the included trilinear hysteretic models rendered mainshock reparability savings. The accelerations reached were equal or higher, while the displacements were larger than the reference hysteretic system. Therefore, the advantages of using hyperelastic systems in this scenario are reduced to aftershock resistance to prevent casualties and reduced indirect economic and social impacts.
- Displacements were the primary source of damage (for hysteretic and hyperelastic models).

6.2. General

- Loss assessments for nominally comparable hysteretic systems were premised on full hysteresis under cyclic loading. However, OCBF and SCBF systems are expected to exhibit pinched hysteresis associated with global buckling of the brace between the end connections. The modeled hysteretic behavior is more representative of a buckling-restrained brace (BRB) system than a CBF system. Therefore, the loss estimates for hysteretic systems were unconservative (higher losses should be expected), which led to hysteretic-to-hyperelastic comparisons unfairly favorable to hysteretic systems.
- Loss assessment estimations for all prototype buildings discussed above (cases A, B, C, and D) provided with bilinear hyperelastic systems showed that none of such bilinear hyperelastic systems would produce reductions in repair costs. The results highlighted that reducing the peak mechanical force does not guarantee proportionate reductions in the system accelerations.
- Analyses of the considered trilinear hyperelastic systems suggested that the arresting stiffness (K_3) should generally remain below 10% of the initial stiffness (K_0) to prevent hyperelastic system maximum LFRS forces from exceeding the force demands for comparable hysteretic systems. Additionally, lowering the arresting stiffness diminishes the influence of ductility in the response. The transition to re-stiffening would not generate significant response variations because of the smooth change in the system stiffness (the trilinear system approaches a bilinear response). The fusing force ratio (ratio of hysteretic yield to

hyperelastic buckling, f_y/f_e) was the most important parameter, because it was strongly correlated to the peak displacement demands.

- The mainshock response of hysteretic stiff systems (low period) was outstanding. Therefore, more complex hyperelastic systems (i.e. more than two post-buckling stiffness [staircase]) should be explored to enhance reparability outcomes. Generally, for stiff systems, the hyperelastic savings from avoiding structural damage were not enough to offset drift-sensitive nonstructural losses.

6.3. Future Research Needs and Opportunities

- Hyperelastic systems will commonly display more flexible responses than those of conventional hysteretic structures. Therefore, their effectiveness could be highly dependent on site condition (stiff, dense, rock) and the interdependency of site motion and hyperelastic response.
- Second order effects (P-Δ) were not explicitly considered in this study. Additional studies accounting for full material and geometric nonlinearity are required to investigate the degree to which P-Δ may influence expected hyperelastic system performance.
- Additional studies should be performed to examine the relative performance outcomes across wider dimensions than addressed in this thesis. The study in this thesis was limited to direct economic loss (repair and replacement costs for structural, nonstructural, and contents). Hysteretic systems are susceptible to permanent deformations after inelastic excursions, whereas hyperelastic systems will return to the original configuration. This potential difference in residual

structure configuration can lead to indirect economic loss and social impacts due to interrupted occupancy and operational functionality that were not within the scope of this thesis, as well as susceptibility to aftershocks.

- The spectrum of possible hyperelastic systems using a controlled elastic-buckling mechanism is infinite, and more complex multi-linear hyperelastic systems could render better responses. For instance, it may be worth exploring various initial stiffnesses (K_0), or fuses with multiple buckling levels, in which slender elements with different lengths are strategically arranged to produce a staircase force-displacement response. Additionally, the medium in which the slender elements of the fuse displace once they have buckled could be modified to add damping and dissipate energy (e.g., exchange air for a denser fluid).

CHAPTER 7. REFERENCES

Ancheta, T. D., Darragh, R. B., Stewart, J. P., Seyhan, E., Silva, W. J., Chiou, B. S. J., Wooddell, K. E., Graves, R. W., Kottke, A. R., Boore, D. M., Kishida, T., and Donahue, J. L. (2013). "PEER NGA-West2 Database."

ASCE/SEI. (2010). *ASCE/SEI 7-10 Minimum Design Loads for Buildings and Other Structures*. *ASCE/SEI 7-10 Minimum Design Loads for Buildings and Other Structures*.

Chopra, A. K. (2012). *Dynamics of Structures Theory and Applications to Earthquake Engineering*. (holly stark, ed.), pearson.

Christopoulos, C., Tremblay, R., Kim, H.-J., and Lacerte, M. (2008). "Self-Centering Energy Dissipative Bracing System for the Seismic Resistance of Structures: Development and Validation." *Journal of Structural Engineering*, 134(1), 96–107.

Clifton, C., Bruneau, M., Macrae, G., Leon, R., and Fussell, A. (2011). *No Title*. *Bulletin of the New Zealand Society for Earthquake Engineering*.

Cook, J., Rodgers, G. W., Macrae, G. A., and Chase, J. G. (2015). "Development of a ratcheting , tension-only fuse mechanism for seismic energy dissipation."

Erochko, J., and Christopoulos, C. (n.d.). "Self-Centering Energy-Dissipative (SCED) Brace: Overview of Recent Developments and Potential Applications for Tall Buildings."

Erochko, J., and Christopoulos, C. (2014). "Self-centering energy-dissipative (SCED) Brace: Overview of recent developments and potential applications for tall buildings." *Sustainable Development of Critical Infrastructure - Proceedings of the 2014 International Conference on Sustainable Development of Critical*

Infrastructure, 488–495.

FEMA. (2000). “Seismic design criteria for new moment-resisting steel frame construction, Report No. FEMA 350.” 221.

FEMA. (2015). “Hazus–MH 2.1: Technical Manual.” *National Institute of Building Sciences and Federal Emergency Management Agency (NIBS and FEMA)*, 718.

Gao, N., Jeon, J.-S., Hodgson, D. E., and DesRoches, R. (2016). “An innovative seismic bracing system based on a superelastic shape memory alloy ring.” *Smart Materials and Structures*, IOP Publishing, 25(5), 55030.

Goldsworthy, H. M. (2012). “Lessons on building design from the 22 February 2011 Christchurch earthquake.” *Australian Journal of Structural Engineering*, 13(2), 159–174.

Hajjar, J. F., Sesen, A. H., Jampole, E., and Wetherbee, A. (2013). “Rocking , Self-Centering , and Articulated Energy- Dissipating Fuses.” *Journal of Earthquake Engineering*, 10(1), 45–66.

Hashemi, A., Zarnani, P., Masoudnia, R., and Quenneville, P. (2017). “Seismic resistant rocking coupled walls with innovative Resilient Slip Friction (RSF) joints.” *Journal of Constructional Steel Research*, Elsevier Ltd, 129, 215–226.

Kircher, C. a., Whitman, R. V., and Holmes, W. T. (2006). “HAZUS Earthquake Loss Estimation Methods.” *Natural Hazards Review*, 7(2), 45–59.

Malley, J. O., Popov, E. P., and Asce, F. (n.d.). “SHEAR LINKS IN ECCENTRICALLY BRACED FRAMES.”

McCormick, J., DesRoches, R., Fugazza, D., and Auricchio, F. (2007). “Seismic assessment of concentrically-braced steel frames with shape memory alloy braces.”

Journal of Structural Engineering-Asce, 133(6), 862–870.

Patro, S., and Sinha, R. (2008). “Optimal seismic performance of friction energy dissipating devices.” *The 14th World Conference on …*.

Qiu, C. X., and Zhu, S. (2017a). “Performance-based seismic design of self-centering steel frames with SMA-based braces.” *Engineering Structures*, 130, 67–82.

Qiu, C., and Zhu, S. (2017b). “Shake table test and numerical study of self-centering steel frame with SMA braces.” *Earthquake Engineering and Structural Dynamics*.

Rahimatpure, A. (2012). “Smart Memory Alloys.” 118–120.

Rodriguez-Nikl, T. (2015). “Linking disaster resilience and sustainability.” *Civil Engineering and Environmental Systems*, 32(1–2), 157–169.

Roeder, C. W., and Popov, E. P. (1978). “Eccentrically Braced Steel Frames for Earthquakes.” *Journal of the Structural Division*, 104(3), 391–412.

Schneider, P. J., and Schauer, B. A. (2006). “HAZUS—Its Development and Its Future.” *Natural Hazards Review*, 7(2), 40–44.

Stevenson, J., Kachali, H., Whitman, Z., Seville, E., Vargo, J., and Wilson, T. (2011). “Preliminary Observations of the Impacts the 2nd February Christchurch Earthquake had on Organisations and the Economy: A Report from the Field.” *Bulletin of the New Zealand Society for Earthquake Engineering*, 44(2).

Taghavi, Shahram; Miranda, E. (2004). “13 th World Conference on Earthquake Engineering ESTIMATION OF THE DYNAMIC PROPERTIES FOR GEOSYNTHETIC INTERFACES.” *Program*.

Tremblay, R., Lacerte, M., and Christopoulos, C. (2008). “Seismic Response of Multistory Buildings with Self-Centering Energy Dissipative Steel Braces.” *Journal*

of Structural Engineering, 134(1), 108–120.

USGS. (2015). “Design Maps Site D-Stiff Soil.” 1–9.

Vargas, R., and Bruneau, M. (2005). “Investigation of the Structural Fuse Concept.” *Draft Report*.

Vargas, R., and Bruneau, M. (2009). “Analytical Response and Design of Buildings with Metallic Structural Fuses. I.” *Journal of Structural Engineering*, 135(4), 386–393.